UNIVERSITY OF CALIFORNIA, SAN DIEGO

Exchange Bias at the Nanoscale:

Bulk or Interface?

A dissertation submitted in partial satisfaction of the requirements for the degree

Doctor of Philosophy

in

Materials Science and Engineering

by

Ali Cemil Basaran

Committee in charge:

Professor Ivan K. Schuller, Chair
Professor Eric E. Fullerton
Professor Shirley Meng
Professor Lu J. Sham
Professor Oleg Shpyrko

2014

The Dissertation of Ali Cemil Basaran is approved, and it is acceptable in quality and form for publication on microfilm and electronically:

Chair

University of California, San Diego

2014

Dedication

Dedicated to my parents

Table of Contents

List of Abbreviations

- AMR – Anisotropic magnetoresistance
- AFM – Antiferromagnetic
- FM – Ferromagnetic
- H_{EB} – Exchange bias field
- MFMMS – Magnetic field modulated microwave spectroscopy
- MR – Magnetoresistance.
- MOKE – Magneto optical Kerr Effect
- PHE – Planar Hall Effect
- SQUID – Superconducting interference device
- VSM – Vibrating sample magnetometer
- XRR – X ray reflectivity
- XRD – X ray diffraction

List of Figures

List of Tables

Acknowledgements

Over the past five years, I have received support and encouragement from a great number of individuals. Today, it is my great pleasure to take this opportunity to thank those whose advice, assistance and support contributed to this dissertation in a variety of ways.

I would first thank my wife, Emel, and my daughters, Zeynep Sena and Asude, for their love, patience, understanding, and support during the times when I was too absorbed in my work. Without their efforts and sacrifices, I would have never been able to complete my PhD research.

Primarily I would like to thank my thesis advisor, Ivan Schuller, for all his support and encouragement throughout my graduate career. Ivan has been not only a mentor, but also a colleague, and, most importantly, a friend. I am very much grateful to have a chance to learn his philosophy of science. All of the *Schuller Rules* will be great assets for my future career. I am so proud to work with Ivan and to be part of his scientific family.

I would like to thank my thesis committee members, Lu Sham, Eric Fullerton, Oleg Shpyrko, and Shirley Meng, for all of their guidance through this process; your discussion, ideas, and feedback have been absolutely invaluable.

I thank Rafael Morales for his in-depth inspiring conversations during coffee times, and enormous help with the exchange biased cross junction project. Additionally, Rafael contributed hugely to my understanding of the exchange bias phenomena. I

would like to thank Thomas Saerbeck for his contributions to the experimental and theoretical interpretation of the ion irradiation project. His ideas and philosophy on data analyses helped me to understand how to approach a research problem as well as how to appropriately present the work. I thank Jose de la Venta for his help with all my research and his invaluable friendship over years. I also want to take this chance to express my utmost appreciation for Carlos Monton. His personal assistance, guidance, and valuable discussions over years were among the most important lessons.

I thank rest of my fellow labmates in Schuller's Nanoscience group: Corneliu Colesniuc, Kevin West, Yaniv Rosen, Mikhail Erekhinsky, Siming Wang, Ilya Valmianski, Jamie Wampler, Stefan Guenon, Gabriel Ramirez, Juan Viterbo, and Christian Urban. They have always been very helpful throughout my graduate school experience. I would like to give a special thanks to Ilya and Jamie who have helped with proofreading of this dissertation in part.

I would like to thank one-time visitors: Yvan Bruynseraede, Gernot Guntherodt, Jose Luis Vicent, Shimshon Barad, Victoria Bekeris, Prasenjit Guptasarma, Samuel Hevia, Miguel Kiwi, Javier Villegas, Felix Casanova, Axel Hoffmann, Michael Fitzsimmons, Xavier Batlle, and colleagues at UCSD: Sunil Sinha, Dimitri Basov, Brian Maple, Zachary Fisk, Jorge Hirsch, and Shelly Schultz for sharing ideas, discussing results, and giving crucial suggestions.

I am also grateful Bernd Fruhberger, Ryan Anderson, Maribel Montero from Nano3 for their help with experimental and instrumental issues. I thank Robin Knox and

Amie Diza from Physics and Charlotte Lauve from Materials Science and Engineering departments for their help with all paper works and bureaucratic issues. I thank Kevin Smith (and all the rest of computer stuff) and Lester Brooks for helping whenever we need and making our life easier.

I thank my former colleagues in Turkey: Bekir Aktas, Yildirhan Oner, Bulat Ramaev, Faik Mikailov, Zafer Ziya Ozturk, Rauf Suleymanov, Savas Berber, Mustafa Ozdemir, Orhan Yalcin, Yusuf Yerli, Osman Ozturk, Sait Eren San, Fikret Yildiz, Resul Yilgin, Atilla Buyukguclu, Ekrem Demirel, and Numan Akdogan for their support and encouragement before and during my PhD career. I thank Mehmet Tarakci for his guidance and assistance. I am thankful for the support and sponsorship from Republic of Turkey Ministry of National Education and for the help from the officers who work in New York Educational Attaché and Ankara. I especially thank my dear friends Sinan Kazan, Ahmet Semih Kucukozet, and Mustafa Okutan. I would not have done without their trust and sacrifice at the beginning.

I wholeheartedly thank my parents. Without their support in every possible way I would not be where I am today.

Chapter 2, in part, is currently being prepared for publication. Co-authors include Rafael Morales, Stefan Guenon, and Ivan K. Schuller. The dissertation author was the primary investigator and author of this material. Ali C. Basaran worked on the sample design, performed the fabrication, measurement, and analysis for this work, and

will be the primary author on the paper. I would also like to thank Rafael Morales for useful conversations and simulations.

Chapter 3, in part, is published in: Ali C. Basaran, T. Saerbeck, J. de la Venta, H. Huckfeldt, A. Ehresmann, and Ivan K. Schuller, "Exchange bias: the antiferromagnetic bulk matters", Applied Physics Letters 105, 072403 (2014). The dissertation author was the primary investigator and author of this material.

Chapter 3, in part, is currently being prepared for publication of the material. Co-authors include T. Saerbeck, J. de la Venta, H. Huckfeldt, A. Ehresmann, X. Batlle, and Ivan K. Schuller, The dissertation author is the primary investigator and author of this material. I would like to thank Henning Huckfeldt and Arno Ehresmann for their productive collaboration with ion bombardment and SRIM simulations in chapter 3.

Chapter 4, in part, is currently submitted to Physical Review Letters for publication of the material. Co-authors include R. Morales, J.E. Villegas, D. Navas, N. Soriano, B. Mora, C. Redondo, X. Batlle, and Ivan K. Schuller. Ali C. Basaran worked on the sample design, performed the fabrication, measurement, and analysis for this work, and will be the second author on the paper.

Chapter 5, in part, contains work performed in several different projects. Some of them have been previously published in:

J. de la Venta, Ali C. Basaran, T. Grant, A. J. S. Machado, M. R. Suchomel, R. T. Weber, Z. Fisk, and Ivan K. Schuller, "Methodology and search for superconductivity in the La-Si-C system", Superconductor Science and Technology 24,

075017 (2011). Ali C. Basaran worked on the sample design, fabrication, measurement, contributed to the rietveld refinement, and analysis for this work. I would like to thank Ted Grant for fabrication of arc melted samples.

J. de la Venta, Ali C. Basaran, T. Grant, J.M. Gallardo-Amores, J.G. Ramirez, M.A. Alario-Franco, Z. Fisk, and Ivan K. Schuller, "Magnetism and the absence of superconductivity in the praseodymium–silicon system doped with carbon and boron", Journal of Magnetism and Magnetic Materials 340,27-31, (2013). Ali C. Basaran worked on the sample design, measurement, and data analysis for this work.

S. Guenon, Y.J. Rosen, Ali C. Basaran, and Ivan K. Schuller, "Highly effective superconducting vortex pinning in conformal crystals", Applied Physics Letters 102, 25, (2013). Ali C. Basaran contributed to the sample fabrication, lithography, measurement, and analysis for this work.

J. Ramirez, Ali C. Basaran, J. de la Venta, J. Pereiro, and Ivan K. Schuller, "Magnetic Field Modulated Microwave Spectroscopy (MFMMS) across phase transitions and the search for new superconductors", Reports on Progress in Physics accepted (2014). The dissertation author was the primary investigator and the co-first-author of this paper. Ali C. Basaran worked on the equipment design and installation, performed sample design and fabrication, measurement, and analysis for this work.

Chapter 5, in part, is currently submitted to Scientific Reports for publication of the material. Co-authors include S. Guenon, J.G. Ramirez, M. Thiemens, S. Taylor, and

Ivan K. Schuller. Ali C. Basaran contributed to the measurement and analysis for this work and will be a co-author of this material.

Chapter 5, in part, is currently being prepared for publication of the material. Co-authors include G. Ramirez, J. de la Venta, S. Wang, T. Saerbeck, X. Batlle, and Ivan K. Schuller. Ali C. Basaran contributed to the FMR measurement and analysis for this work and will be a co-author of this material.

Chapter 5, in part, is currently submitted to Nano Letters for publication of the material. Co-authors include A.F. Rodriguez, M. Kovylina, R. Morales, J. Llobet, X. Borrise, M.A. Marcus, A. Scholl, Ivan K. Schuller, X. Batlle, and A. Labarta. Ali C. Basaran performed the sample fabrication, magnetization measurements, and contributed to the date analysis for this work and will be a co-author of this material.

The work presented in this dissertation was funded by the Office of Basic Energy Science, U.S. Department of Energy, BES-DMS funded by the Department of Energy's Office of Basic Energy Science, DMR under grant DE FG03 87ER-45332, and an AFOSR MURI grant FA49550-09-1-0577 I want to thank them for their generous support.

Vita

2003	Bachelor of Science, Physics, Gazi University, Ankara, Turkey
2008	Master of Science, Physics, Gebze Institute of Technology, Kocaeli, Turkey
2014	Doctor of Philosophy, Materials Science and Engineering, University of California San Diego, La Jolla, California, USA

Abstract of the Dissertation

Exchange Bias at the Nanoscale:

Bulk or Interface?

by

Ali Cemil Basaran

Doctor of Philosophy in Materials Science and Engineering

University of California, San Diego, 2014

Professor Ivan K. Schuller, Chair

One of the most interesting topics in material science is the effect of geometric confinement on nanoscale magnetic structures. Confinement produces new phenomena not observed in bulk materials and has led to a large number of technologies. An important structure featuring a geometric confinement effect is a thin film multilayer. In particular, the exchange bias effect, which is present in some ferromagnet / antiferromagnet bilayers, is used in applications such as magnetic recording, sensing, and spintronic devices. Although exchange bias has been the focus of many experimental and theoretical investigations, the details of its mechanism are still

elusive. Above all, the contributions of magnetic structures in regions away from the interface remain ambiguous.

This dissertation studies the individual contributions of each region of the ferromagnetic/antiferromagnetic bilayer on the exchange bias. We consider the exchange bias effect in magnetic thin films as defined by the three components of the spin structure: i) at the ferromagnetic/antiferromagnetic interface, ii) in the antiferromagnetic layer, and iii) in the ferromagnetic layer. We performed experiments to address individually these three constituents and found that the exchange bias is significantly affected by the *bulk* of both the antiferromagnetic and the ferromagnetic layers.

We used Ni/FeF_2 bilayers as a prototypical exchange bias system. First, we explored magnetization reversal in cross shaped nano-junctions using the planar Hall Effect. We demonstrated how to find the direction of magnetization rotation and obtained the angular distribution of the unidirectional anisotropy axes. Second, we investigated the contribution from the antiferromagnetic bulk using ion bombardment to induce controllable depth dependent defects. We unambiguously showed that the exchange bias can be tuned without altering the interface or the ferromagnetic layer. Third, we investigated the ferromagnetic layer thickness dependence on the exchange bias. We found a strong deviation from the inverse proportionality law and demonstrated the importance of the spin structure in the ferromagnetic layer. An incomplete domain wall model was used to quantitatively account for the experimental results. Our studies show that the bulk of the antiferromagnetic and the ferromagnetic

layers, together with the interface, are crucial ingredients in the establishment and the control of the exchange bias.

1. Introduction

1.1. Motivation and scope of the thesis

Magnetism is a physical phenomenon that originates either from electrical currents or magnetic moments of elementary particles. Although magnetism has been known for millennia, our ability to understand the physics behind this important phenomenon has emerged only in the last two centuries. Magnetism has had many applications throughout history. One of the earliest was compasses, which dramatically improved open sea navigation. Today, magnetism-based devices have superseded Cuneiform Scripts, pen and paper, and even print as the principle methods of recording.

The last few decades saw vast development of experimental techniques for ultrasmall length scale material growth. This has led to many new applications since physical properties can change significantly when the material is geometrically reduced to relevant length scales. For magnetism, such characteristic length scales, e.g., the exchange length and the magnetic domain wall width, occur at the nanometer scale. Therefore, when the size of a magnetic material is reduced to the nanoscales (at least in one dimension), magnetic properties different from those in the bulk emerge. This is the basis of a new research area called *Nanomagnetism*, which includes the study of properties and applications of the magnetism in nanodots, nanowires, thin films, multilayers, etc. [1].

For thin films, the neighboring physical environment needs to be taken into account since they are generally in close contact with a substrate, a capping layer, or another film. This means the physical properties of magnetic thin films can be affected by its neighbors. For example, proximity effects such as exchange bias appear when two dissimilar magnetic materials are getting close to each other [2].

Exchange bias is one of the phenomena associated with the exchange anisotropy created at the interface typically between an antiferromagnetic (AFM) and a ferromagnetic (FM) material. It is defined as a shift of the magnetic hysteresis loops with respect to the applied field axis. It was discovered in 1956 by W. H. Meiklejohn and C. P. Bean when studying Co particles embedded in their native antiferromagnetic oxide [3]. Since then, exchange bias has been in the focus of many experimental and theoretical investigations [2, 4]. Although it has been widely used in magnetic recording and sensor applications [5-7], a quantitative predictive theory of exchange bias is not available to date [8]. In fact, the details of the mechanism leading to exchange bias are still elusive and there are contradicting experimental and theoretical studies [9].

Due to the short range of the exchange interaction, the exchange bias phenomenon has been mostly considered an interfacial effect. Hence, most of the exchange bias models take into account the coupling between FM and AFM spins just around the interface [10]. One of the controversies is whether the AFM bulk needs to be considered in the establishment and magnitude of the exchange bias [8, 11]. Some experimental evidence shows that both the bulk of the AFM layer and the interface play a role in determining the magnitude of the exchange bias field [11-13]. Furthermore, it

has been widely reported that the thickness of the FM layer and the magnitude of the exchange bias field are inversely proportional [4, 14, 15]. However, the spin configuration in the FM layer should not be ignored [16], and the effect of the FM spin configuration perpendicular to the interface needs to be investigated.

There are also studies that examine dependence of exchange bias field on sample morphology. For example, it has been shown that sample specific morphologies, such as roughness [17, 18], grain size [19-21], crystallinity [22, 23], interlayer diffusion [24], and defects [25, 26] are crucial in determining exchange bias properties. The magnitude and sign of the exchange bias can be further altered by the magnetic field and temperature history [27, 28]. Therefore, the exchange bias effect is fundamentally attributable to several extrinsic and intrinsic parameters, which become very important at nanoscales [29-31]. A unifying theory taking into account all of the above parameters might be hard to develop. Likewise, a new experiment is required to simultaneously detect and separate contributions from the interface and the bulk.

With the above motivation, this dissertation is mostly focused on the fabrication and investigation of nanomagnetic exchange bias systems and investigating individual contributions from each component. We consider the exchange bias effect in magnetic thin films as mainly defined by the three components of the spin structure; i) at the FM/AFM interface, ii) in the AFM layer, and iii) in the FM layer (Figure 1). We investigate these three ingredients individually using different experimental approaches in each dedicated chapter and aim to understand the corresponding contributions.

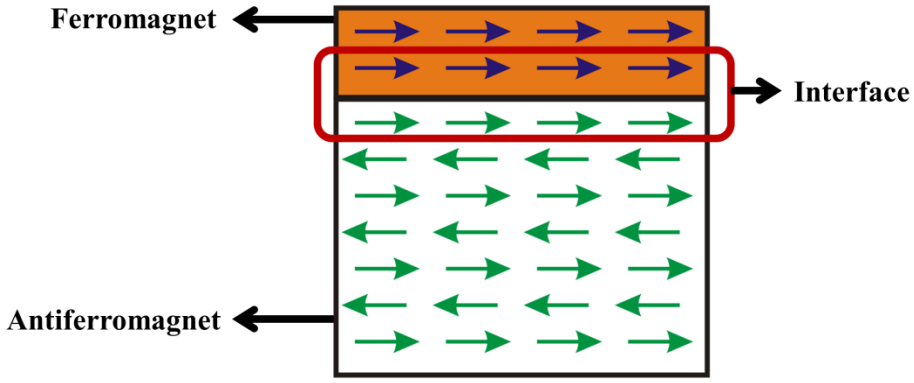

Figure 1. Schematic of an exchange bias system and its three main constituents: the ferromagnet, the interface, and the antiferromagnet.

In chapter 2, in order to understand the general properties of our model exchange bias system, Ni/FeF_2, we performed magnetoresistance measurements by using a cross shaped FM nano-junction. A lithographically patterned metallic ferromagnetic (Ni) cross was placed on an insulating antiferromagnetic film (FeF_2), which introduced the exchange coupling. Measuring the transport above and below the Neel temperature of FeF_2 allowed exploring the dependence of the magnetization reversal in the FM junction depending on the presence or absence of the bias. The advantage of having a cross shaped junction is that longitudinal (anisotropic magnetoresistance) and transverse (planar Hall Effect) components of the magnetization could be simultaneously measured via magnetoresistance measurements. We showed that the magnetization rotation way (chirality) can be detected by the magnetoresistance measurements. The dependence of reversal on temperature, cooling field, and cooling angle were investigated. The angle between the easy axis of the AFM lattice and the applied field axis strongly affects the magnetization reversal. We compared three

techniques; anisotropic magneto resistance, planar Hall Effect, and magnetometry for the same sample. We found that the planar Hall Effect, compared to other two techniques, is extremely sensitive to the small deviations from the easy axis. Furthermore, the angular dependence of the exchange anisotropy was investigated by rotating the sample in an applied magnetic field (in-plane). The sample rotation in the presence of the applied field perturbs the pinned FM moments from the unidirectional anisotropy axis. Thus, the exchange coupling was examined at different applied fields. We used incomplete domain wall model to simulate the experimental data. The results are in excellent agreement with the model. We used the same model to explain the data in chapter 4 and the validity of the model was confirmed in independent experiments.

In chapter 3, we will present an experimental approach which allows us to separate and investigate the individual contributions of the AFM bulk and interface on exchange bias. We used He-ion bombardment to create defects and therefore control both magnitude and direction of exchange bias field. We employed two different approaches: i) the defects are selectively created either in the bulk of the AFM layer or at the FM/AFM interface by varying the capping layer thickness, and ii) the number of defects at a certain depth is controlled by varying the ion dose. We have obtained the penetration depth profiles of bombardment ions and the number of vacancies (defects) from SRIM (Stopping and Range of Ions in Matter) simulations [32] . Extensive structural and magnetic characterizations before and after the bombardment allow us to investigate the effect of selectively created defects on exchange bias. These results unambiguously reveal that the AFM bulk is an important ingredient in the establishment

and control of the exchange bias and has to be included in any theoretical consideration. Moreover, the ion dose dependency leads to two important conclusions: i) the exchange bias can be significantly affected only by creating defects into the bulk of the AFM layer – without altering the interface, and ii) the exchange bias field and the coercive field are decoupled and can behave independently.

In chapter 4, we examine the influence of the spin configuration of the FM layer on exchange bias. In particular, we investigate the exchange bias field dependence both on FM layer thickness and on temperature. Several Permalloy (and Ni)/FeF_2 films with varying FM layer thickness were prepared in-situ and investigated with magnetization measurements. These measurements reveal that the exchange bias field is affected by the FM spin structure, which introduces a correction to the widely accepted inverse proportionality rule. A model based on the incomplete domain walls quantitatively accounts for the experimental results and, in particular, explains the deviation from the inverse proportionality rule.

Chapter 5 will be devoted to a summary of other studies that have been performed during the PhD research. The most important was the search for new superconducting materials using Magnetic Field Modulated Microwave Spectroscopy (MFMMS). We demonstrated that MFMMS is both highly sensitive and selective. We have analyzed more than two thousand samples including several different types of superconducting and non-superconducting samples. We identified a known superconducting phase in a new compound [33]. We also found a new magnetic phase in Pr-Si-C system [34]. We wrote a review article about the technique and application to

the search for new superconducting materials [in press]. The search for new superconducting phases in meteorites and micro-meteorites is still an ongoing project. We have also investigated the superconducting vortex pinning in conformal crystal geometry [35]. There are many other ongoing projects at the time of the writing of this dissertation that will be briefly addressed in chapter 5.

Finally, a summary and conclusions of the works that are presented in this dissertation will be given in chapter 6.

1.2. FM/FeF_2 thin film bilayers

Although exchange bias was first discovered in core-shell nanoparticles [3], it has been observed in variety of systems containing small particles [36], inhomogeneous materials [37], and thin films [18]. In particular, exchange bias in thin films has been of great interest due to its applications in the sensor and storage technologies [5, 6, 38]. In this thesis we will focus on exchange bias in FM/FeF_2 thin film bilayers. We refer to several comprehensive reviews on the exchange bias phenomenon for the detailed description of the effect [2, 4, 8, 9, 15, 31, 39].

FeF_2 was chosen as an AFM material due to its well-defined structural and magnetic properties. FeF_2 has a tetragonal structure with the lattice constant values of the *a* and *c* directions being 0.46945 and 0.33097 nm, respectively [40]. It is grown epitaxially on the [110] surface of single crystal MgF_2 substrates with very well defined

easy axis along [001] of FeF_2 and MgF_2. The AFM transition temperature is ~79 K [22]. FeF_2 has a very large uniaxial anisotropy with a rather simple magnetic configuration that makes it an ideal Ising-like AFM system [41, 42]. When FM layers (such as Nickel, Permalloy, Iron, or Cobalt) are grown on epitaxial FeF_2, they show a growth induced uniaxial magnetic anisotropy, which coincides with the easy axis of FeF_2 [43].

FM/FeF_2 bilayers are perhaps one of the most systematically studied exchange bias systems. FM/FeF_2 usually shows a large exchange bias shift without training and time dependences. The blocking temperature and the Neel temperature are the same. Many interesting features have been shown such as coexistence of positive and negative exchange bias [27], magnetization reversal asymmetry [44, 45], and anomalous temperature dependence [28]. Proving the existence of the pinned, uncompensated spins in FeF_2 illuminates the current understanding of the exchange bias phenomenon [46, 47]. However, there are still unanswered questions for further research such as the origin and exact locations of the pinned uncompensated spins.

1.3. Incomplete domain wall model

In order to explain the exchange bias in FM/FeF_2 bilayers, we propose a model sketched in Figure 2. This model accounts for the magnetization reversal through rotation of the magnetic moments rather than domain wall nucleation and motion [48,

49]. This is mostly satisfied at low temperatures in materials with small magnetocrystalline anisotropy such as Py and Ni.

In this model, domain walls parallel to the FM/AFM interface are considered in both the AFM and the FM layers. There is no domain wall formation taken into account perpendicular to the interface. The FM layer is divided into *N* planar sub-layers. The magnetic moment of each sub-layers forms an angle β_i with the easy axis, corresponding $i = 1$ to the FM sub-layer in contact with the antiferromagnet. The angular reference is defined by the easy axis of the magnetic system. The maximum angle of the domain wall in the antiferromagnet, α, is given by the orientation of nearest AFM spins to the interface. The external magnetic field is applied along the easy axis. The total energy of the system is given by three contributions: the AFM domain wall energy (E_{AF}), the exchange energy at the interface ($E_{AF\text{-}FM}$), and the FM energy (E_{FM}). E_{FM} comprises the exchange coupling between FM sub-layers, the anisotropy energy and the Zeeman energy of each sub-layer. Thus, the total energy can be expressed the sum of all:

$$E = E_{AF} + E_{AF-FM} + E_{FM}, \tag{1.1}$$

where,

$$E_{AF} = 2\sqrt{A_{AF}K_{AF}}(1-\cos\alpha), \tag{1.2}$$

$$E_{AF\text{-}FM} = -J_{AF\text{-}FM}\cos(\beta_1 - \alpha), \tag{1.3}$$

$$E_{FM} = -J_{FM}\sum_{i=1}^{N-1}\cos(\beta_{i+1}-\beta_i) - K_{FM}\Delta t_{FM}\sum_{i=1}^{N}\cos^2\beta_i - M\Delta t_{FM}H\sum_{i=1}^{N}\cos\beta_i\ . \tag{1.4}$$

A_{AF} and K_{AF} stand for the exchange stiffness and anisotropy constant of the AF, respectively. $J_{AF\text{-}FM}$ is the exchange coupling constant at the interface while J_{FM} denotes the exchange coupling constant between adjacent FM sublayers. K_{FM} is for the FM anisotropy constant, m_i is for the magnetic moment of each sublayer and H represents the applied magnetic field.

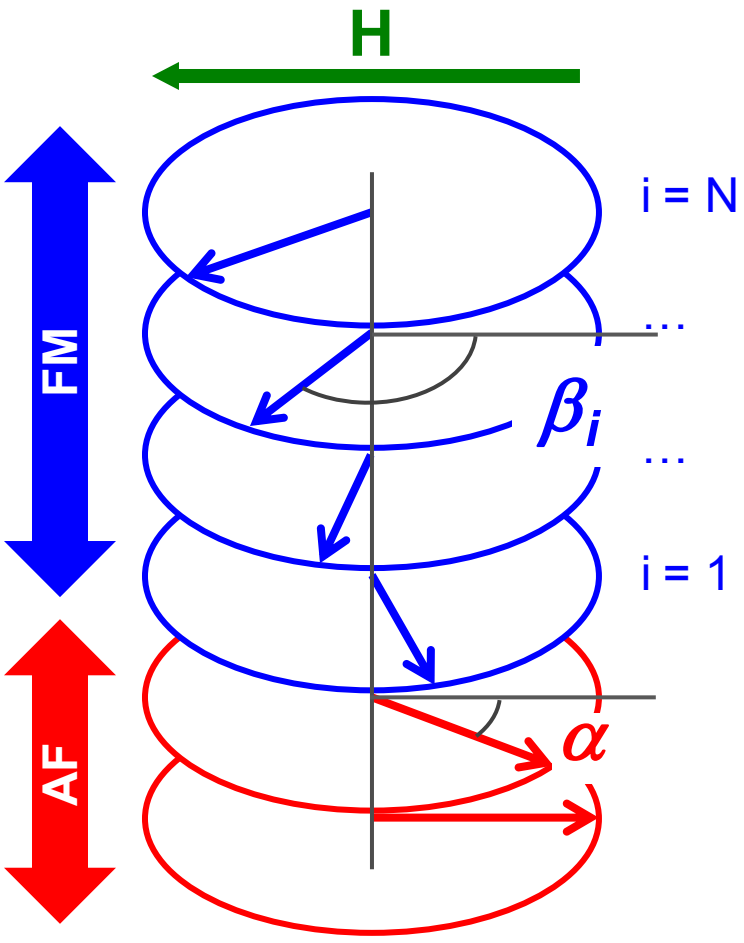

Figure 2. Schematic orientation of net magnetic moments in AFM (red) and FM (blue) layers. The model assumes domain walls parallel to the FM/AFM interface.

The simulation starts from positive saturation where all FM layers are parallel and pointing the same direction. All β_i and α angles were calculated for each magnetic field to minimize the total energy given by equation (1.1). The projection of m_i on the external field axis provides the contribution of the *i.* sublayer to the hysteresis loop. This model successfully predicts all experimental features such as the amount of the exchange bias field, absence of the coercivity, and the asymmetry in the reversal.

1.4. Anisotropic magnetoresistance and planar Hall Effect

Magnetoresistance (MR) measurements have been widely used to investigate the exchange bias and related properties [50-52]. MR is a well-known phenomenon since the first observation by Lord Kelvin in 1856 [53]. It is defined as the change of a material's resistivity with the application of a magnetic field and can be observed in all metals. For non-magnetic metals, MR effect is isotropic and very small (typically less than % 0.1 at low fields). For magnetic metals, however, the effect is anisotropic and large (typically on the order of 2 %). The physics of electron transport in magnetic materials is extremely complicated but is well described in literature [54-56]. The physical origin of the MR effect lies in the spin orbit coupling which is responsible for different scattering lengths along different directions.

Anisotropic magnetoresistance (AMR) is the variation of the resistivity of magnetic materials depending on the angle θ between the current and the magnetization

direction. In order to derive a simple mathematical expression of the effect, we consider an isotropic thin film stripe with four equally spaced *d* point contacts placed on it as seen in Figure 3. A saturating external magnetic field is applied and its direction in the plane of the film varies so that the angle θ of the magnetization *M* varies. When an electric field *E* applied along the x-axis causes a current density J_x. the voltage between points 1 and 2 $V_{12} = E_x.d$ is a measure of the longitudinal electric field along the stripe. The voltage between points 3 and 4 $V_{34} = E_y.d$ is a measure of the transverse electric field which arises because *E* and *J* are not always parallel. Its existence is often called the "planar Hall Effect" (PHE) because devices utilizing it have many functional and circuit similarities to true Hall Effect devices. However, there are many differences from the common Hall Effect, the most important being that the magnetic fields are in the plane of the contacts.

In general, an applied electric field, *E,* induces a current density, *j.* The relation between *E* and *j* depends on the resistivity, ρ, of the material and can be written as

$$j = \frac{1}{\rho} E \,. \tag{1.5}$$

We can decompose E and J as shown at the bottom of Figure 3 to their components parallel and perpendicular to *M*. For longitudinal voltage

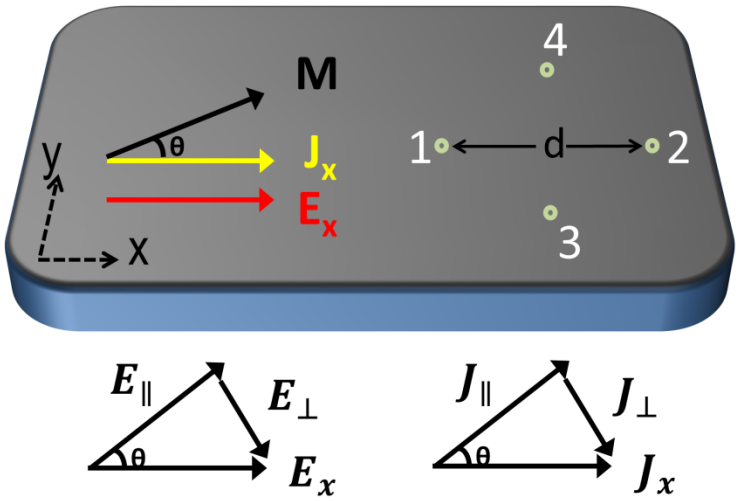

Figure 3. Top: schematic of a thin film stripe with four equally spaced point contacts. A saturating magnetic field is applied in the plane of the film so that the magnetization stays and varies only in the plane. Bottom: representing the sum of electric field and current density vectors for parallel and perpendicular to the magnetization direction used in the derivation of equation (1.6) and (1.11).

$$E_x = E_\parallel cos\theta + E_\perp sin\theta \,, \tag{1.6}$$

$$= \rho_\parallel J_\parallel cos\theta + \rho_\perp J_\perp sin\theta \,, \tag{1.7}$$

$$= J\left(\rho_\parallel cos^2\theta + \rho_\perp sin^2\theta\right), \tag{1.8}$$

$$= J\rho_\perp\left(1 + \frac{\rho_\parallel - \rho_\perp}{\rho_\perp} cos^2\theta\right), \tag{1.9}$$

$$V_{1,2} = J\rho_\perp d\left(1 + \frac{\Delta\rho}{\rho_\perp} cos^2\theta\right). \tag{1.10}$$

Here, $\Delta\rho = \rho_\parallel - \rho_\perp$. Similarly, for the transverse voltage

$$E_y = E_\parallel sin\theta - E_\perp cos\theta \,, \tag{1.11}$$

$$= \rho_\parallel J_\parallel sin\theta - \rho_\perp J_\perp cos\theta \,, \tag{1.12}$$

$$= J\left(\rho_\parallel sin\theta cos\theta - \rho_\perp sin\theta cos\theta\right), \tag{1.13}$$

$$= J(\rho_{\parallel} - \rho_{\perp}) sin\theta cos\theta \ , \tag{1.14}$$

$$V_{34} = J\rho_{\perp} d \left(\frac{\Delta\rho}{\rho_{\perp}} sin\theta cos\theta\right) . \tag{1.15}$$

When comparing the longitudinal and transverse magnetoresistance signals, they have the same magnitude except for a large constant term in the former case. Equation (1.15) shows that the PHE signal is zero when the magnetization and the current are exactly parallel ($\theta=0^0$) or perpendicular ($\theta=90^0$). At $\theta=45^0$ it reaches the maximum value and becomes equal to AMR signal. In fact, they are identical except for a 45^0 phase shift in θ since

$$\cos^2\theta = \frac{1}{2} + \sin(\theta + 45^0)\cos(\theta + 45^0) . \tag{1.16}$$

Figure 4 shows the comparison of normalized AMR and PHE signals as a function of the angel between the magnetization and the current. Except the comparisons mentioned above, the most important difference is that the PHE changes sign from positive to negative at 90° while the AMR remains the same because the angular dependence is proportional to $\cos^2(\theta)$ (equation (1.10)). The amplitudes of PHE signal at 45° and 135° are equal in magnitude but opposite in direction since the sine function is an odd function (equation(1.15)). This gives a unique advantage to PHE measurements: they can be used to distinguish the rotational direction of magnetization during the reversal.

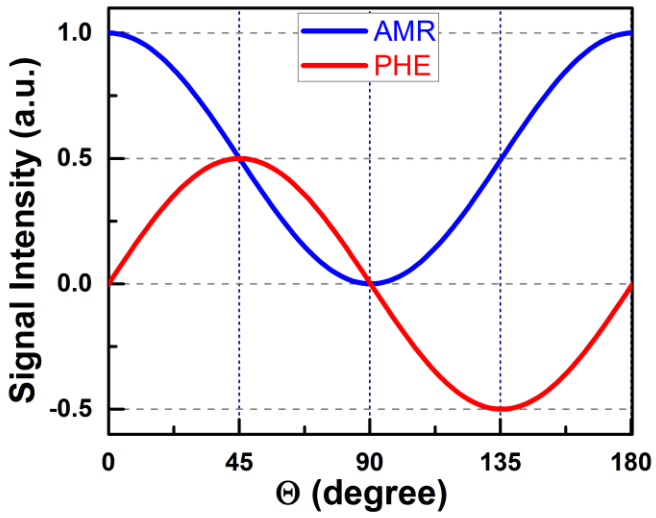

Figure 4. Comparison of normalized AMR and PHE signals as a function of the angle between magnetization and the current.

The advantage of the magnetoresistance measurements and rotation sense can be seen in Figure 5 where SQUID, AMR, and PHE measurements are compared. We assumed a ferromagnet which has two identical domains with exactly opposite magnetic moments, so that the net magnetization is zero in all three cases. Therefore, they are indistinguishable with SQUID, VSM, or MOKE techniques. However, AMR and PHE techniques can distinguish the two configurations in (a) and (b) since the direction of current is either parallel or perpendicular with respect to the magnetization direction. PHE has a further advantage relative to AMR in that it can distinguish the direction of rotation (chirality). If we consider the rotation of the moments from state (a) to state (c), AMR, unlike PHE, cannot separate the difference between up and down rotation directions.

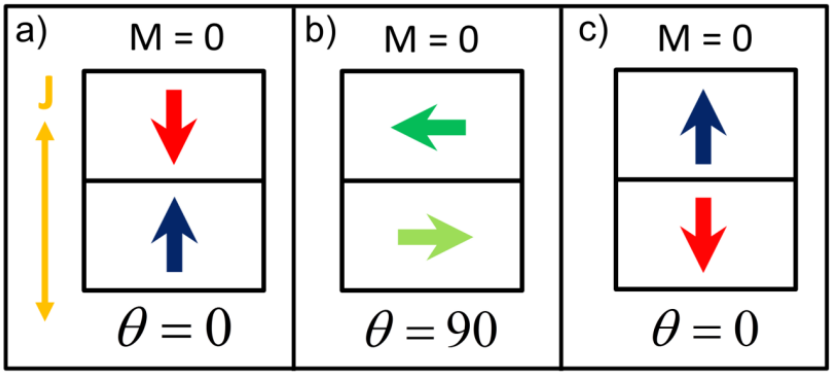

Figure 5. Two identical FM domains with opposite magnetic moments in order to have zero net magnetization. SQUID, VSM, and MOKE techniques cannot distinguish the differences between these three cases. However, AMR and PHE signals can differ between (a) and (b) since the current direction is either parallel or perpendicular to the magnetization, respectively. PHE can be used to separate the reversal from (a) to (c).

This simple picture clearly demonstrates the advantages of magnetoresistance measurements. The averaging nature of standard magnetization measurements hides these important details on the reversal mechanism. The AMR configuration has been more commonly used than PHE. This is related to a more complicated lithographical process required for fabricating PHE devices.

In order to perform a PHE measurement, the ideal shape is a well-defined cross geometry since the current is restricted to flow through one of the wires and the transverse voltage can be measured from the other one. Figure 6 visualizes two different approaches, etching and lift-off, that we used to obtain a cross junction. In both cases, a cross shaped junction was transferred on a sample using a patterned photomask. In the etching process, we start with a bilayer film that was deposited at the same time without breaking vacuum. In the lift-off process, on the other hand, the growth was interrupted

after the first layer to perform the lithography before the second layer deposition. Therefore, the interfacial properties between layers obtained from both approaches are different and must be considered in later characterizations. The steps in both approaches will be explained in the following section.

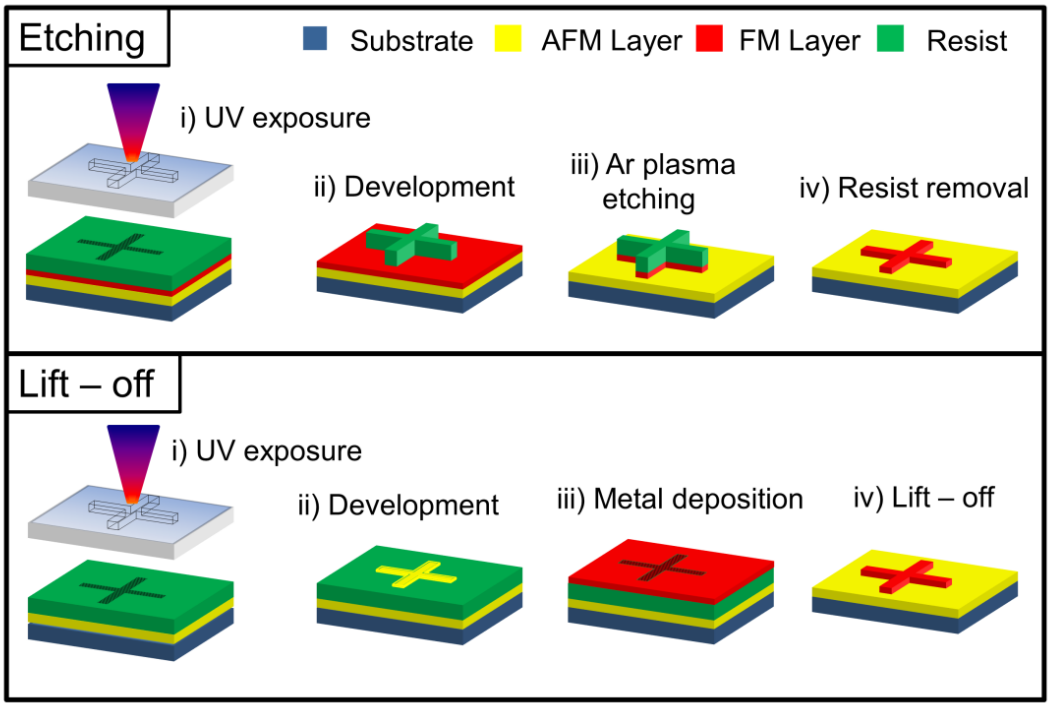

Figure 6. Schematic of the fabrication process of a cross junction by using two different approaches: (up) etching, and (down) lift-off.

1.5. Fabrication techniques

Throughout this thesis studies, we have performed several different experiments which require different sample fabrication techniques. Some of the details regarding the sample fabrication will be given in each particular chapter. Here, we mention only general fabrication techniques such as photolithography and electron-beam evaporation that we used to obtain particularly the cross samples for PHE measurements. Since these standard lithography and growth techniques have been well established and used in all nano-fabrication processes [30, 57-59], we will give only brief recipes generally used in fabrication protocols. A step by step list is given in the appendix.

1.5.1. Photolithography

Photolithography (or UV lithography) is a widely used technique for large areas with custom features. We used either a Karl Suss MJB 3 or Karl Suss MA6 mask aligner that allow feature sizes as small as 1 μm. 0.06" thick and 3" in diameter iron coated photomasks for custom designed devices were bought from Advanced Reproductions Corporation. A positive tone (Microposit S1818) and a negative tone (Futurrex NR9-1500PY) resists were used for photolithography.

Before starting the lithography process, the mask should be cleaned in ultrasonic bath with Acetone, Methanol, and Isopropanol (~ 5 minutes for each). The mask was then rinsed in deionized water and dried with flowing nitrogen gas. This process helps

remove the residual resist from the previous use and to obtain cleaner features (especially when features are smaller than 2 μm).

The S1818 was spun on the sample at 5000 RPM for one minute and then baked at 115 °C for one minute on a hot plate. The resist was exposed to UV light for ~ 3.5 minutes at an exposure power of ~ 0.4 mW/cm^2. The required time changes from time to time probably due to power changes, so it should be checked occasionally. After exposure, no post baking was performed for the positive resist. It was directly developed in 1 part deionized water and 1 part AZ developer for approximately 40 s. After rinsing in water for 20 s and drying out by blowing nitrogen gas, the sample is visually checked by an optical microscope to confirm that the pattern transferred properly. Once the sample was ready, the resist could be removed in Acetone.

The negative NR9-1500PY resist was spun on the sample at 4000 RPM for 40 s. The resist was then pre-baked at 150 °C for one minute on hot plate. The exposure was performed for ~ 3.5 minutes at a power of ~ 0.4 mW/cm^2. Once exposed the sample was post-baked again at 100 °C for one minute on hot plate and then developed for ~ 40 s in pure RD-6 resist developer while agitating the sample by hand. The sample was then immersed in deionized water in two separate beakers and agitated for approximately 20 s for each time. This process ensures that no resist particulates were left on the sample after development. Once processed, the resist was removed by immersion in acetone at least for 6 hours. A low power sonication was usually required for about 30 s to obtain the desired features. The sample was rinsed in Isopropanol and deionized water and dried out with nitrogen.

1.5.2. Electron beam lithography

During different sample fabrications, we have used a combination of photolithography and electron beam lithography techniques which is widely used to obtain especially for sub-micron feature sizes. We have used two different systems: a JEOL JSM 6400 scanning electron microscope that has been converted to an electron beam writer using the nano pattern generation system (NPGS), and RAITH 50 electron beam lithography tool. The later was used when alignment required for a multistep lithography process.

We have used Polymethyl methacrylate resist (PMMA) from Microchem Corporation. Typically we used C4-950PMMA as a single layer resist. In some cases, we used a combination of A2-950PMMA/C4-495PMMA as a double layer resist to achieve clean edges. PMMA was spun on the sample at 6000 RPM for one minute and then baked at 195 °C for six minutes on a hot plate. The patterns were written into the resist with typically 20 nm step size, 30 kV acceleration voltage, 100 pA current, and 500 $\mu C/cm^2$ dose. Once the pattern was written into the resist, the sample was developed in 1 part methyl isobutyl ketone (MIBK) and 3 parts Isopropanol for 40 seconds. The sample was rinsed in Isopropanol for 20 seconds to stop the developing and then dried with nitrogen gas. After the materials depositions, the lift-off can be done removing in acetone for at least 4 hours. The sample was rinsed again in isopropanol and deionized water, and dried with blowing nitrogen gas.

1.5.3. Etching

Etching was employed in the fabrication of exchange biased cross junctions. The benefit of plasma etching is that the bilayer can be deposited at once without breaking vacuum and then only the top FM layer should be etched to obtain the cross. Therefore, the interface between AFM and FM layers will not be touched by any lithographic process.

We used Oxford Plasmalab 80 reactive ion etching instrument. The base pressure was better than $1x10^{-5}$ Torr before starting the process. The process pressure was kept at 25 mTorr with 40 sccm Ar flow. The power was 200 W and the measured reflected voltage was 540 V. Under these conditions, the etching rate of Ni was found to be approximately 3 nm/minutes.

We have found that the negative NR9-1500PY resist is good enough as a mask to etch 10 nm of Ni. Even though the etching time was less than 4 minutes, it is hard to remove the resist without sonication. Special care must be given during the sonication since the cross junction is extremely delicate.

1.5.4. Film growth

The samples including in this dissertation are mainly grown in a Kurt J. Lesker electron beam evaporation system with a typical base pressure of $1x10^{-7}$ Torr. The system is equipped with a 4 hearth 7 kW Temescal electron beam gun, a liquid nitrogen

cold trap, a copper block heater, and a step motor controlled shadow mask. The sample holder is located right above the evaporating materials. This allows more directional deposition without hitting the patterned edges, improving the definition of the features.

A sputtering system (Microscience) equipped with AC and DC power supplies was also used for various depositions, especially for the outer contacts and in-situ Ar ion milling. The sputtering chamber operates at a base pressure of ~ $2x10^{-7}$ Torr. Due to the nature of the sputtering technique materials can be deposited on all surfaces of the sample, including the walls of the resist. This can be a problem during the lift off process and produces fences at the edge of the features. A double layer resist with a less sensitive resist layer on the top and a more sensitive resist layer on the bottom was used to overcome this problem.

For the fabrication of the cross junction both deposition methods were used. For lift off samples, first FeF_2 layer was deposited in the evaporator. Afterwards, the sample was taken out from the chamber and a cross junction was shaped by photolithography. The sample then was introduced into the sputtering chamber and ~ 3 minutes of Ar ion milling was performed with 50 W and 4 mTorr pressure by applying a bias onto the sample holder. When sputtering Ni, the Ar gas was flowed through the chamber and pressure was maintained again at 4 mTorr while 100 W of power was applied to the target. Following the sample was taken out from the sputtering chamber for the lift off process. After the lift off for Ni and another photolithography for outer contacts, a Ti (10 nm) / Au (90 nm) deposition was performed in a different sputtering chamber (In fact, this second sputtering system is identical to one described above and called as

Microscience-II). Before Ti deposition, the Ar ion milling was also performed with the same parameters above. The Ti layer was deposited to achieve an adhesive layer for Au. More details for sample preparation can be found in Table 1 in Appendix A.

The first Ar ion milling step is important for maintaining a clean FeF_2 / Ni interface, which is critical for exchange bias. If this step was not performed, exchange bias was not observed. However, different samples prepared using the aforementioned recipe were not the same in terms of the exchange bias properties. This is probably related to our inability to control ion milling and to obtain similar interfaces in different samples. The second Ar ion milling before Ti deposition is also very important to remove the residual particulates from the photoresist and to eliminate the high contact resistance.

In the other approach, a FeF_2 / Ni stack was deposited as a bilayer in the evaporator without breaking the vacuum. Following the lithography and etching processes described above, the Ti / Au outer contacts were deposited in the Microscience-II sputtering system. The Ar milling and the deposition conditions were kept the same as in the first approach. We found that the samples grown as bilayers show very reproducible exchange bias properties. Therefore, in chapter 2 we include only the results from the samples that were made of etching process. More details for sample preparation can be found in Table 2 in Appendix A.

1.6. Measurements

The transport measurements were mostly performed in a Quantum Design DynaCool system. It has a cryogen free chamber with a superconducting magnet up to ± 9 Tesla. The accessible temperature range is 1.8 K – 400 K. Electrical transport option allows measuring the AC and DC resistance with 1 nV sensitivity. A horizontal sample rotator can be used at angle ranges from -10 to 360 degrees (see Figure 7 (d)). The rotator has its own thermometer close by the sample chip for more accurate temperature reading. The system is combined with a pair of Keithley electronics (typically a 2182A nanovoltmeter and 6221 AC and DC current source) and a custom made switch board from Wimbush Science and Technology. The communication between electronics and the chamber is established using a custom designed LabVIEW program.

The sample was connected to the sample holder using a double sided tape. In order to establish a good thermal conductivity, the sample is in direct contact with He gas flow. We used highly insulating substrates, i.e., MgF_2, to avoid electrical shorts between the device and the system. Indium solder was used to connect the wires to the chip (sample holder). Sometimes the device was broken due to the heat induced by the soldering iron, especially on the sample side. Therefore, we have taken special care to not burn the sample, which can be done by using silver paste to mount the wires onto the sample (Figure 7 (b)).

The chip fits onto the horizontal rotator as seen in (Figure 7 (c) and (d)). There is a separate thermometer at the bottom side of the chip (not seen). There are 14

channels coming out from the probe to access the contacts and the thermometer. The probe together with the vertical sample puck allows full circle rotation, either clockwise or counterclockwise directions, while the applied magnetic field always stays in the plane of the sample. The rotation is externally controlled by a motor through a goniometer with better than 1 degree precision.

Before installing the probe into the chamber, all contacts were checked to make sure the devices have proper resistance between all contact pairs. A typical cross junction has ~ 500 Ω resistance between any two contacts at room temperature. In AMR measurements with the cross samples, only a combination of any two contacts can be used. Therefore, in such two probe configuration, there are additional inline contributions to the total device resistance, e.g., Au pads, sample wires, probe wires, switch board, etc. The switching between the contacts was done using the switch box without taking the probe out.

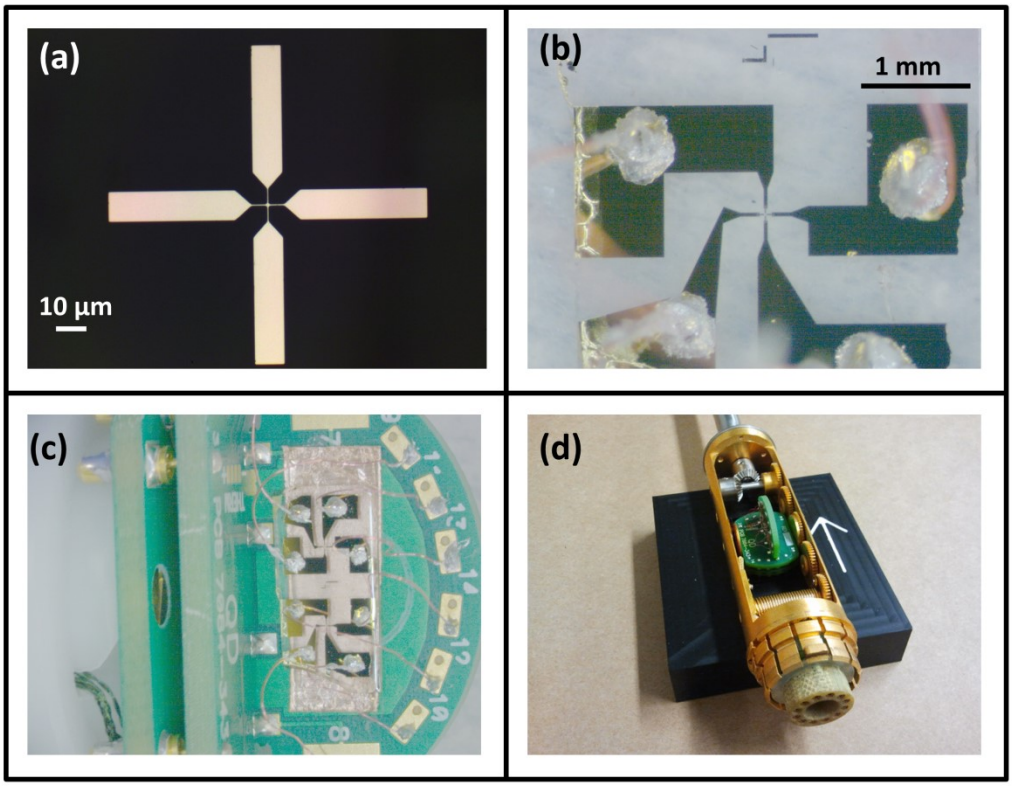

Figure 7. Various stages of sample preparation and mounting for transport measurements. (a) Patterned cross junction, (b) outer Au contacts with indium soldered wires, (c) vertical sample puck, and (d) horizontal sample rotator. The applied magnetic field is along the white arrow in (d) so that the field stays in the plane of the sample during the rotation.

2. Magnetization reversal in Ni/FeF_2 cross junctions

In this chapter, we will discuss the general exchange bias properties of our model exchange bias system, Ni/FeF_2. We combined two magnetoresistance measurement techniques to study the magnetization reversal mechanism in a lithographically patterned conducting ferromagnetic (Ni) cross, coupled to an insulating antiferromagnetic film (FeF_2). These two techniques are based on the planar Hall Effect (PHE) and anisotropic magnetoresistance (AMR), and together allow us to determine the magnetization reversal mechanism in exchange-coupled Ni/FeF_2 crosses. We found that the PHE, in contrast to AMR, is very sensitive to the direction of rotation of the magnetization. We investigated the dependence of the reversal mechanism on the direction of the unidirectional anisotropy axis with respect to the applied magnetic field. Small deviations around the crystallographic easy axis revealed the presence of a tight angular distribution of anisotropy axes. These axes are slightly tilted in opposite directions around the average easy axis and determine the magnetization reversal mechanism. This is confirmed with simulations using the incomplete domain wall model [60, 61]. We show how to use PHE measurements as a precise tool to probe the angular distribution of the unidirectional anisotropy axes and the magnetization rotation direction (chirality). Furthermore, we studied the rotational dependence of the magnetization of Ni/FeF_2 crosses. Clockwise (CW) and counterclockwise (CCW) rotations of the sample revealed a hysteretic magnetization switching around the most

unfavorable orientation: along the easy axis but opposite to the unidirectional anisotropy easy axis. A competition between the applied magnetic field and the unidirectional anisotropy determines the width of the angular hysteresis. We simulated the angular dependences of the PHE and AMR measurements using the same model and parameters as for the hysteresis loops. The experimental and simulated data are in excellent agreement for all geometries and magnetic field values.

2.1. Introduction

Exchange bias is a result of the unidirectional magnetic anisotropy which is caused by interfacial exchange coupling, typically between a FM and an AFM layer [3]. There are several characteristic features associated with exchange bias, among which the best known are the shift of the center of magnetic hysteresis loop and the accompanying enhancement of magnetic coercivity [2]. These features can be determined either by direct measurement of magnetization or indirectly from magnetotransport measurements, e.g., from the AMR or the PHE. The measurements from SQUID or VSM techniques include the magnetic contribution of the substrate and the sample holder. Moreover, it is always a challenge to investigate the magnetization reversal process in nanomagnetic systems, such as wires and junctions, because the magnetic signal from such structures is relatively weak. Most conventional microscopy techniques are resolution limited. To solve this problems, magnetotransport measurements have commonly been used to characterize the magnetic properties in

various magnetic nanostructures [62-64], thin films [55, 65, 66], nanodots [67], nanowires [65, 68-71], nanopillars[72], nanoconstrictions[73], nanohole arrays[74], and other such systems.

As compared with AMR, the PHE signal is more sensitive to changes in the local spin configuration and has much lower background voltage. Because of this, the PHE is mostly preferred in applications in sensor technologies, such as magnetic nanobead detection [75] and biosensors[76, 77]. It has been shown that using the PHE, a low field magnetic field sensor with a minimum detectable field that is less than 10 nT and four orders of magnitude less thermal noise than in AMR is possible [78]. Other advantages of the PHE geometry are the ability to sense the magnetization rotation direction as shown in exchange biased (Ga,Mn) As / MnO heterostructures [79] and the ability to determine the vortex chirality in a magnetic nanodot [80]. The PHE has been also used in the investigation of the reversal mechanism in magnetic nanowires [81-84], exchange coupled thin films [79, 85] and submicrometric wires [86]. However, AMR geometry has been more commonly used due to the specific geometry and fabrication requirements of the PHE measurements.

We employ the PHE as a very sensitive technique to investigate the magnetization reversal in our prototypical exchange bias system, Ni/FeF_2. In general, TM / FeF_2 (TM refers to transition metals such as Ni, Fe, Co) systems are of particular interest due to the presence of features such as positive exchange bias [27], magnetization reversal asymmetry [44, 50, 87, 88], and anomalous temperature dependence [28]. These systems have been suggested for use in multi-digit storage

technologies because of the coexistence of positive and negative exchange bias [89]. Therefore, there is a significant interest in understanding the details of the magnetization reversal mechanism in such systems. It is possible to study the reversal of magnetic moments using the transverse magneto-optical Kerr effect [87] and vector vibrating sample magnetometry [90]. However, for small feature sizes these techniques require arrays of elements, while PHE can probe individual nanostructures. Furthermore, PHE has a unique advantage compared to more sophisticated experimental techniques like polarized neutron reflectivity [44] and standard AMR geometry [50] that were found to be insensitive to the direction of transverse magnetic moments. The disadvantage of the PHE technique is that a more complicated lithographical process is required for fabricating PHE devices.

In this chapter, we present the PHE and AMR techniques used to determine the magnetization reversal mechanism in exchange-coupled Ni/FeF_2 crosses. We found that there is a narrow distribution of unidirectional anisotropy axes, which corresponds to a distribution of pinned magnetic moment directions around the average crystallographic easy axis. Small angle variations around these axes change the magnetization rotation direction and produce opposing PHE signals. The rotational dependence of the magnetization of Ni/FeF_2 crosses was studied at higher angles by CW and CCW rotations. An angular hysteretic behavior found depending on the strength of the applied magnetic field. The magnetic field and angular dependences of the PHE and AMR measurements were simulated for this patterned structure. Experimental and simulated data are in excellent agreement for all geometries and magnetic field values.

2.2. Sample fabrication

The Ni/FeF_2 heterostructures were obtained after several film growth and lithography steps. Antiferromagnetic FeF_2 was grown on a 5 mm x 10 mm (110) MgF_2 substrate by using an electron beam evaporator. Before deposition, a base pressure of $1x10^{-7}$ Torr was achieved by pumping a turbo pump for at least 6 hours and using a liquid nitrogen cold trap. Next, the heater was set to 500 $^{\circ}$C for an hour. This removed any residue (degassing) from the holder and substrates. The temperature was reduced to the FeF_2 deposition temperature (300 $^{\circ}$C) and kept for 30 minutes before the deposition. 100 nm of FeF_2 and 10 nm of Ni were deposited with a rate of 1 Å/s at 300 $^{\circ}$C and 150 $^{\circ}$C, respectively. During the deposition, special care was given to keep the maximum pressure of the chamber below $6x10^{-7}$ Torr. Under these conditions, FeF_2 and Ni are grown epitaxially and into a textured polycrystalline film, respectively.

The cross junction was fabricated by a combination of standard photolithography and etching techniques (Figure 8). A second photolithography step and a deposition step were required to obtain the top Ti (10 nm)/Au (90 nm) contacts for the transport measurements. In this step, a 10 nm layer of Ti was deposited to obtain an adhesive layer for the Au. The top contacts were deposited in a sputtering chamber with 2 x 10^{-7} Torr base pressure. The argon gas flow was set to 4 mTorr during the entire deposition process. 3 minutes of argon ion milling was performed in-situ by applying a 50 watt RF bias to the sample holder right before the Ti deposition. This

milling removed the photoresist residue. The details of lithography steps were given in chapter 1.

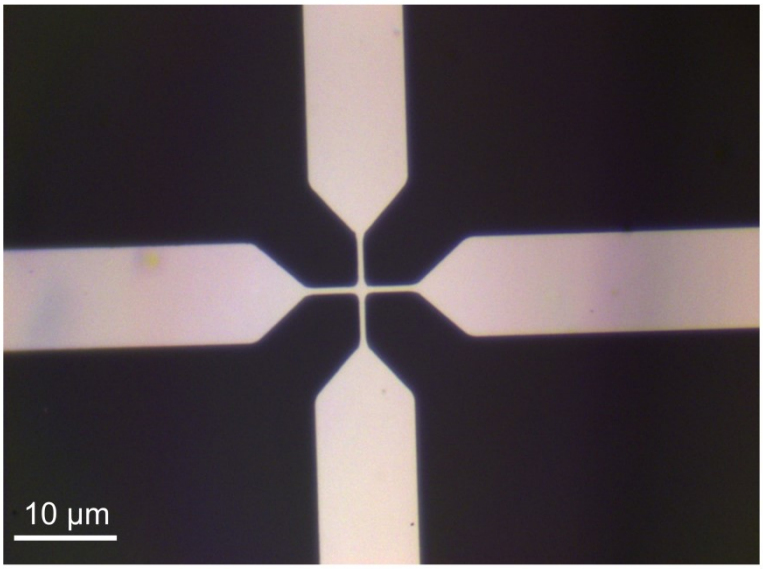

Figure 8. A microscope image of a cross junction used in AMR and PHE measurements. The black background is FeF_2 and silver cross is Ni. Ni/FeF_2 bilayer was deposited in an electron beam evaporator and the cross was shaped by photolithography and etching processes. The photoresist was used as a mask during etching.

2.3. Magnetic characterization of Ni/ FeF_2 bilayers

In order to check the magnetic and exchange bias properties of the sample obtained from magnetotransport measurements, a ~ 5 mm x 5 mm 'sister sample' was grown at the same time. This was kept as a reference sample without doing any further lithography processes. Figure 9 (a) and (b) show VSM measurements of a FeF_2 (100 nm) / Ni (10 nm) bilayer at 300 K and 5 K, respectively. The hysteresis loop at 300 K shows a square shape with a remnant ratio of $M_r / M_s = \sim 1$ and coercive field of 30 Oe

(here, M_r and M_s refer to remnant and saturation magnetization, respectively). The measurement at 5 K was recorded after 50 Oe field cooling. It shows a reversible magnetization rotation and there is no loop opening within our experimental uncertainty (Figure 9 (b)). The magnetic field was swept from the positive to negative saturation with a speed of 20 Oe/s. The diamagnetic contribution from the substrate was corrected by subtracting a negative linear slope -1. The exchange bias field is ~ - 1.6 kOe. The lack of a coercive field and a clear large loop shift shows that our archetypical exchange bias samples represent an ideal system to study exchange bias and related properties. The asymmetry in the magnetic reversal at 5 K will be discussed later on this chapter.

We simulated the VSM data with the incomplete domain wall model (introduced in chapter 1) at 5 K where the magnetization rotation mechanism is reversible. Simulated $M(H)$ curves are shown in Figure 10, compared with experimental data taken at 5 K. The parameters used in the model were: $A_{AF} = 3.1\times10^{-8}$ erg/cm, $K_{AF} = 1.35\times10^{8}$ erg/cm^3 [18, 91], $J_{AF-FM} = 0.92$ erg/cm^2, $J_{FM} = 5.6$ erg/cm^2 as obtained from the fit of the M(H) curve. $K_{FM} = 5\times10^{3}$ erg/cm^3 was obtained from hard axis hysteresis loop and m_i was calculated from the Ni magnetization $M_{Ni} = 484$ emu/cm^3 using $m_i = M_{Ni}\Delta t_{FM}$.

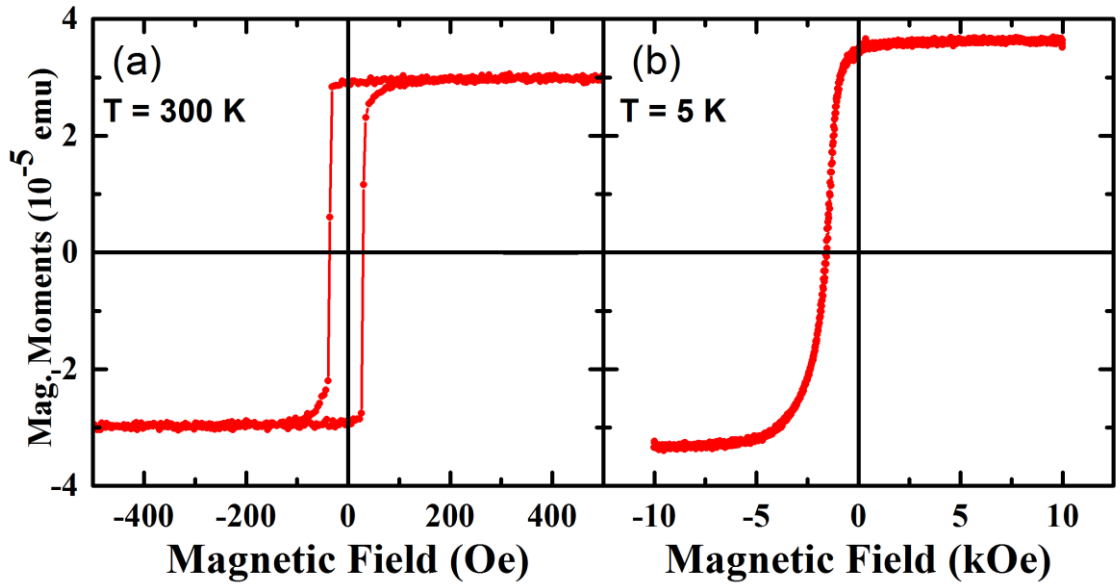

Figure 9. Hysteresis loops for a FeF_2 (70 nm) / Ni (10 nm) bilayer at 300 K (a) and 5 K after 50 Oe field cooling (b).

The thickness of each FM sublayer Δt_{FM} was taken as 1 nm. The simulation followed the shape of the hysteresis loops very well showing both a fast decay in the magnetization approaching the exchange bias field and a slow saturation at negative fields. The model predicts a reversible magnetization reversal mechanism, which was confirmed by VSM measurement. The exchange bias value is in good agreement. We used the same parameters to explain the PHE and AMR measurements of the cross junction.

2.4. Initial magnetic characterization and magnetoresistance measurements

In our prototypical exchange bias system (Ni/FeF_2), FeF_2 is an insulating material and therefore the magnetoresistance measurements probe only the ferromagnetic Ni layer.

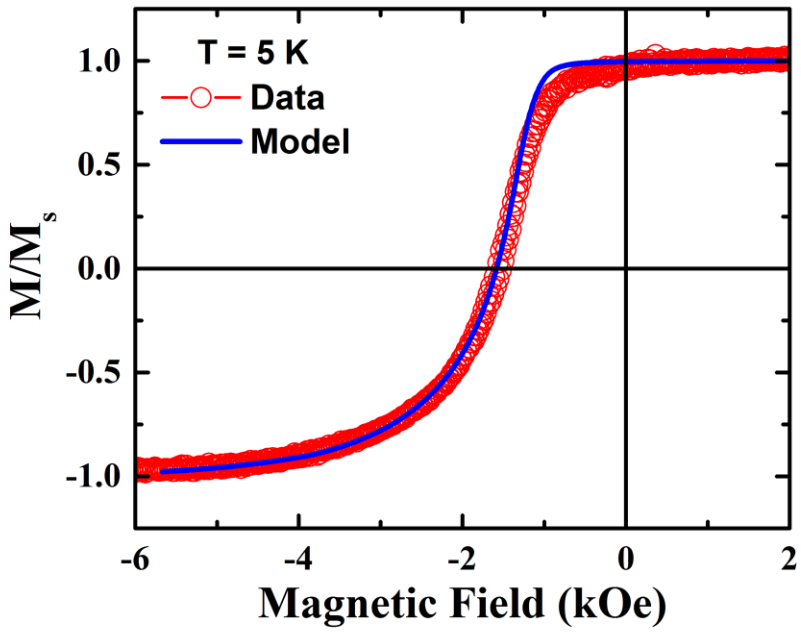

Figure 10. Comparison of the simulated data and the VSM data at 5 K after 50 Oe field cooling. The solid blue line is calculated from the model introduced in chapter 1, using the parameters given earlier in this chapter. The open red circles are the VSM data.

Hence, the contribution of the AFM bulk is excluded. Measurements above the Neel temperature of FeF_2 enable us to study the reversal of Ni in the absence of the exchange coupling. Conversely, measurements below this temperature enable us to study the presence of exchange coupling. We chose Ni as a high anisotropy

ferromagnetic material and a thickness of 10 nm to minimize the effect of the spin configuration in out-of-plane direction (see chapter 4 for the effect of FM layer). However, the asymmetry in the reversal process indicates the presence of in-depth FM domain walls [44, 45]. This implies that the magnetoresistance measurements in our FeF_2 / Ni heterojunctions can be used to probe the FM layer, although these measurements are strongly governed by the interfacial properties.

Figure 11 shows a photograph of one of the measured samples with soldered conducting wires. There are two identical but independent devices (grown and patterned at the same time) on the same sample. The numbers on the contacts represent the channel numbers for the transport probe. Up to eight contacts can be connected simultaneously to the sample, but only two to four of those contacts were used for any given measurement. We can switch between different contacts by selecting the corresponding channel on the switch board (see chapter 1 for more details). A typical sample showed ~ 500 Ω resistance between any two contacts at room temperature. During the PHE measurements, typically 1 mA current was passed from contact 5 to 7 or 3 to 9. The voltage values were recorded automatically between contacts 3 and 9 or 5 and 7. Hence, the electrical potential difference between transverse contacts was dominated by the PHE at the junction, which is given in equation(1.15).

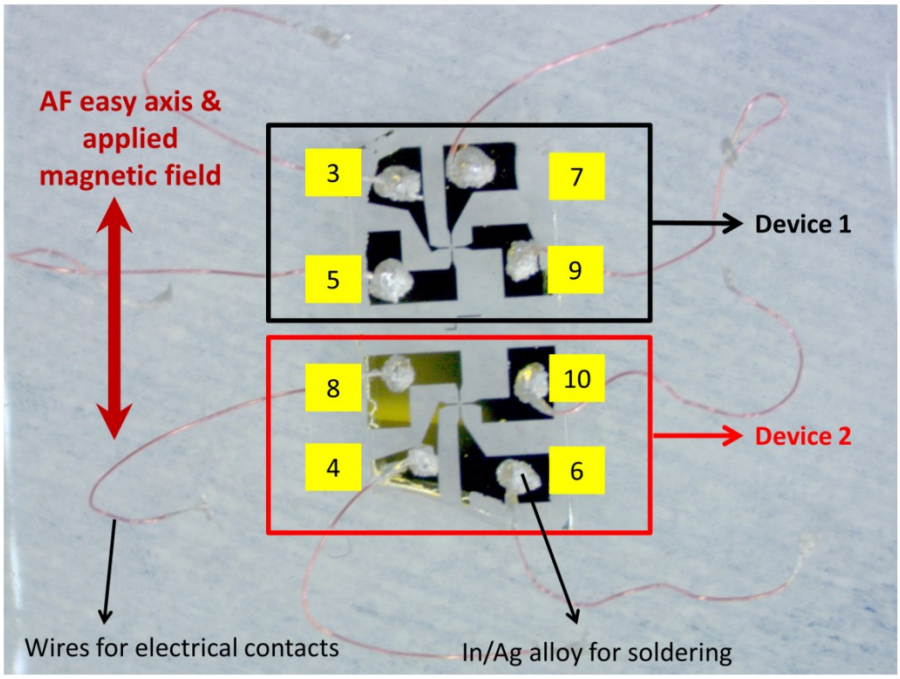

Figure 11. A photograph of a measured sample. Two independent devices are shown as device 1 (top) and device 2 (bottom). The numbers correspond the channel numbers on the transport probe. The applied magnetic field is along the long axis of the sample which is also the AFM easy axis as indicated with a red arrow. The conducting wires are soldered to Au pads with Indium (includes 10 % of silver).

Figure 12 (a) and (b) show magnetoresistance measurements at room temperature for current parallel and perpendicular to the applied field, respectively. Before starting the measurements, a + 1 kOe field was applied along the axis of the wire and parallel to the film plane. This was determined to be sufficiently large to saturate the magnetization in the positive direction. The field was swept from positive to negative saturation at a speed of 10 Oe/s and then back to positive saturation at the same speed.

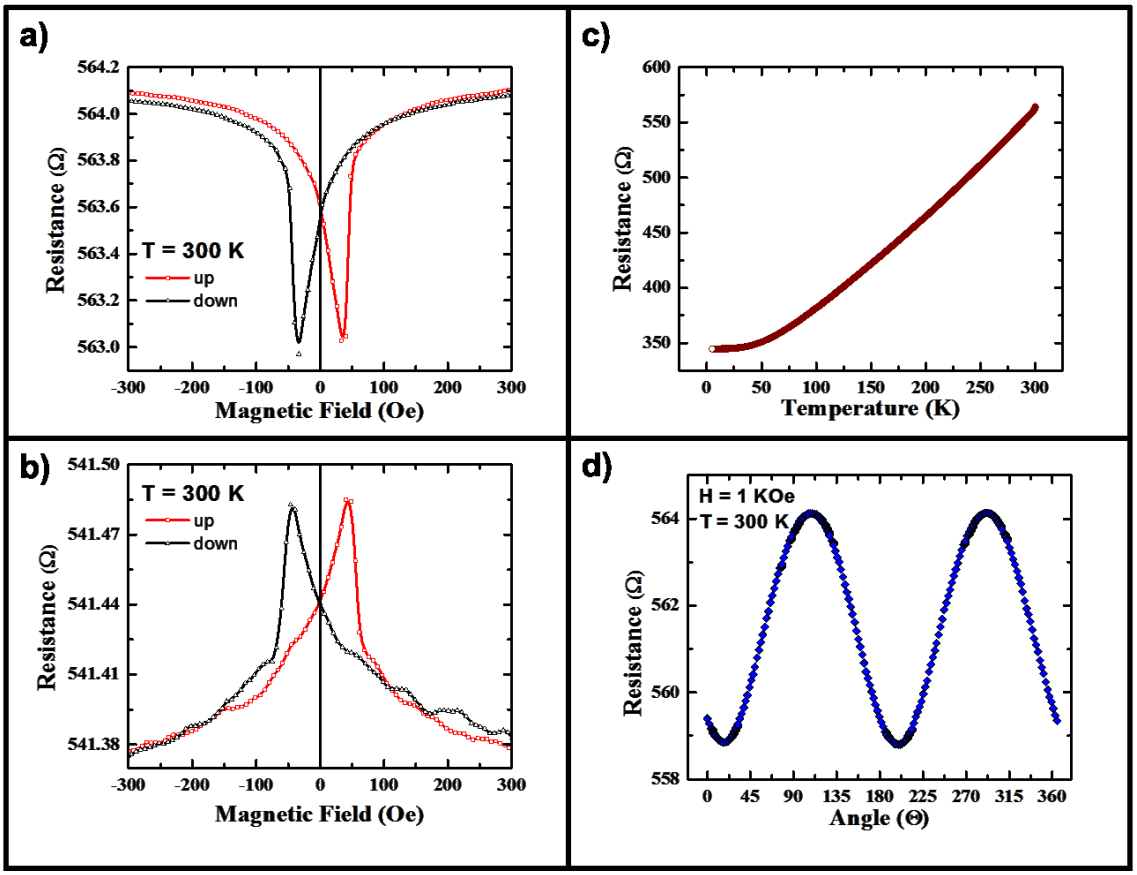

Figure 12. Initial characterization of the sample. (a) and (b) are the magnetic field dependence of the sample at room temperature for current parallel and perpendicular to the applied field, respectively. (c) is a typical temperature dependence and (d) shows the angular dependence of the AMR configuration with 1 kOe applied field.

During the field sweeps, the behavior of the resistance was reversible and reproducible until the sweep passed the resistance minimum (or maximum, for the case of current perpendicular to field), which occurred at approximately ± 40 Oe. Once this field was passed the behavior becomes hysteretic. Since hysteresis is associated with the presence of domain walls, this indicates that domain walls first formed in the sample at ± 40 Oe. This field also corresponds to the coercive field of the device.

The VSM measurement of the "sister" sample introduced in chapter 2.3 shows very sharp switching with a ~ 30 Oe coercive field (see Figure 9). The difference between the VSM and AMR measurements could be associated with patterning (the shape of the cross). At the intersection of the arms of the cross, the shape anisotropy from each arm will be in competition and induce a new total magnetic anisotropy, which requires a higher coercive field compared to the film. This is further supported by the shape of the AMR curves which show a slow approach to the minimum (or maximum) and sharp switching afterwards, suggesting the magnetization reversal occurs by a combination of rotation and domain wall motion related mechanisms induced by the cross shape.

The AMR signal was recorded during 50 Oe field cooling (Figure 12 (c)). This temperature dependence is typical for a metal and there is no anomalous feature across the Neel temperature of FeF_2. To find the exact easy axis of the device, prior to field cooling, the sample was rotated in a 1 kOe applied field and AMR signal was recorded (Figure 12 (d)). The angular dependence shows a 4-fold symmetry, which is expected since the applied field is high enough to keep the magnetization direction along the field axis. Therefore, the angle between the current and the magnetization direction changes as the sample is rotated. The easy axis was found to be at 107° with respect to the measurement zero. This initial angular test at room temperature allows us to determine the easy axis of the device and perform the field cooling at a precisely known angle, which is necessary to determine the dependence of exchange bias on cooling angles.

Before field cooling, a 1 kOe magnetic field was applied to saturate the cross junction along the FM easy axis of the sample, which coincides with the wire and AFM easy axes. The field was reduced to 50 Oe (the cooling field) and kept at this value during cooling to 5 K with a typical rate of 4 K/minute. The first measurement was started after 2 hours to obtain ~ 1 mK thermal stability.

2.5. Direction of magnetization rotation sense

Figure 13 shows the PHE measurement of the cross junction after it is field cooled to 5 K. These PHE measurements represent the zero degree case (respect to the easy axis) since they were obtained right after cooling without any rotation. The measurement started with the field at positive saturation (10 kOe). The field was swept with a 20 Oe/s speed first towards the negative saturation (red, downward) and then back to the positive saturation (black, upward) to complete the cycle. The junction shows a -1.64 kOe exchange bias field, in good agreement with the VSM data from the 'sister sample' (see Figure 10). Running this cycle more than 5 times gave very similar curves with only a few minor changes in the noise level. The details of the PHE signal and its interpretations were given in chapter 1. Significant difference between upward and downward sweeps is remarkable. Here, we will discuss the main features of the data obtained from the PHE measurements in comparison to AMR (Figure 14). AMR measurements were done just after the PHE by changing the contact leads without other changes in the sample or magnetic field orientation.

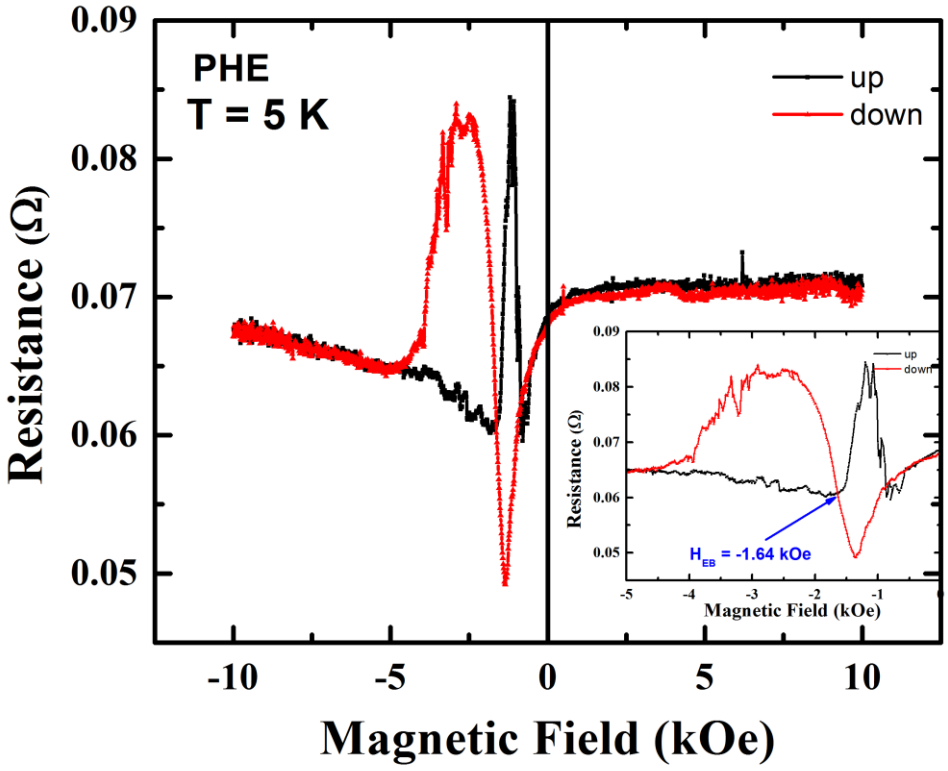

Figure 13. PHE measurement at 5 K after 50 Oe field cooling. The inset is an enlarged view around the switching fields. The black and red symbols correspond to upward and downward sweeps, respectively.

Both upward and downward AMR curves for zero degrees respect to the easy axis are included in Figure 14 (a). The resistance changes by ~ 1.2 % with respect to the saturation value. The remnant resistance at zero field is about the same as the resistance at the positive saturation, which indicates that a strong coupling has been established at the interface. The asymmetric reversal is clearly seen from the relatively sharp decrease on the right hand branch while slow approach to the saturation on the left. The general shapes of the curves, which are determined by the change in the magnetization direction

respect to the current, are in a very good agreement with VSM measurements (see Figure 10). There is virtually no coercivity between upward and downward sweeps. This indicates the magnetization reversal occurs via rotation of magnetic moments. The small angle variations (± 4°) around the easy axis appear as small changes only on the high field side of the loops, i.e. as a slower approach to negative saturation (Figure 14 (a)). This can be explained considering the required applied field varies to achieve the negative saturation depending on the angle between the applied field and the easy axis.

On the other hand, in the case of 0°, the presence and absence of the significant difference between upward and downward sweeps in PHE and AMR measurements, respectively, can only be explained by a change in the magnetization rotation direction (see chapter 1 for more details about the sensitivity to the direction of rotation for each technique). The signal shape of the PHE measurements (Figure 13) proves that the magnetization reversal occurs in a full circle rotation. However, the magnetization is expected to have an equal probability of rotating CW or CCW directions if neither one is energetically favorable. Repeating the same measurement several times results in similar data. Moreover, there is a large difference in the intensities (the relative change in the resistance values) between the 0° and ± 4° in the PHE measurements (see Figure 14). This indicates that there should be an additional mechanism to reduce only the PHE signal at 0°. The origin of the change in the magnetization rotation directions (chirality) between upward and downward sweeps and the intensity decrease at 0° needs to be further considered.

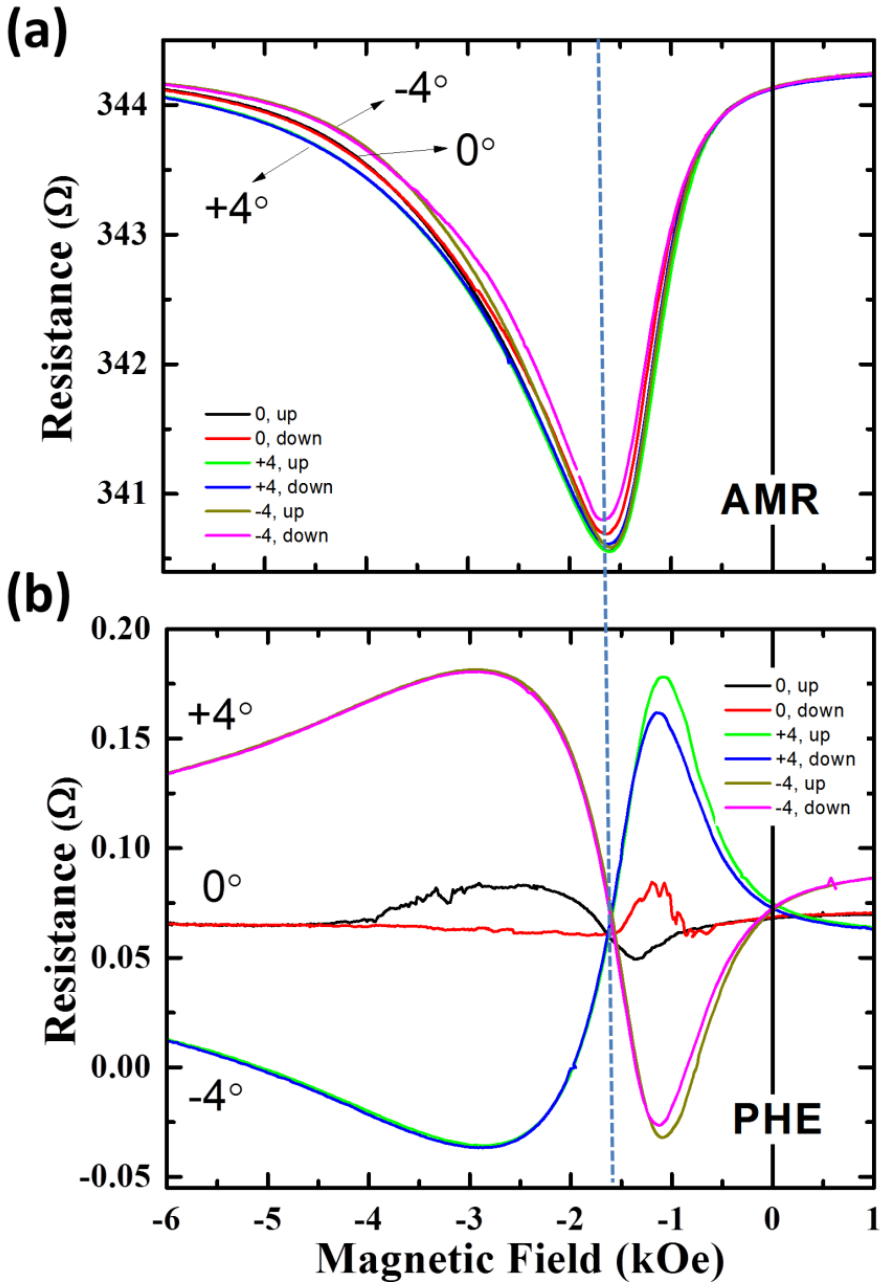

Figure 14. Comparison of AMR and PHE measurements for the small angle variations (±4°) around the easy axis (0°). Both upward and downward sweeps are included for each angle. The PHE curves clearly show the differences in rotation directions.

To explain these measurements we assume the presence of two different directions of pinned moments, which are slightly tilted from the average

crystallographic easy axis in opposite direction as seen in Figure 15. Directions of pinned moments are indicated using the blue and red arrows with easy axis 1 and 2 labels (EA_1 and EA_2, Figure 15 (b)). The average crystallographic easy axis is shown with the green arrow and labeled as unidirectional anisotropy axis (UA). The direction of the external magnetic field is fixed (the black arrow). This assumption does not exclude the presence of moments, which are at zero degrees or other possible directions, but it is used to simplify the problem. We further assume that the average distribution of the moments that are aligned in the EA_1 direction is higher than in EA_2. If the magnetic field is applied at a small angle (±4°, Figure 15 (a) and (c)), the magnetic moments in each easy axis are forced to follow the same rotation direction (CW or CCW; depending on the angle of the applied field). When the field is reversed, the magnetic moments in both axes rotate back following the opposite rotation direction. This is due to the strong unidirectional anisotropy that forces the moments to be aligned only in one direction. Therefore, a semicircular rotation of magnetic moments occurs during a full magnetic field cycle.

When the magnetic field is applied at zero degrees, the moments in two easy axes are forced to rotate in opposite directions (CW or CCW) as seen in Figure 15 (b). In this case, the projection of the applied field simply determines the preferred rotation direction. Similarly, when the applied field is reversed, moments in the both easy axes return to the initial positions by rotating in the same direction as they did previously. Therefore, the moments in each of the easy axes complete a full circle rotation. The

average PHE signal that we measure in our experiments arises from the sum of these two individual rotations.

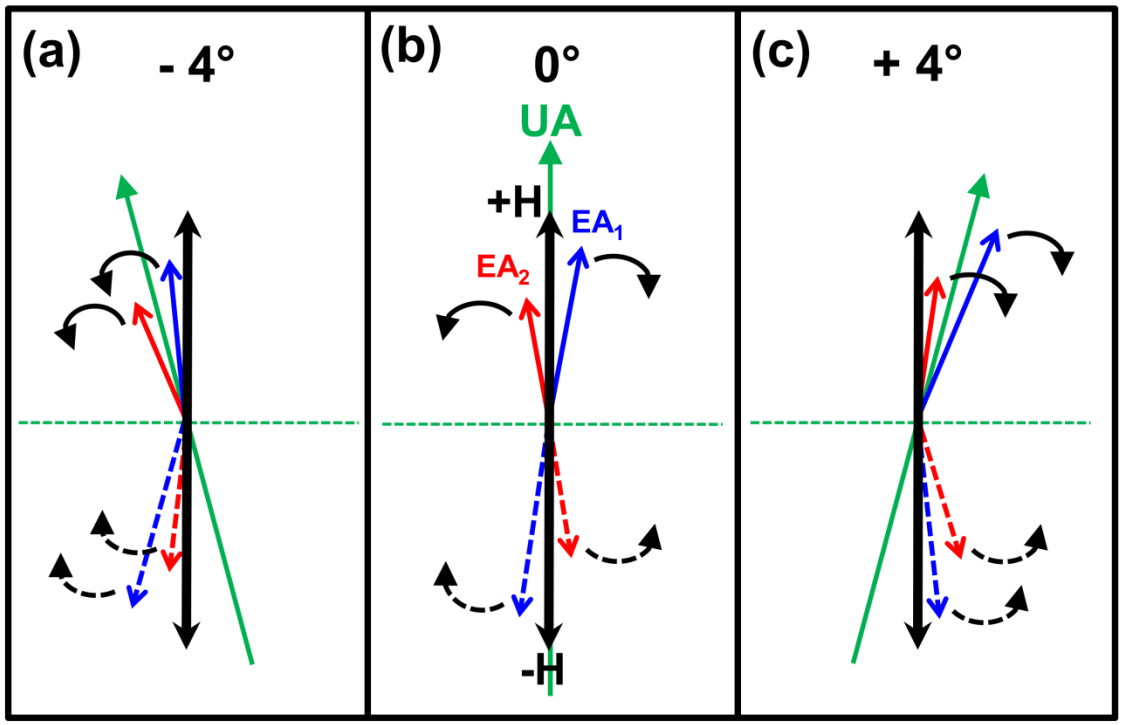

Figure 15. Schematic of the rotation directions for pinned moments. It is shown for two easy axis directions as indicated with the blue (EA_1) and the red (EA_2) arrows. These two directions are slightly tilted from the crystallographic easy axis (the green arrow (UA); unidirectional anisotropy axis). Magnetic field direction is fixed (along the black arrow). The dashed black arcs show the preferred rotation direction of the magnetic moments between two saturations. The small angle variations between the applied field and the crystallographic easy axis is shown for - 4° (a), 0° (b), and + 4° (c).

This intuitive picture can be used to explain all of the features that we see in the experimental data (Figure 14). (i) There should be no difference of the PHE signal between the upward and downward sweeps if the sample is tilted from the applied field

axis. This is due to half a circle rotation of the magnetic moments which is energetically favorable. (ii) Positive tilt angles (+ 4°) produce an opposite phase signal compared to the negative tilt angles (- 4°) because of the change in the direction of rotation. (iii) When the applied field is at zero degrees, the two networks simultaneously rotate in opposite directions and the measured signal intensity is much lower due to the sum of two opposite signals. In other words, the scattering from moments rotating in two opposite directions partially cancels and only the remaining signal is measured. (iv) When the applied field is at 0°, there is a phase difference between the upward and downward sweeps since the majority of magnetic moments rotate in a full circle between the two saturations, but in opposing directions.

It is worth noting that there is no need to introduce two different easy axes of the pinned magnetic moments to explain the behavior for nonzero angles (± 4°). However, the zero degrees behavior cannot be explained without assuming the presence of the two easy axes. To check this assumption, we simulated the PHE curves (Figure 16) with using the same model and parameters as in the section 2.3.

We included the two easy axis directions for the FM moments which are tilted ±4° from the unidirectional anisotropy axis direction (this is also our reference direction at zero degrees). The simulated curves for ±4° were obtained by changing the applied magnetic field directions to ±5°. The contribution from the pinned moment network in each tilted direction was assumed to be 50 %. The simulation represents all main features and shows excellent agreement with the data for ±4°. Simulation for zero

degrees successfully reproduces the decrease of the signal intensity. However, it shows curves with slight differences between upward and downward sweeps.

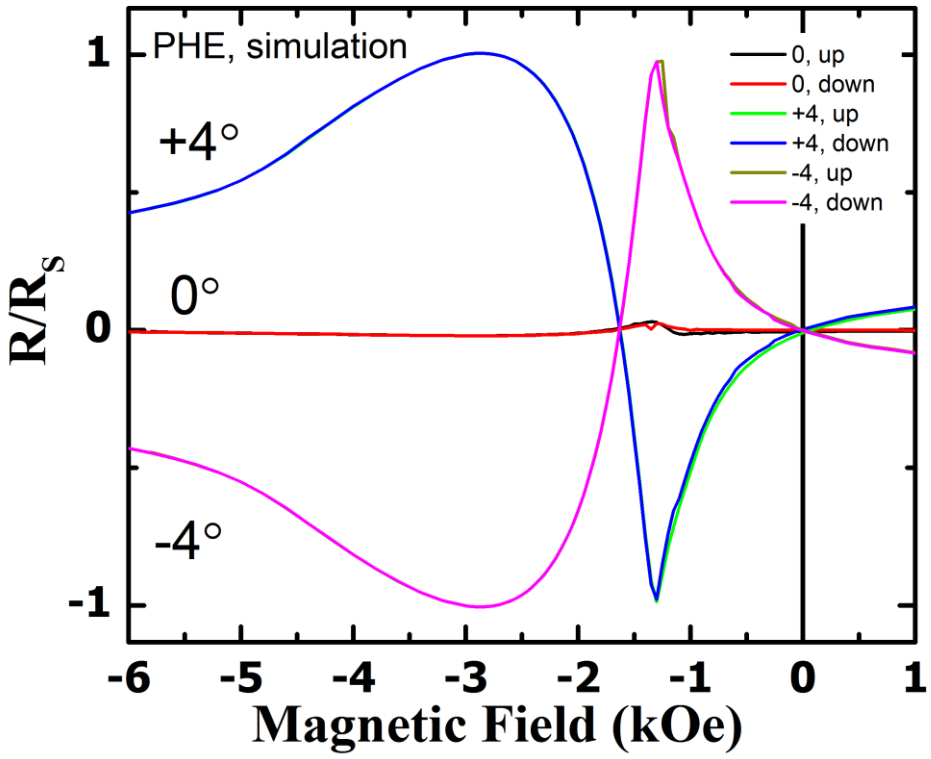

Figure 16. Simulation of PHE measurements for the small angle variations (±4°) around the easy axis (0°). The resistance values are normalized to the maximum resistance value. Both upward and downward sweeps are included for each angle. The PHE curves for ±4° clearly show the differences in rotation directions. The simulation is in a good agreement with the data (Figure 14(b)), including the significant decrease in the resistance amplitude for 0°.

In order to catch irreversibility, we changed the initial angular directions (β_1 and β_2) and the contribution ratio of each pinned moments (fraction) as seen in Figure 17. Here β_1 and β_2 represent the angles between the unidirectional anisotropy axis and the

two different easy axis directions of the pinned moments. The fraction is the contribution of the negative tilted moments to the PHE signal. If the contribution from one of the direction is increased (as in Figure 17(d)), we always obtained a reversible behavior (both upward and downward branches are the same). In this case, for example, both branches are similar to the up branch in Figure 13. The irreversibility appears when β_1 and β_2 are very similar but with opposite sign (as in Figure 17(a), (b), and (c)). Further varying the fraction (the relative contribution of each pinned moment direction) only appears to be a change in the average rotation direction of the moments (PHE sign).

We can conclude that the simulations using the incomplete domain wall model successfully reproduce the experimental data, except a very fine details at exact zero degrees. The assumption of the presence of an easy axis distribution for the pinned magnetic moments, which are slightly tilted from the average unidirectional anisotropy axis, is required to obtain the significant decrease in the signal intensity. Furthermore, the irreversibility at zero degrees can only be explained with this assumption. These measurements and simulations revealed that the magnetization rotation direction and the distribution of the easy axis can be probed by PHE technique. These details are not present in AMR measurements.

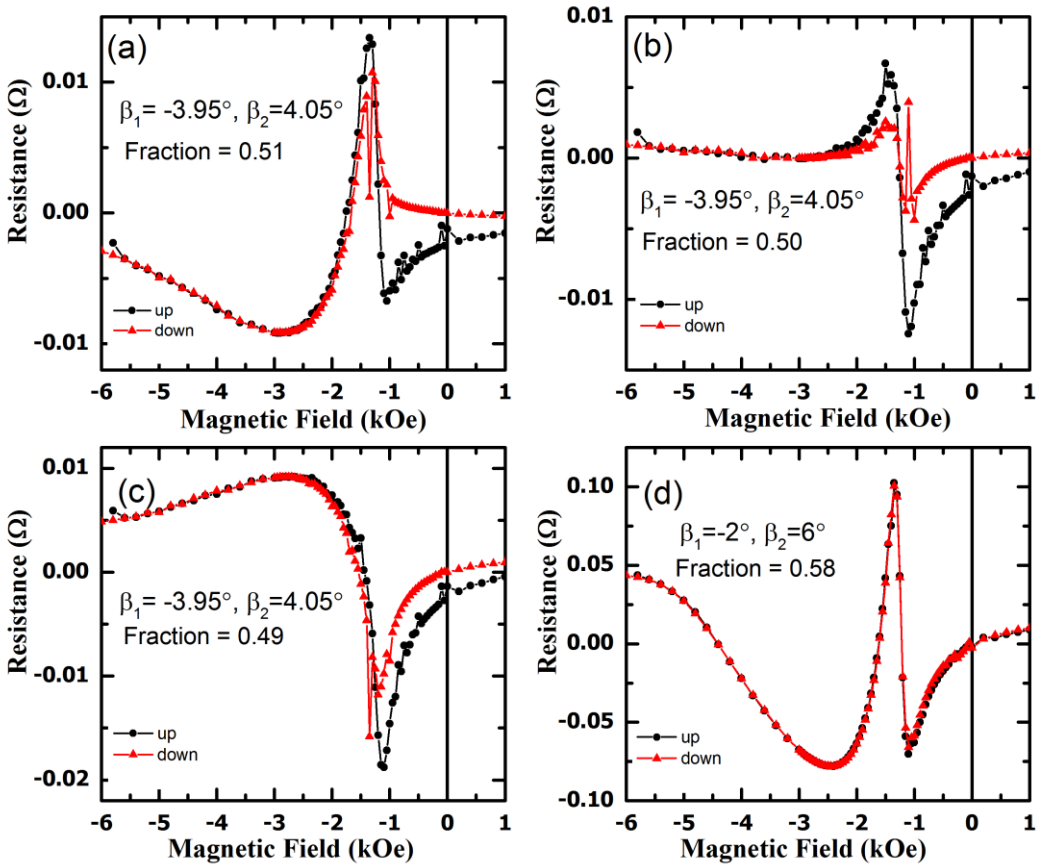

Figure 17. Simulations for PHE signals in the case of two slightly tilted magnetic moment directions. β_1 and β_2 represent the angles between the unidirectional anisotropy axis and the two different easy axis directions of the pinned moments. The fraction is the contribution of the negative tilted moments to the PHE. In each case, both upward (black) and downward (red) curves are included.

2.6. Dependence of magnetic field sweeps at higher angles

In the previous section, small angle deviations reveal the importance of the applied field angle with respect to the unidirectional anisotropy axis and the presence of more than one magnetic easy axis directions. We further investigated the change in the reversal mechanism at higher angles. Figure 18 shows the PHE measurements as a

function of magnetic field for some selected angles. Applying the field even two degrees away from the easy axis is enough to induce a preferred direction of rotation to magnetic moments. Further rotations away from the wire axis do not affect the preferred direction of rotation and both upward and downward branches follow the same curves. The amount of exchange bias field decreases following to the projection of the applied field along the unidirectional anisotropy axis and becomes zero at 90°. This is expected since it corresponds to perpendicular direction to the unidirectional anisotropy axis. The shape of the PHE curves at 45° is exactly the same as the AMR curves. If the sample is rotated in opposite direction (from 0 to - 90°), a symmetric behavior around the y-axis was observed (not shown).

Slight differences between upward and downward sweeps can be seen in the intensity of the PHE signals for up to ± 5° (Figure 14 and Figure 18). These slight differences disappear above ~ 5° in our samples so at high angles the two branches become identical (Figure 18). This implies that the angular distribution range of the direction of the pinned magnetic moments is approximately ± 5°. This leads to another important conclusion that the PHE signal can be used to probe the angular distributions of the pinned magnetic easy axes directions.

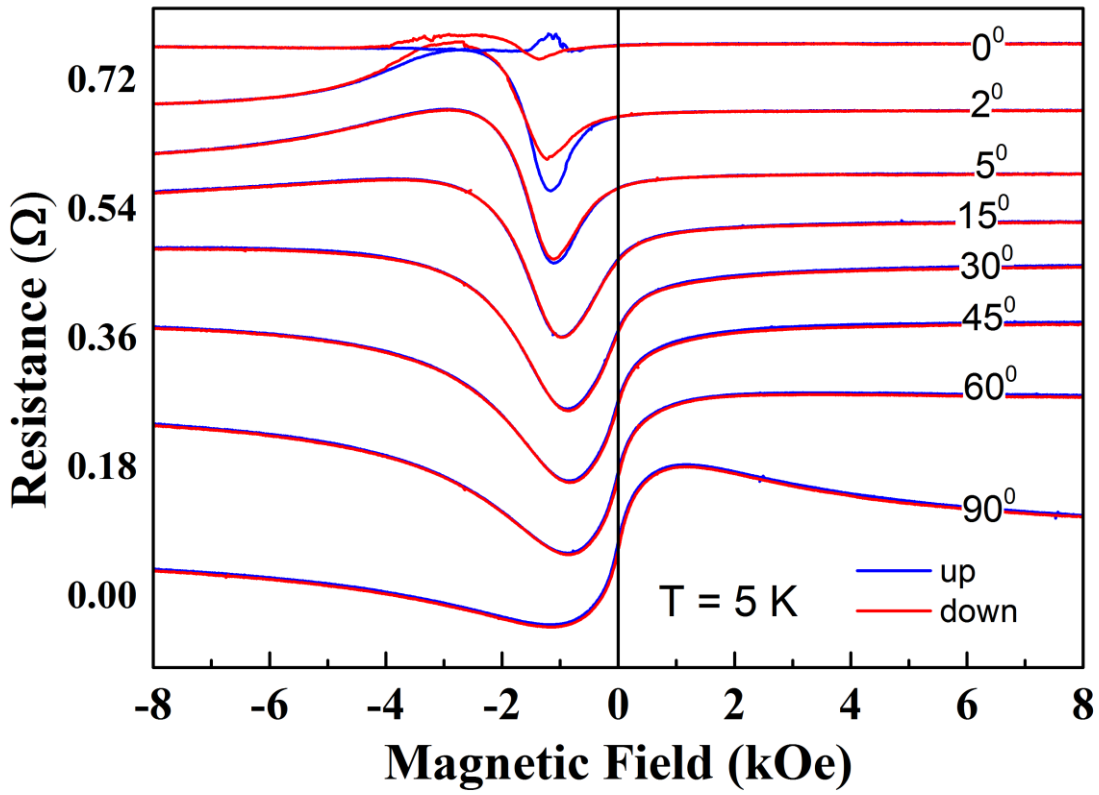

Figure 18. PHE measurements as a function of magnetic field for high angles. The curves are vertically shifted for clarity. These measurements were taken at 5 K after 50 Oe field cooling. Both upward (blue) and downward (red) sweeps are shown for each angle.

The magnetization reversal in a similar exchange bias system (Fe/MnF_2) has been studied by magneto-optical Kerr effect technique, which can also simultaneously probe both the longitudinal and the transverse components of the magnetization [87]. It was found that the transverse component of the magnetization changes its sign within a few degrees (±3°) around the unidirectional anisotropy axis. This measurement further supports our experimental results and interpretations. The transport measurements, unlike to magneto-optical Kerr effect, can be done in nanoscale devices - with the price

of a device fabrication and can be used to map the whole magnetization reversal process.

2.7. Rotational dependence: competing anisotropies

The magnetization reversal mechanism of the cross junction was further investigated using rotational measurements (Figure 19). These measurements differ from the field sweeps. In this method, instead of sweeping the magnetic field between the two saturations, the sample was rotated in a fixed applied magnetic field. The magnetic moments do not completely switch, but they rotate around the easy axis and allow mapping the angular and magnetic field dependence of the exchange bias anisotropy.

In order to perform an accurate angular study, the sample was rotated towards an index point in the CCW direction. This index point was used to calibrate the goniometer prior to measurements and it is located at negative ten degrees of the goniometer. This calibration was repeated after every complete cycle. A complete cycle of the measurement was from 0° to 360° in the CW direction and then back from 360° to 0° in the CCW direction. The easy axis of the sample, which is also the wire axis, was found to be at 107° on the goniometer. The magnetic field was applied along this angle during the cooling, establishing a strong unidirectional anisotropy axis.

In Figure 19, PHE and AMR measurements are compared at selected applied fields. The change in the resistance values during a rotation around a fixed magnetic

field shows that the direction of the magnetization varies. The magnitude of this variation is determined by the competition between the applied field and the effective magnetic anisotropy in the sample, which is dominated by the exchange bias anisotropy. The jumps in the resistance values and the hysteretic angular behavior around 284° (± 5°) imply a sudden change in the corresponding magnetization when the projection of the magnetic field overcomes the exchange bias field. The rotational dependence for different applied fields can be analyzed in three cases.

(i) For a high enough applied field (in this case > ± 5 kOe), the magnetization always remains in the applied field direction during rotation (not shown). Therefore, the change of the angle between the magnetization and current produces a PHE signal similar to Figure 12 (d).

(ii) For a small applied field (< ± 0.3 kOe), the magnetization direction is not significantly affected by the applied field. Instead, it remained along its own axis because of the effective anisotropies and only negligible changes in the resistance were recorded (not shown).

(iii) When the applied field is in the range of the exchange bias field, the direction of the magnetization is determined by the competition between the effective anisotropy and the applied field (Figure 19).

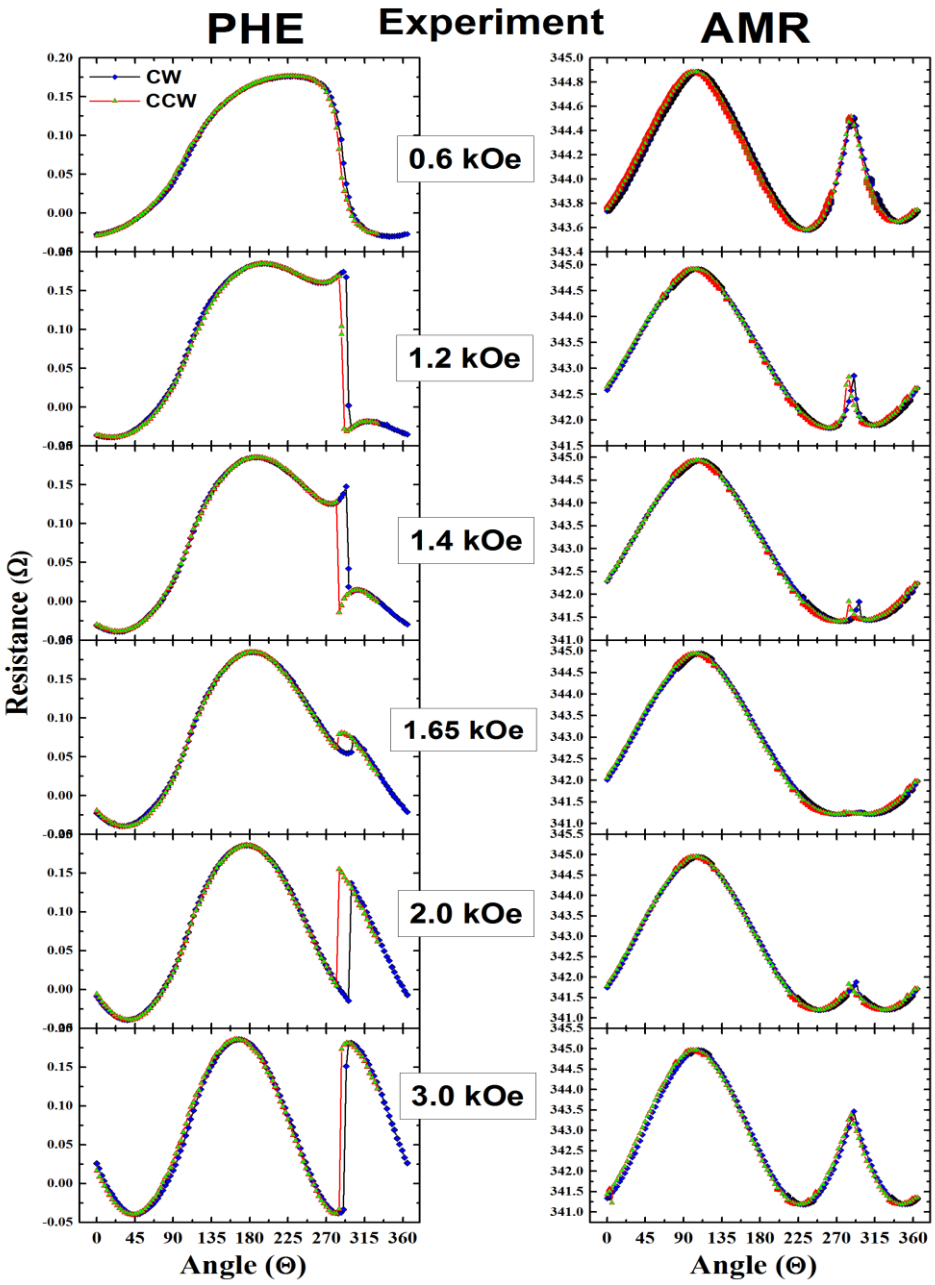

Figure 19. Rotational dependence of PHE (left) and AMR (right) signals for some selected applied fields and for both CW (blue symbols) and CCW (green symbols) directions.

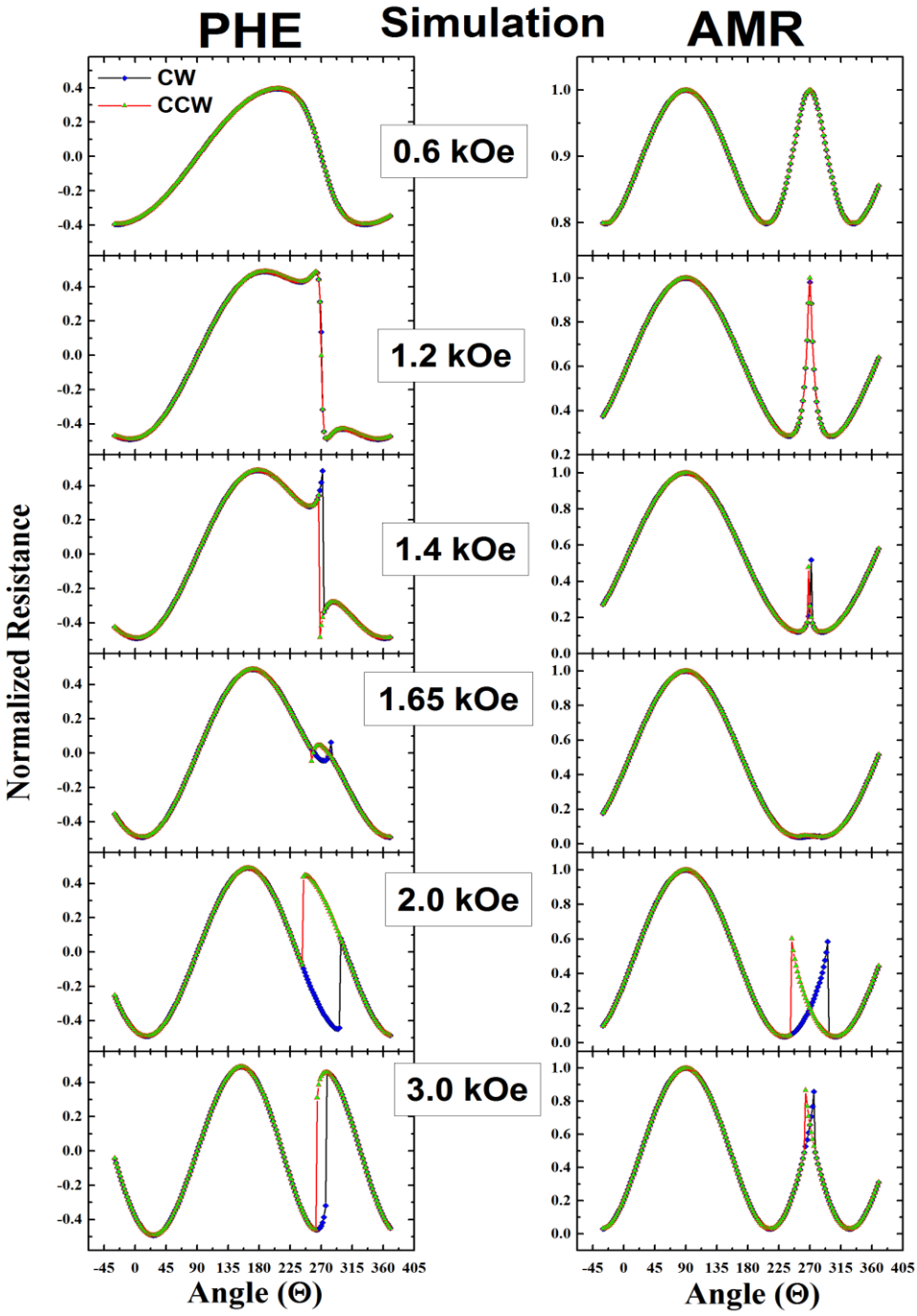

Figure 20. Simulated rotational dependence of PHE (left) and AMR (right) signals for some selected applied fields and for both CW (blue symbols) and CCW (green symbols) directions

In order to understand the reason for the abrupt changes in the resistance values, rotational effects on the magnetization were simulated using the same model. In these simulations, we used the same parameters that were presented in section 2.3. To account for the experimental uncertainties in the goniometer, we ran the simulations from - 30 to 370 degrees. The resistance values were normalized, so that the PHE and AMR values varied between ± 0.5 and 0 to + 1, respectively. The simulation results are in excellent agreement with the experimental data as seen in Figure 20. 17° shift in the angle values in the experimental data agrees with the shift found from the calibration of the goniometer.

The simulations show all major experimental features such as abrupt jumps around 270° and a coercive behavior between CW and CCW sweeps. The hysteretic behavior seems slightly narrower for 1.2 kOe and 1.4 kOe and wider for 2 kOe applied fields in the simulations. This can be related to the contribution of the shape anisotropy in the actual sample.

In addition to the PHE and AMR signals, the simulations provide the longitudinal and transverse components of the magnetization. Therefore, we can calculate the angle (Φ) between the average magnetization and the unidirectional anisotropy axis during the rotations. Please notice that we are using an average magnetization and Φ to refer its angular position relative to the unidirectional anisotropy axis. There is no need to assume more than one pinned magnetization direction to simulate the rotational dependencies since the angular distribution is averaging out. Figure 21 shows all individual components during the CW rotation for a

1.4 kOe applied field. As the sample rotated within the applied field, the AMR signal (Figure 21 (b)) is governed by the longitudinal component of the magnetization while the PHE signal (Figure 21 (c)) is dominated by the transverse component of the magnetization.

Here, Θ is the angle between the applied magnetic field and the current direction (the current is restricted to flow through the unidirectional anisotropy axis, i.e., current axis). We define Φ as the angle between the average magnetization and the unidirectional anisotropy axis. Since the position of the average magnetization relative to the current axis can be either forward or backward, the values for Φ can be positive or negative. The positive values correspond to the magnetization vector away from the current axis in the CCW direction, while the negative values correspond to those in the CW direction. The change of Φ from positive to negative at 270° explains the sign change in the PHE signal from positive to negative. Similarly, AMR response appears as a narrow peak at the same angle. Therefore, the abrupt change in the PHE and AMR signals is due to the change in the magnetization direction with respect to the current axis. This is illustrated in Figure 22.

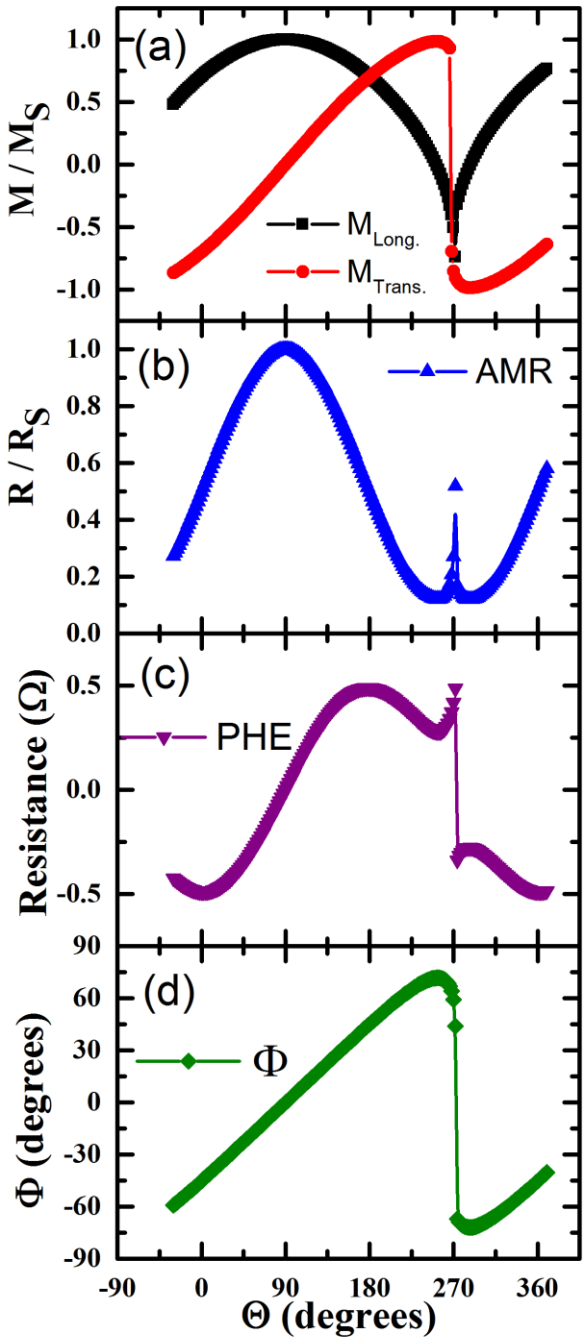

Figure 21. Simulation results for the rotation in CW direction in a 1.4 kOe applied field. The transverse (red circles) and longitudinal (black squares) components of the magnetization (a), AMR (blue triangles, (b)) and PHE (purple inverse triangles, (c)) signals, and angular variation of Φ (green diamonds(d)) are shown as a function of Θ.

A schematic representation for the change of the angle between the current axis and the average magnetization is depicted in Figure 22. This sketch shows only the position of the magnetization and the wire axis near the jumps in the rotational curves for 1.4 kOe applied field. When the sample reached $\Theta = 270°$ (Figure 22 (a)), the vector sum of the applied field and the exchange bias field forced the magnetization to abruptly rotate around the current axis (Figure 22 (b)). Since the relative orientation between the magnetization and the current axis changes, the PHE signal shows an abrupt jump in value, from positive to negative (Figure 21 (c)). For CCW rotations, the same mechanism happens and causes a jump from negative to positive instead. However, this time the jump happens at different angle, since the vector sum requires that the current axis pass around 270° in the other direction (Figure 22(d)). Therefore, there is a hysteretic behavior between CW and CCW rotations.

The angle at which the jump happens depends on the strength of the applied field, because it is the applied field which horizontally forces the magnetization, causing it to switch. The vector sum of the applied field and anisotropy fields determines the angle. For a 1.4 kOe applied field, the average magnetization does not switch from one direction to the other, since the field is not strong enough. Instead, the magnetization changes its direction with respect to the current axis in a manner determined by the competition between the applied field and anisotropy fields.

One apparent different between the sample rotation and the magnetic field sweeping is that the former does not probe a whole magnetization reversal. Instead, the average magnetization slightly deviates around the current axis and causes changes in

the PHE and AMR signals. For higher applied fields, the magnetization is forced to follow the external field and we see a 4-fold symmetric angular behavior. These measurements probe the average magnetization (spin configuration of the FM layer) and confirm the coherent rotations of magnetic moments. The validity of the incomplete domain wall model in our samples is also confirmed by this data.

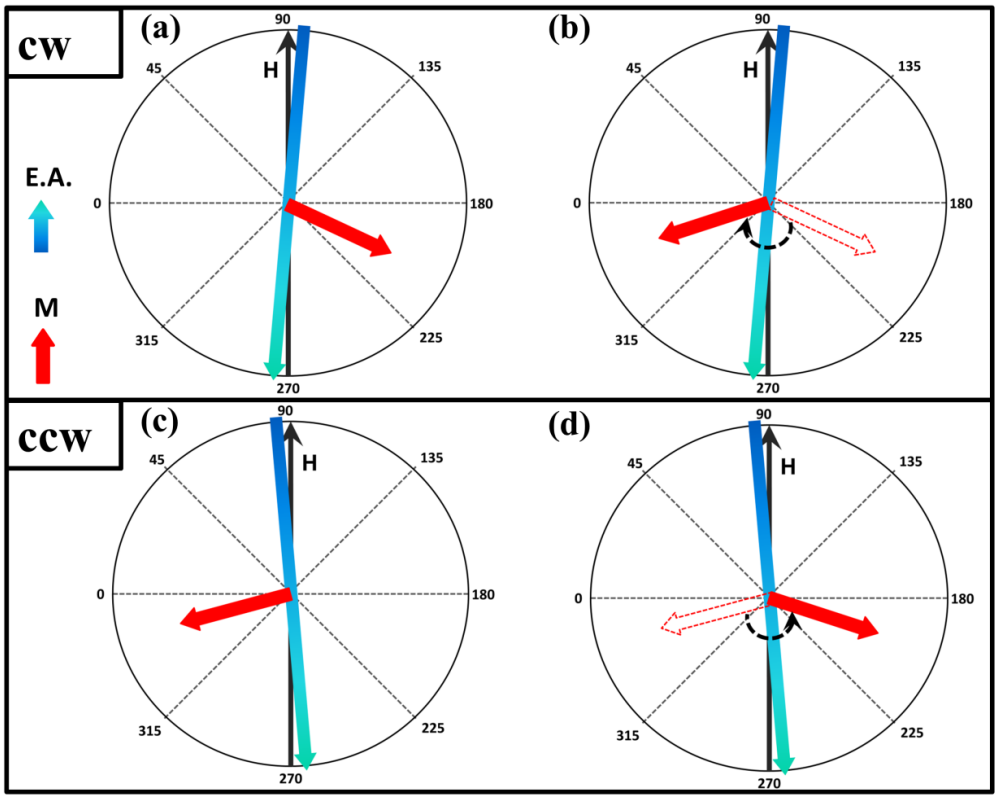

Figure 22. Illustration for the magnetization and switching directions around Θ = 270° for both CW (top) and CCW (bottom) directions at 1.4 kOe applied field. The direction of the applied magnetic field and angles represent the experimental situation. The current goes through the wire axis (blue arrow). The magnetization (red arrow) switches from (a) to (b) as the sample is rotated in CW direction, while (c) to (d) in CCW direction.

2.8. Conclusion

The magnetization reversal mechanism in lithographically patterned exchange bias Ni/FeF_2 cross junctions was studied by two magnetoresistance measurement techniques. We unambiguously showed that PHE measurements can be used to distinguish the rotation direction of the magnetization. On the other hand AMR is not able to do this. The sensitivity and the ability to distinguish relative magnetization orientations of the PHE measurements imply a distribution of unidirectional anisotropy axes around the crystallographic easy axis. These unidirectional anisotropy axes correspond to a distribution of pinned magnetic moment directions around the crystallographic easy axis and determine the direction of the magnetization rotation. The rotational dependence of the magnetization of Ni/FeF_2 crosses was studied by CW and CCW rotations. A competition between the established unidirectional anisotropy and the applied field determines the magnetization direction with respect to the current axis. Changes in the magnetization direction around the current axis produce abrupt changes in the PHE signal. An angular hysteretic behavior was observed when the applied field in the range of the exchange bias field. All of the experimental features were explained using a simulation, based on incomplete domain walls that are formed in the FM layer due to exchange bias.

2.9. Acknowledgements

Chapter 2, in part, is currently being prepared for publication. Co-authors include Rafael Morales, Stefan Guenon, and Ivan K. Schuller. The dissertation author was the primary investigator and author of this material. Ali C. Basaran worked on the sample design, performed the fabrication, measurement, and analysis for this work, and will be the primary author on the paper.

3. Role of the antiferromagnetic bulk

Exchange bias is mainly governed by the FM/AFM interface. However, the interfacial properties between two dissimilar magnetic materials is not free from the bulk related properties and can be affected by the magnetic configurations throughout the bulk. In this chapter, we investigate the AFM bulk and its effect on exchange bias.

3.1. Introduction

As of today, the details of the mechanism leading to exchange bias are not fully established and contradicting experimental and theoretical studies are reported. One of the controversies is whether the AFM bulk needs to be considered in the establishment and magnitude of the exchange bias [8, 11]. Extensive and sometimes contradicting models consider the interface and AFM bulk with different importance [8, 15, 48, 61, 92-94]. For example, models that are based on AFM domain walls either perpendicular [95] or parallel [48] to the interface are in direct contrast to the domain state model [96, 97], which considers the entire bulk of the antiferromagnet. A generally accepted picture is that the unidirectional anisotropy is due to uncompensated AFM spins, whose density governs the bias [4, 98].

Dependence of exchange bias on AFM bulk properties has been experimentally investigated in experiments using FM/AFM/FM trilayers [11, 99] or diluted AFM materials [12, 97]. However, inserting magnetic or non-magnetic impurity layers at different locations away from the interface reveals that the effect can extend only up to few nm into the bulk [100]. Furthermore, neutron scattering experiments indicate the magnitude of exchange bias is not influenced by the AFM domain size [101], contrary to several other observations in which the AFM domain size is important [19, 20]. Experiments using either polarized x-ray [46, 102] or neutron scattering [46, 47] observe a finite magnetization in the AFM bulk, but the effect on exchange bias remains elusive. Although these reports display contributions of the magnetic structure beyond the interface, the importance of AFM bulk is still far from being uniquely established and accepted [9].

Many of the experimental disagreements arise because exchange bias depends simultaneously on several extrinsic and intrinsic parameters of the materials and measurement conditions. It has been shown that sample specific morphologies, such as roughness [17, 18], grain size [19-21], crystallinity [22, 23], interlayer diffusion [24], and defects [25, 26] are crucial for the effect. The magnitude and sign of the exchange bias further can be altered by different magnetic field history and cooling procedures [27, 28]. In consequence, establishing a unifying theory taking into account all of the above parameters might be very difficult. Similarly, a clarifying experiment is required to simultaneously detect and separate contributions from interface and bulk, which is in

general not established. For example, studies as a function of the AFM layer thickness [103, 104] or dilution of the antiferromagnet [12] do not relate bulk and interface.

In this chapter we will present an experiment designed to detect simultaneously and separate the contributions from all layers involved in exchange bias. Beyond the existing investigations of the AFM bulk contribution, we employ post growth modification of the antiferromagnet at controlled depth in fixed magnetic conditions. In contrast to previous studies we present an approach which is not influenced by intrinsic sample morphologies because the sample, and therefore all structural parameters, and the measurement protocol are the exact same. Therefore we avoid comparisons of different roughness, grain size, crystallinity, interlayer diffusion, and defects, except of those intentionally introduced at pre-determined location within a single sample. Furthermore, we avoid altering the magnitude and sign of exchange bias by different magnetic field history and cooling procedures. Our observations demonstrate the bulk of the antiferromagnet is a crucial ingredient for establishing exchange bias.

More specifically, we investigate the contribution of AFM bulk by controlled defect creation using light-ion bombardment [105]. The impinging ions create defects whose location depends on the energy [106]. In order to investigate defects preferentially created in the antiferromagnet, the FM layer is located below the AFM layer and the bombardment is done from top. The penetration depth of ions, and therefore the depth at which defect formation takes place, is controlled by varying Au capping layer thicknesses.[107]. Direct comparison of the exchange bias before and

after the bombardment as a function of Au thickness enables a separation of the magnetic contribution of interfacial and bulk defects.

3.2. Sample fabrication

In order to create defects selectively at different part of the exchange bias bilayer system, the depth of bombardment ions needs to be controlled. This can be appropriately done either by changing the energy of bombardment ions or by keeping all bombardment parameters (such as energy and dose) are the same and varying thickness of capping layer to stop ions at different depths. The later one was chosen to avoid possible bombardment related effects and avoid systematic errors. All samples were bombarded at the same time under the same conditions and the only parameter which affects the ion penetration depth is the capping layer (Au) thickness on different samples. Therefore, the stopping range of the ions is solely determined by the Au layer thickness (t_{Au}).

Several sets of Ni (10 nm)/FeF_2 (70 nm) bilayers with constant thickness were grown simultaneously by electron-beam evaporation on (0001) Al_2O_3 substrates. Substrates were cleaned with acetone and methanol in ultrasonic cleaner for 15 minutes each before loading into the chamber. Substrates were heated to 500 °C for 1 hour prior to deposition, and then cooled to Ni growth temperature (~150 °C). The temperature was again increased (10 °C/min.) and kept at ~300 °C during FeF_2 deposition. The Au capping layer was deposited after the temperature reduced below 50 °C. By using a

shadow mask with translational movement, the samples were exposed to Au for different times, leading to a controlled variation of the Au thickness (Figure 23). The base pressure remained below 10^{-6} Torr during the deposition of all layers. The Ni thickness of 10 nm was chosen after studying a range of FM thicknesses (within 5 to 35 nm of Ni in more than 50 samples) in order to obtain a fully biased hysteresis loop. The thickness of FeF_2 was chosen to 70 nm, which is thicker than the typical AFM domain size of FeF_2 (~30 nm [101]).

All samples were investigated using SQUID and VSM magnetometers, as well as x-ray diffraction and reflectometry in order to determine the structure.

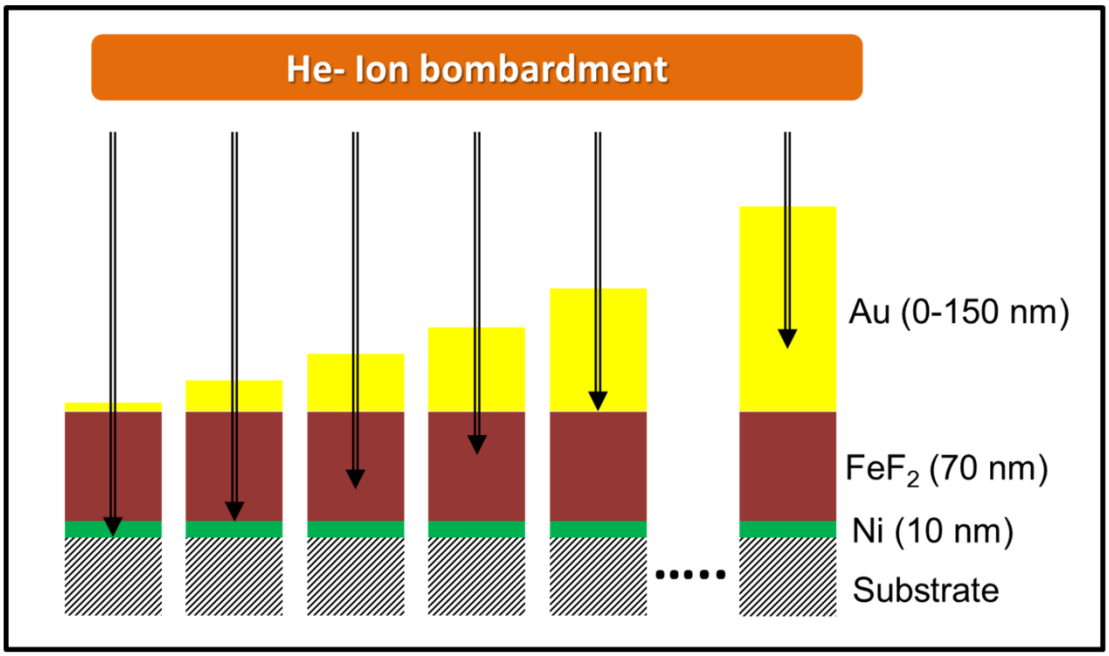

Figure 23. Schematic of the experimental approach: in-situ sample growth of varying capping layer thickness and following He-ion bombardment. He-ions penetrate and create defects at different depths as the capping layer thickness changes.

3.3. Ion bombardment and simulations

Following the initial structural and magnetic investigation, all samples were bombarded with He ions using a fixed 9 kV acceleration voltage in a home built setup [108] at a current of 300 nA. The acceleration voltage was chosen based on SRIM (Stopping and Range of Ions in Matter) [109] simulations to obtain an ion penetration into the FM layer for thin Au (Figure 24).

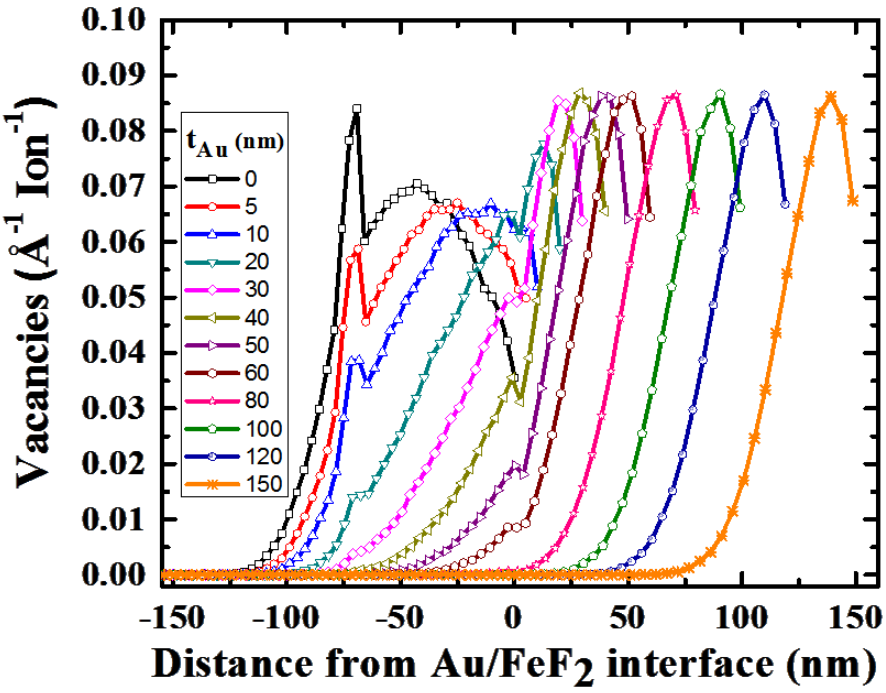

Figure 24. SRIM simulation of vacancy creation per Ion and Å as a function of Au thickness for 9kV acceleration voltage and 1.0×10^{15} ions/cm^2 dose.

The ion bombardment was carried out at a base pressure of 2.5×10^{-6} Torr at room temperature, i.e. well above the Néel temperature of FeF_2 (T_N = 79 K). A constant ion dose across the sample was achieved by defocussing of the beam by an electrostatic Einzel-lens and feeding it through an aperture. This leads to a beam spot of 2.5×2.5 mm², which was scanned over the samples in lines. The centers of adjacent lines were displaced by 250 μm. The exposure time of the samples to the ion beam was controlled for each line to achieve the desired dose.

We have designed two different experiments. First, we used a fixed low ion dose ($1.0x10^{15}$ ions/cm^2) to determine the effect of defects on exchange bias and to avoid structural changes. This allows us to compare differences in magnetic properties of varying Au capping layer thickness. Second, we chose three critical thicknesses (20, 40 and 60 nm) and varied the ion dose (varied the number of defects). Hence, we investigate the individual contributions from different regions; the FM layer, the FM/AFM interface, and the AFM layer.

3.4. Structural analysis

An exhaustive structural analysis of x-ray diffraction and reflectivity of all samples before and after the bombardment has been performed. The high angle diffraction reveals highly textured FeF_2 with (110) aligned with the direction normal to the surface and indicates a predominant orientation of the FeF_2 along the (110) (Figure 25). However, other diffraction lines can also be observed with less intensity. Only FeF_2

diffraction lines are marked in Figure 25. For all Au thicknesses, both (111) and (200) reflections were observed, indicating a polycrystalline growth of Au. Diffraction of 10 nm Ni is not observed due to overlapping Au and substrate reflections. No change in crystalline orientation or diffraction profile of any material within the stack was observed after the bombardment.

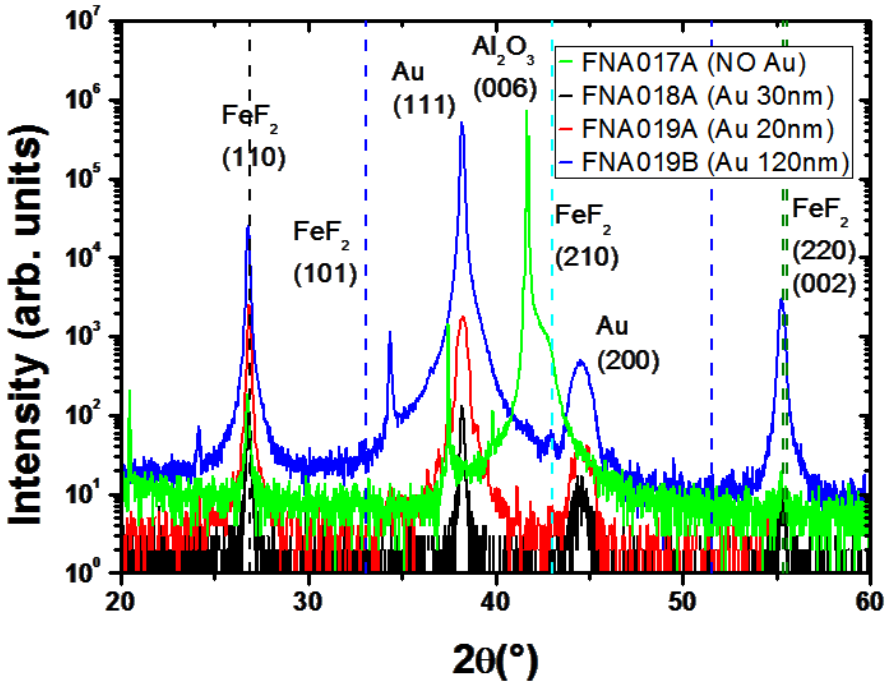

Figure 25. High angle x-ray diffraction data for four different samples with 0, 30, 20, and 120 nm Au thicknesses. FeF_2 diffraction lines are marked in the graph.

Figure 26 shows x-ray reflectivity measurement and fit of the sample with 10 nm Au capping before the bombardment. The fitting was performed using MOTOFIT [110], designed to fit slab models to a range of datasets with the same initial parameter set. Layer thicknesses (t) and interface roughness (σ) obtained from the fitting are 8.4 nm and 0.4 nm for Ni, 66 nm and 1.1 nm for FeF_2, 10.9 nm and 1.5 nm for Au,

respectively. The FM/AFM interface establishing H_{EB} has the lowest roughness of the structure, since the Ni layer is grown directly on the substrate.

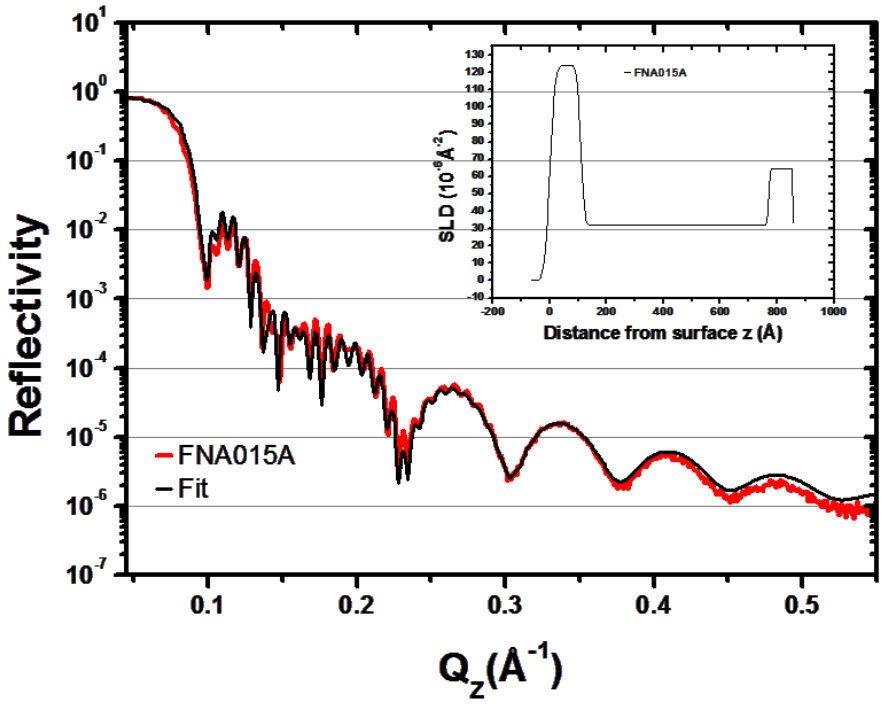

Figure 26. Example XRR measurement for t_{Au}= 10 nm before the bombardment (red) and fit (black). Inset: corresponding scattering length density (SLD) profile.

Similar structural analysis has been performed for all samples after the bombardment. Figure 27 shows XRR measurement and fit of another sample with 50 nm Au capping before and after the bombardment. Layer thicknesses (t) and interface roughness (σ) obtained from the fitting are 8.6 nm and 0.4 nm for Ni and 66 nm and 1.2 nm for FeF_2. Typical differences in the reflectivity profiles of as grown and bombarded

samples are on the scale shown in the inset of Figure 27. The deviations are well accounted for by only minor adjustments of structural parameters by few Å.

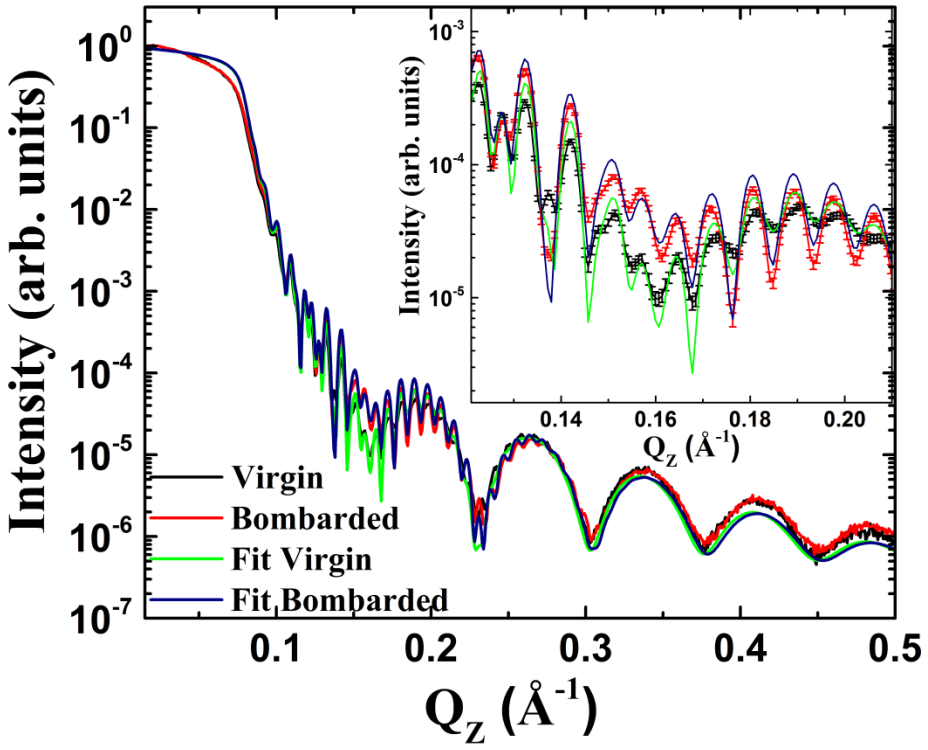

Figure 27. Example XRR measurement for t_{Au}= 50 nm before and after bombardment and fit (lines). Inset: Enlarged view of the differences in the reflectivities due to the bombardment.

Results from structural analysis as a function of Au thickness are shown in Figure 28 for more samples within the range of up to 150 nm Au. The Ni (FeF_2) layer thickness shows a ±0.2 nm (±4 nm) variation from sample to sample. The deviation from the nominal layer thicknesses amounts less than 10 % for all samples, except of the sample with 100 nm Au capping. This can be related to a large uncertainty in the fitting for this thickness combination only. XRR fitting results of the samples after

bombardment are included in Figure 28. We observe no evidence of structural changes in either interface roughness or sample structure due to the bombardment.

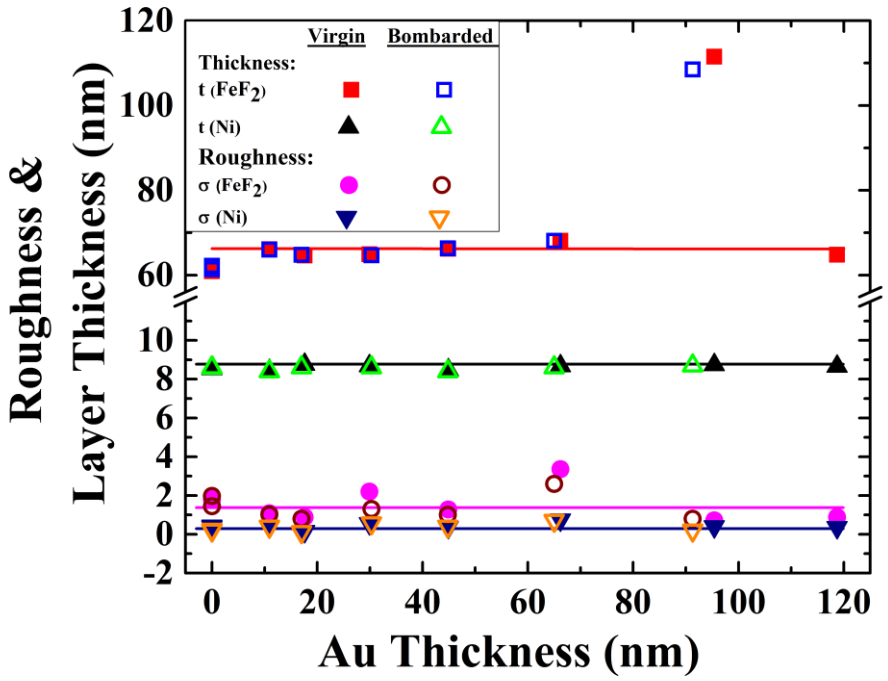

Figure 28. Layer thickness and roughness parameter obtained from XRR fits. FeF_2 and Ni parameters are plotted over the fitted Au thickness. Lines are guide to the eye.

3.5. Magnetic characterization

For the magnetic characterizations the following experimental protocol was fixed for all samples for consistency. A +200 mT magnetic field was applied parallel to the film plane at 200 K, above the Néel temperature of FeF_2. This establishes fully

reproducible magnetic initial conditions. The field was decreased to +20 mT, which was determined strong enough to keep the Ni saturated during cooling to measurement temperature. On the other hand, the cooling field was chosen low enough in order not to induce positive exchange bias, which arises at higher cooling fields [27, 111]. Hysteresis loops were recorded scanning the magnetic field starting from positive to negative saturation direction. The data has been corrected for a linear diamagnetic slope from the substrate. Exchange bias is determined for each sample individually by the offset of the loop center along the applied field axis.

Figure 29 shows two different samples with 0 and 60 nm of Au capping layers. In both curves, the measurements before and after the bombardment were included. The left curves belongs 7 by 10 mm sample size and were obtained from SQUID magnetometry at 10 K, whereas the right curves belongs to 3 by 4 mm sample size and were obtained from VSM measurements at 20 K. Both samples were bombarded at the same time with the same parameters (9 kV, 1.0×10^{15} ions/cm^2). In both cases, exchange bias was decreased by about 18 %. This indicates that the change in the exchange bias is about the same no matter if the ions create damages at the interface or not.

The magnetization value for SQUID sample is higher since the measured sample size is bigger. It is worth to mention that the exchange bias values show no significant changes below 40 K (see Figure 36); therefore comparison of H_{EB} between 10 K and 20 K is reasonable and excludes thermal effects. We do not observe a training effect for any of the samples measured with above described protocol.

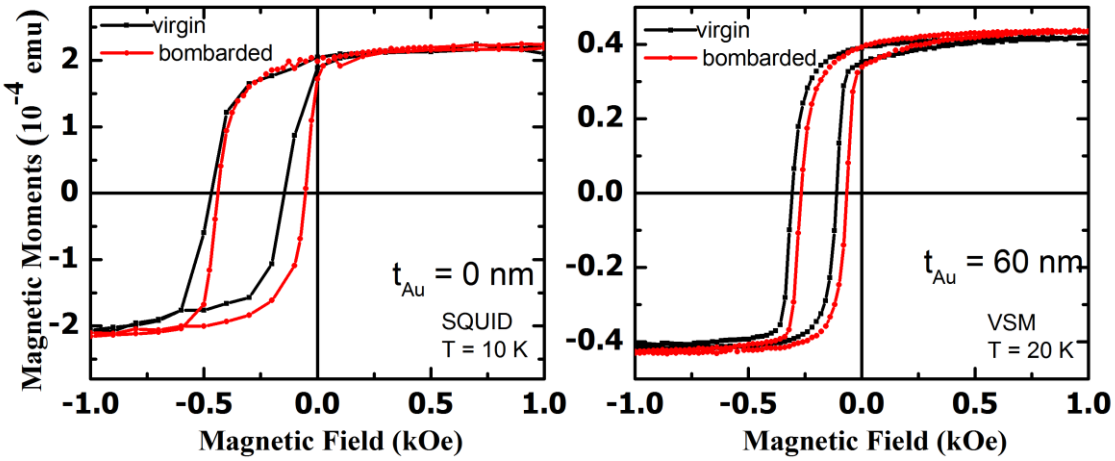

Figure 29. Comparison of hysteresis loops before and after the ion bombardment for 0 and 60 nm of Au samples, measured in two different systems (SQUID and VSM).

Figure 30 shows examples of magnetic hysteresis loops at 10 K of the sample with 30 nm Au capping layer before and after the ion bombardment. The curves are normalized to the maximum saturation value. A shift of $H_{EB}^{v} = 66.5$ mT was recorded before the bombardment, which decreased to $H_{EB}^{b} = 40.9$ mT after the bombardment. This corresponds to a decrease of $\Delta H_{EB} / H_{EB}^{v} = (H_{EB}^{v} - H_{EB}^{b}) / H_{EB}^{v} = 38$ % for this sample. H_{EB}^{v} and H_{EB}^{b} H_{EB}^{b} refer to exchange bias fields for the virgin and bombarded sample, respectively.

Magnetization values for all samples are consistent within 2 % for the samples grown in the same deposition. Although samples were grown simultaneously, differences in the Ni volume (due to slight variation in the deposition rate at different positions on the holder) or different domain formation in the AFM layer can arise and explain the variation. The contribution of magnetic moments from free Fe or some other

possible intrinsic contributions from AFM layer can also differ from sample to sample. To exclude these kinds of inevitable variations between samples, we compare only identical sample before and after the bombardment and normalize the change in H_{EB} due to bombardment to the value before the bombardment.

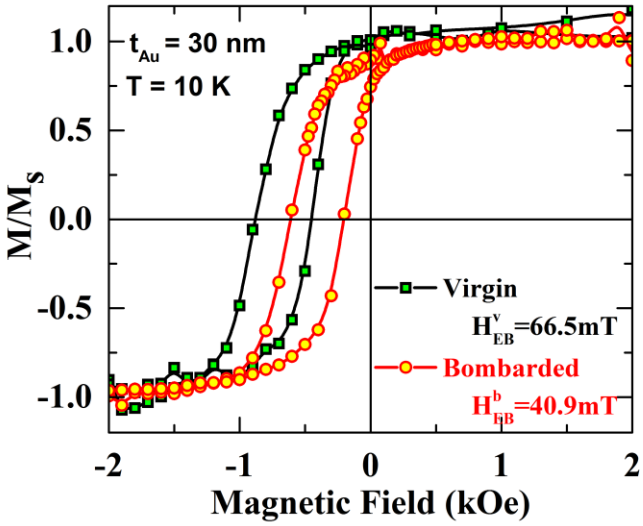

Figure 30. Example of a SQUID measurements for as-grown (black squares) and bombarded (red circles) sample with t_{Au} = 30 nm. Both curves are obtained at 10 K after 20 mT field cooling from 200 K. The He-ion bombardment decreases the loop shift by ~38 %. The magnetization values are normalized to saturation.

3.6. Au thickness (depth) dependence

The relative change $\Delta H_{EB} / H^{v}_{EB}$ as a function of Au thickness is summarized in Figure 31. This plot includes 18 samples deposited in 3 different sets. Each set comprises thick and thin Au layers. Two sets were measured with VSM (black squares and red circles) at 20 K and one set was measured in a SQUID magnetometer (blue

triangles) at 10 K. Experimental errors of ~10 % were estimated based on sample mounting and diamagnetic background corrections. The vertical lines mark the regions affected by ion bombardment extracted from Figure 24 (see also Figure 32). Without capping layer, the initial decrease of amounts to ~20 %. With increasing Au thickness, the change shows a peak of 35 % at t_{Au}= 20 – 30 nm. Beyond t_{Au} = 40 nm, a plateau at ~20 % is observed over 40 nm. Above t_{Au} = 80 nm the change gradually vanishes.

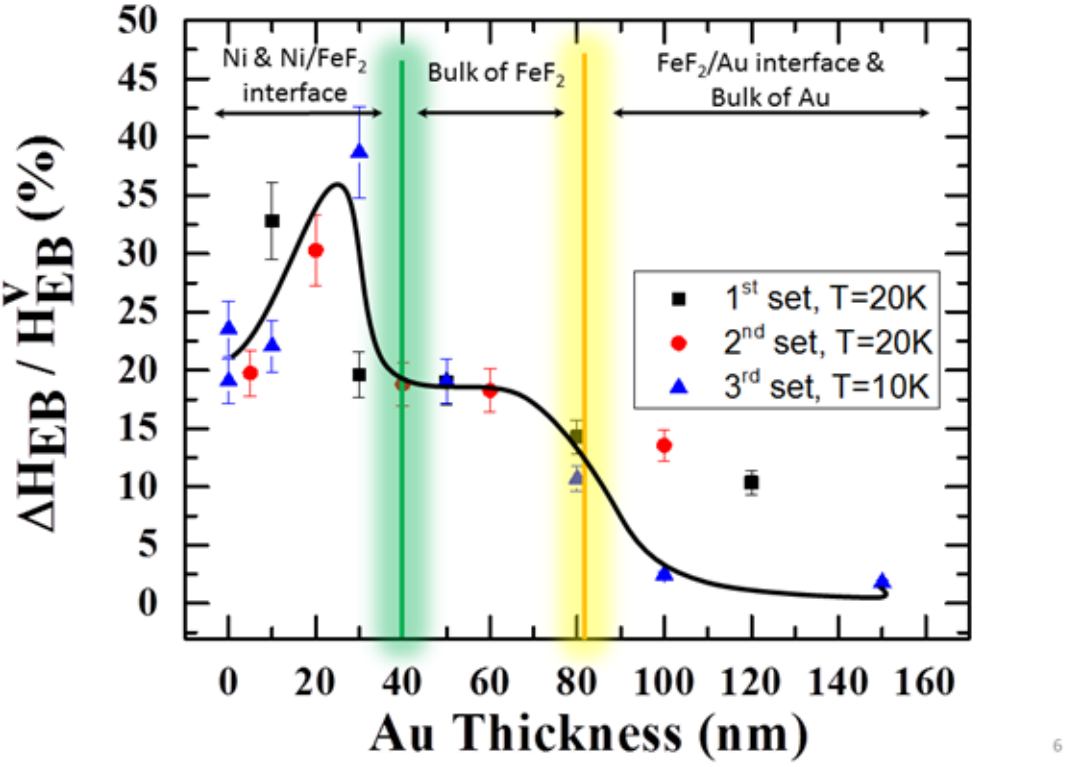

Figure 31. Relative change of exchange bias field as a function of the Au thickness for three sets of samples. Set one and two were measured with VSM at 20 K (black squares and red circles, respectively). The third set (blue triangles) was measured with SQUID magnetometer at 10 K. The line is a guide to the eye. Vertical lines obtained from Figure 24 indicate separation of affected regions due to bombardment.

In order to explain this data, the number of vacancies obtained from SRIM simulations (Figure 24) were separately integrated over the interface and FeF_2 thickness and plotted in Figure 32. There is no penetration into the AFM layer above 80 nm (± 10 nm) Au. The FM/AFM interface is only affected up to 40 nm (± 5 nm) Au. Therefore, the observation of a finite change in $\Delta H_{EB} / H_{EB}^{v}$ well above t_{Au} = 40 nm shows that the bulk of the AFM layer must have an influence on exchange bias.

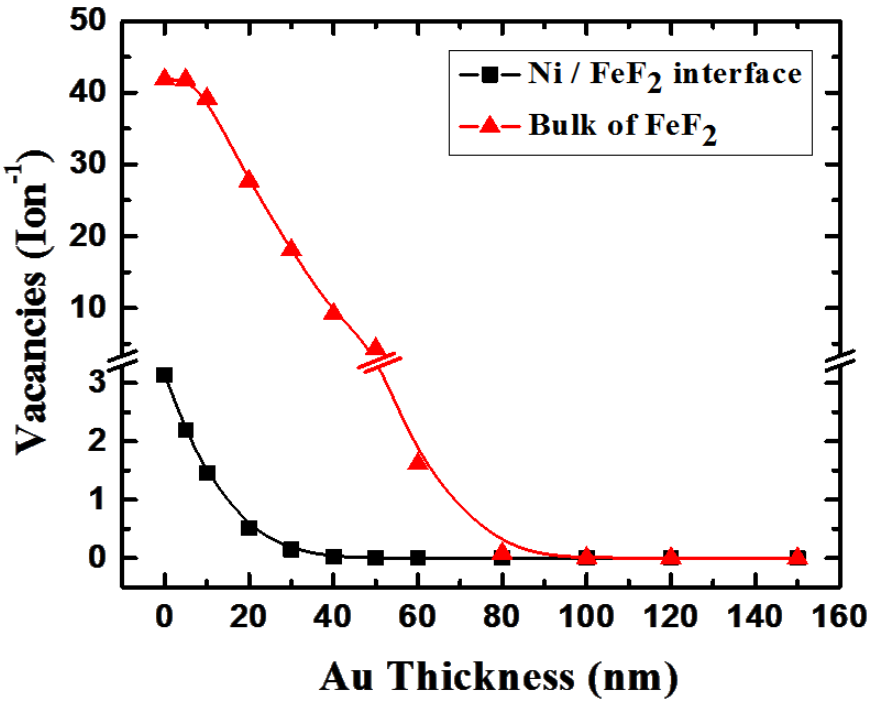

Figure 32. Number of vacancies from Figure 24 integrated over the interface (black squares) and FeF_2 thickness (red triangles). Above 80 nm (± 10 nm) Au no penetration of ions into AFM layer takes place. The FM/AFM interface is only affected up to 40 nm (± 5 nm) Au.

According to the SRIM simulations, no defects are created at or near the FM/AFM interface above this critical thickness (green line in Figure 31). Only the

defect creation in the bulk extends to t_{Au} = 80 nm, which agrees with the observed plateau of $\Delta H_{EB} / H_{EB}^{v}$. Above t_{Au} = 80 nm (yellow line in Figure 31), ions do not penetrate through the Au and therefore no defects are created in FeF_2 and the change in exchange bias vanishes as expected. The observation of the AFM bulk affecting H_{EB} is independent of the detailed mechanism leading to the change in H_{EB}.

3.7. Dose dependence

In order to investigate the dependence of number of defects at different depths, we employed He-ion bombardment with different doses. We kept the same energy (9kV) and only varied the bombardment dose for three chosen capping layer thicknesses (20, 40, and 60 nm of Au). According to SRIM simulations, the bombarding ions can penetrate all the way into the FM layer for 20 nm of Au (Figure 24). However, there is no penetration into the FM layer for 40 and 60 nm of Au. The entire AFM layer and some slight effects at the interface can be expected for 40 nm Au. The interface will not be affected due to the bombardment for 60 nm of Au sample.

Figure 33 shows the total number of vacancies only in the entire AFM layer (top) and only in the FM/AFM interface (bottom) as a function of Au thickness (left) and as a function of bombardment dose (right). In both the interface and the AFM bulk, the number of vacancies increases with decreasing the thickness of gold and with increasing the bombardment dose, as expected.

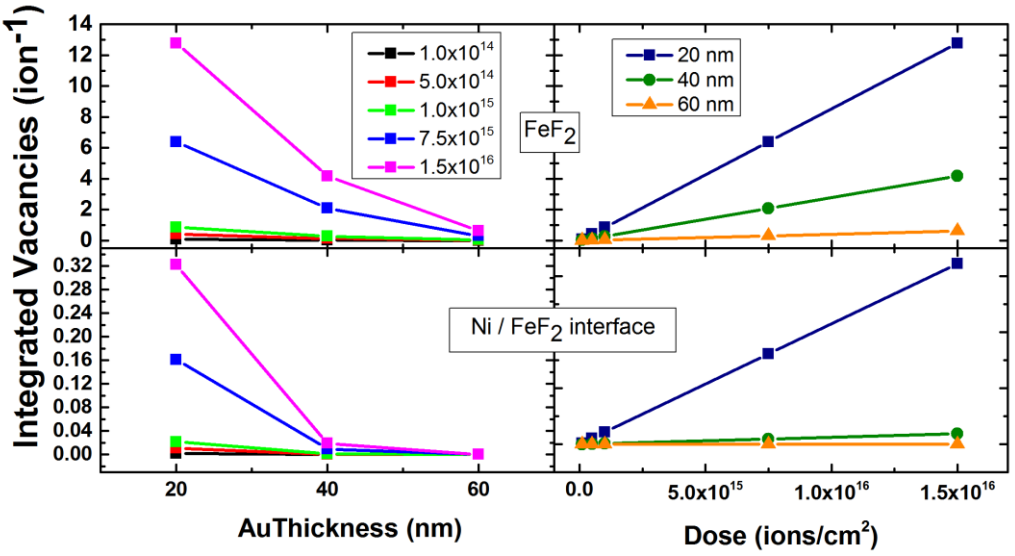

Figure 33. Integrated vacancies as a function of Au thickness (left) and bombardment dose (right). The values are obtained from Figure 24 and multiplied for different doses. The integration is calculated considering only FeF_2 (top) and only Ni/FeF_2 interface (bottom).

Since the bombardment dose was varied by two orders of magnitude, some structural changes might be expected. The room temperature hysteresis loops can be compared to each other to understand whether the FM layer is affected by the bombardment or not. The effect of exchange bias can be excluded at room temperature since FeF_2 is in the paramagnetic state above 80 K.

Figure 34 shows comparison of hysteresis loops at 300 K for three different Au thicknesses. These samples were bombarded with the highest dose ($1.0x10^{15}$ ions/cm^2) of the batch, therefore most likely to be more affected by the bombardment. Samples with 20 and 40 nm of Au capping layer clearly show wider hysteresis loops after the bombardment. The change in H_c due to bombardment is more significant for 20 nm of Au (left). A small change can be seen for 40 nm of Au (middle), whereas the change in

the 60 nm Au sample can be negligible (right). The widening of the hysteresis loops for 20 nm and 40 nm Au samples can be explained by taking into account the defect creation in Ni layer. With this high dose, there are possible scenarios: i) the number of defects is enough to create pinning sites (domain walls) in the FM and ii) the interface mixing is high enough and causes larger roughness for the 10 nm Ni layer. In addition these two situations can also simultaneously present. Therefore a higher magnetic field is required to switch the magnetization.

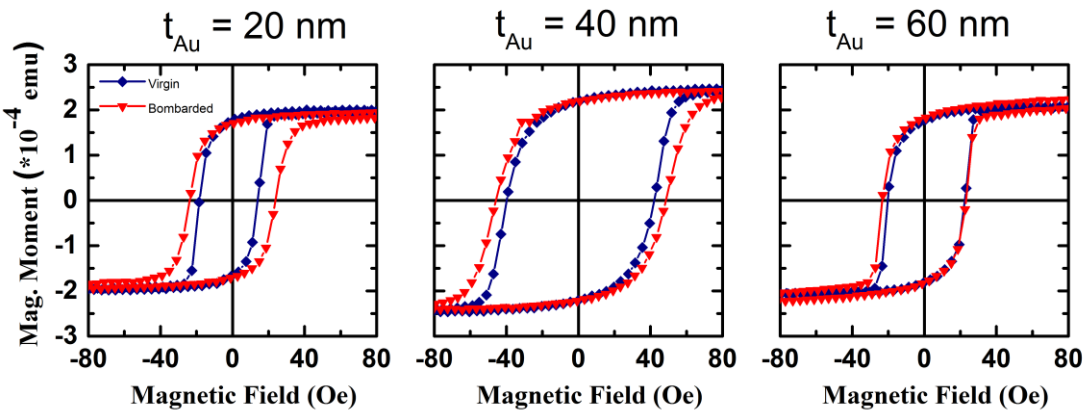

Figure 34. Hysteresis loops before and after the bombardment with the highest dose at 300 K for three gold thicknesses.

Contrary to expectations from simulation (Figure 33), the experimental data shows a complete different behavior, especially for doses higher than 1.0×10^{15} ions/cm^2 (Figure 35). In order to analyze Figure 35 in detail, we can separate the results in two regions; low and high dose regions. In low dose region ($< 10^{15}$ ions/cm^2), the change in the exchange bias due to the bombardment is higher for thinner Au, as expected from

the simulation. In other words, the biggest change up to 30 % occurs in 20 nm Au, while the change as high as 20 % and 15 % occurs for 40 nm and 60 nm of Au samples, respectively. In high dose region (> 10^{15} ions/cm^2), the change in the exchange bias is decreasing to 10 % for 20 nm Au, while increasing up to 80 % and 65 % for 40 nm and 60 nm Au samples, respectively. In conclusion, the change in the exchange bias for thinner Au is higher at low bombardment dose and lower for high bombardment dose, contrary to linear dependence in the simulation (Figure 33).

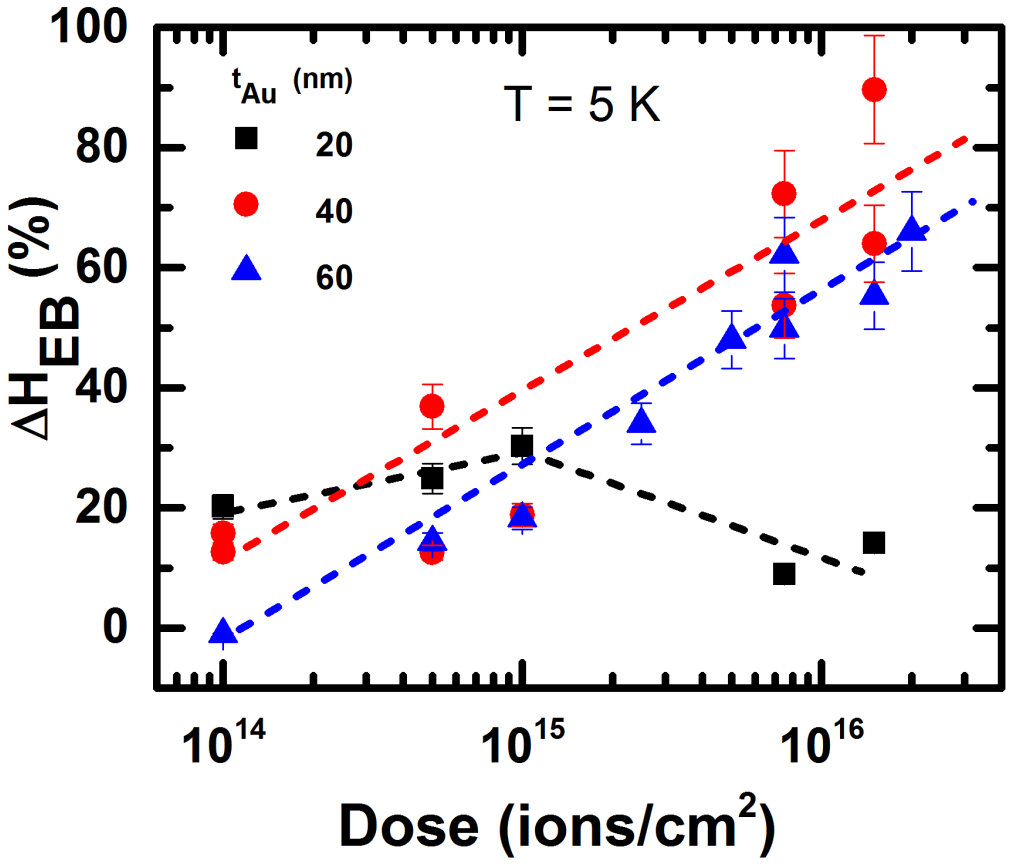

Figure 35. The change in the exchange bias as a function of bombardment dose for three Au thicknesses. The data is obtained from individual hysteresis loops for each sample before and after the bombardment upon field cooling to 5K. The error bars are statistically obtained from different samples for repeated doses and same thicknesses. Notice that the X-axis is on a log scale.

The effect on the change of the exchange bias for different capping layer thicknesses indicates the presence of more than one mechanism which dominates the overall behavior. For example, in the case of thin capping layer (20 nm), the entering ions create defects in all three regions; in the AFM bulk, at the FM/AFM interface, and in the FM layer. Therefore, the contributions of each individual part may differ and we can only measure the average of all. For thicker capping layer (60 nm) the ions can create defects only in the part of the AFM layer that is away from the interface.

3.8. Decoupling of coercive and exchange bias fields

In order to show typical temperature dependence, exchange bias and coercive field values for 40 nm Au extracted from each individual hysteresis loops and plotted in Figure 36. There is no exchange bias above 80 K which is established during the field cooling across the Neel temperature of FeF_2 (~79 K). A rapid increase on exchange bias field from the transition to 40 K is observed. The H_{EB} reaches its maximum value at around 40 K and flattens of upon further cooling. The coercive field mostly behaves as expected from a FM film except a slight change that can be attributed to the AFM transition around 80 K.

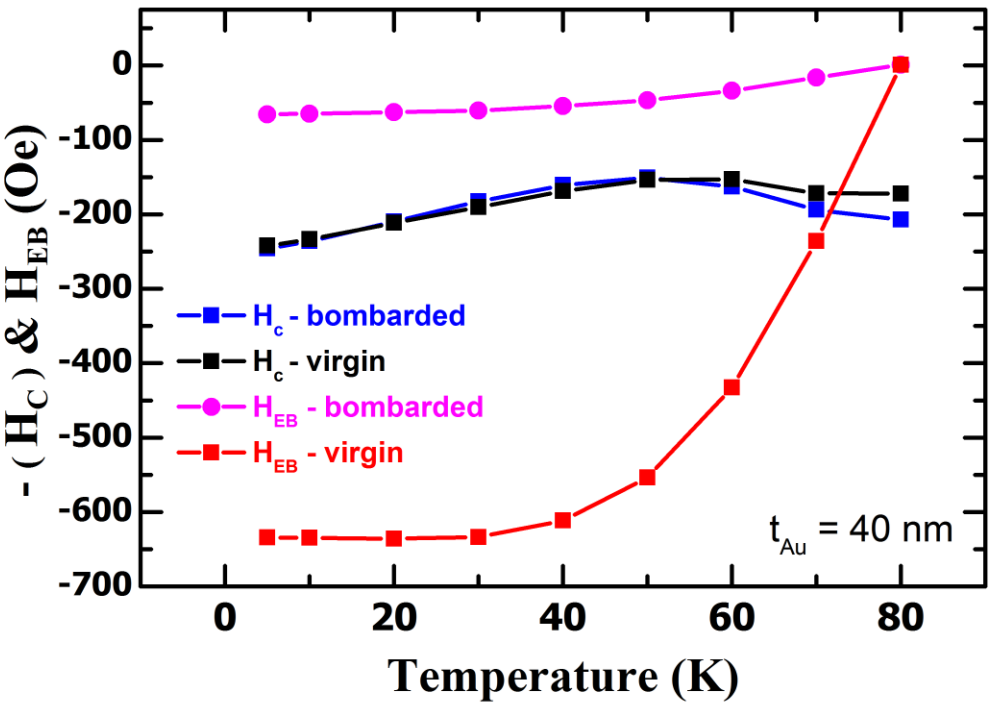

Figure 36. Temperature dependence of coercive field and exchange bias field for 40 nm Au samples. The data taken after the bombardment with 1.5×10^{16} ions/cm^2 was also included for comparison.

The extracted exchange bias and coercive field values for the same 40 nm Au sample after the bombardment with 1.5×10^{16} ions/cm^2 are added into Figure 36. Although the exchange bias field is decreased to 80 % with this highest bombardment dose (see also Figure 35), the coercive field remains the same after the bombardment. Similar behavior is observed for all samples. For 60 nm Au, the change in exchange bias field is ~60 % for the same bombardment dose. These findings reveal two important conclusions: i) the exchange bias and coercive fields are decoupled and ii) exchange bias field can be fully suppressed without affecting the interface.

3.9. Discussion

Since the bombardment took place well above the Néel temperature and measurement protocols are kept the same, time and temperature dependent effects [105, 112] or changes in the frozen-in AFM structure [113] can be neglected. The change in the H_{EB} with Au thickness (Figure 31), in other words the depth dependence of defects, is independent of the microscopic or macroscopic sample morphology since only the Au layer is used to manipulate the ion penetration depth and therefore the damage profile. In addition, we used low dose light-ion bombardment for the depth dependence of defects; therefore the damage is low enough not to be detected by XRR and XRD (Figure 25 and Figure 27).

The influence of the AFM bulk on exchange bias is further supported by considerations regarding the length scales in the experiment (Figure 31). For Au thicknesses less than ~ 30 nm, which include a defect creation at the interface in addition to the FeF_2 bulk, $\Delta H_{EB} / H_{EB}^{v}$ peaks at 35 %. The width of this interface related maximum is 20 nm. The plateau immediately after the peak extends for 50 nm with a change of $\Delta H_{EB} / H_{EB}^{v}$ = 20 %. Such a constant exchange bias reduction over almost three times the peak width is unlikely even considering an asymmetric damage profile of the interface. Consequently, the plateau in $\Delta H_{EB} / H_{EB}^{v}$ is only explained by contributions from the bulk of the antiferromagnet.

The dose dependence for fixed Au thicknesses reveals the importance of the number (or intensity) of defects as well as their locations. Unexpected lower change in the H_{EB} for 20 nm whereas higher change for 40 nm Au by high-dose ion bombardment (Figure 35) suggests that possible mechanisms and individual contributions of involving parts on exchange bias needs to be separately considered.

Although an enhancement of H_{EB} is expected [114], we observe that defect creation always decreases the magnitude of H_{EB}. This can be related to a diminished AFM order and reduced AFM anisotropy, which can lead to an increased number of freely rotatable Fe moments. Those moments do not further contribute to the density of pinned uncompensated moments, which further decreases H_{EB} [46, 98, 101, 102]. In addition, this reduces the AFM domain size, which was reported to decrease the exchange bias in $Fe_xZn_{1-x}F_2$ [115]. We note that according to the domain state model [96, 97] H_{EB} increases with the number of uncompensated moments, which has been experimentally supported by measurements of $Co_xMg_{1-x}O$ [96, 97] and $Fe_xZn_{1-x}F_2$ [116, 117]. This does not contradict our results but highlights that exchange bias crucially depends on the type of defect created, i.e. pinned or unpinned uncompensated magnetization. The existence of uncompensated magnetization in the AFM bulk [46, 47] and intrinsic exchange bias, i.e., exchange bias observed in the system without a ferromagnet, [118] has been shown previously, but our results unambiguously show contributions to the exchange bias.

Below t_{Au} = 40 nm, defect creation in the AFM bulk, at the FM/AFM interface and in the FM needs to be taken into account simultaneously. Within the FM layer defects alter the magnetic domain structure, leading to pinning sites for FM domains [119]. Our experiments do not show an enhanced coercivity by bombardment with doses lower than $10x10^{15}$ ions/cm^2. Above this dose, the coercivity of Ni is enhanced for 20 nm and 40 nm Au samples, but not for 60 nm of Au (see Figure 34). This also gives further support to the simulation results which show that the FM layer is affected up to 40 nm of Au. Such enhanced coercivity upon ion bombardment was observed for FeMn/FeNi exchange bias system [120], but not for NiO/FeNi [105] and therefore appears to depend on the specific sample morphology.

It has recently been shown that the lateral and in-depth domain landscape of the FM strongly influences the exchange bias [60, 111]. Previous studies on FeF_2 show a decrease of H_{EB} with increasing interface roughness [22]. In our study, XRR results show that chemical profiles are unaltered by bombardment on sub-nm length scales for low doses (Figure 28). In the case of high doses, contrary to expectations, it seems the bombardment causes a decrease in the interlayer roughness, which would increase the exchange bias field. It is difficult to ascertain the effect of changes in roughness in our samples since the structural analysis for high dose bombardment has not completed by the time of writing this thesis. Nevertheless, the exchange bias field for samples with polycrystalline AFM layers appear to be less sensitive to roughness [21].

Magnetic defects near the interface increase the areal density of uncompensated moments. This is expected to enhance H_{EB} [4, 98, 100]. In radiation damage

experiments, however, increasing number of defects close to the interface decreases the H_{EB} [114]. Therefore, the balance between enhancement and decrease of H_{EB} is complex and is expected to highly depend on the ratio between defects in the FM, interface and AFM bulk. This is experimentally supported in our studies by the dose dependency for three Au thicknesses, where radiation damage selectively creates defects of different amounts within these regions (Figure 35).

Below a certain amount of defects (< ~1.0×10^{15} ions/cm^2), contribution from the FM seems not to be significant (Figure 35). This can be due to strong exchange interaction within the FM layer. However, even small amount of defects created above Neel temperature is enough to alter the magnetic structure in the antiferromagnet since the point defects can cause a different domain formation upon cooling. It has been shown that the amplitude and direction of the exchange bias field can be controlled with applying external magnetic field [114] if the AFM order was established during the bombardment. This indicates the importance of the magnetic state of antiferromagnet during defect creation, in addition the structural parameters. It can also be attributed to the ion induced chemical disordering of antiferromagnets is much easier than the ferromagnets.

Independent of all possible scenarios, the AFM bulk, the individual contributions of different components and the amount of defects have to be considered to explain all experimental observations.

Investigation of the change in the coercive field, which is another important parameter in an exchange bias system, shows no significant change upon bombardment

(Figure 36). The coercive field and its typical enhancement across the transition are believed to be intimately related to the microscopic origin of exchange bias [121-123]. However, our results demonstrate that there is no direct correlation between H_{EB} and H_C (Figure 36), similar to previous reports [11, 124, 125]. The temperature dependence of coercive field before and after the bombardment does not show a difference and remains almost the same for all samples above 40 nm Au. Although the sample which is bombarded with the highest dose shows 80 % of change in H_{EB}, the temperature evolution of coercivity is not affected by the bombardment (Figure 36). This clearly proves that the mechanism responsible for coercivity and exchange bias must be decoupled and independent. Another important conclusion is that the exchange bias field can be fully suppressed without affecting the interface, since the interface and the FM layer remains unaltered for thick Au samples.

3.10. Conclusion

In summary, we have shown that the AFM bulk has a direct influence on the absolute magnitude of exchange bias. The location of defects created by light-ion bombardment has been controlled by varying an inert capping layer thickness. A change in exchange bias is observed with defects only formed in the FeF_2 bulk, at Au thicknesses where the interface is unaffected. A maximum change of exchange bias is observed if defects are created throughout the bulk of AFM layer and at the FM/AFM interface. In a separate experiment, the number of defects created by ion bombardment

at certain location was controlled by varying the bombardment dose. With highest dose and lower Au thickness, a slight change is observed in H_C which indicates a change in the FM (or FM/AFM interface). Above certain amount of defects, this change in the FM becomes important and enhances the exchange bias. This can be attributed to a balance of several mechanisms. The temperature dependence of H_C before and after the bombardment reveals the independent mechanisms responsible for coercivity and exchange bias. The importance of AFM bulk on exchange bias is further supported by demonstrating the H_{EB} can be fully suppressed without affecting the interface.

3.11. Acknowledgements

Chapter 3, in part, is published in: Ali C. Basaran, T. Saerbeck, J. de la Venta, H. Huckfeldt, A. Ehresmann, and Ivan K. Schuller, "Exchange bias: the antiferromagnetic bulk matters", Applied Physics Letters 105, 072403 (2014). The dissertation author was the primary investigator and author of this material.

Chapter 3, in part, is currently being prepared for publication of the material. Co-authors include T. Saerbeck, J. de la Venta, H. Huckfeldt, A. Ehresmann, X. Batlle, and Ivan K. Schuller, The dissertation author was the primary investigator and author of this material.

I would also like to thank Thomas Saerbeck for the help of structural analysis and writing and Henning Huckfeldt and Arno Ehresmann for performing ion bombardment and SRIM simulations.

4. Role of the ferromagnetic spin structure

In this chapter we present the effect of FM spin structure on exchange bias, which has not been thoroughly investigated. Magnetization measurements of AFM/soft-FM exchange bias bilayers with different FM layer thicknesses reveal a strong deviation from the inverse proportionality dependence. Furthermore, it is shown that this deviation depends on the strength of the exchange coupling, which varies with temperature. The incomplete domain wall model quantitatively explains the experimental results and the observed deviation from the inverse proportionality. These results reveal the active role of the FM spin structure and imply a new paradigm of the exchange bias phenomenon.

4.1. Introduction

Recent observations of different ground states in FM materials such as skyrmions not only indicate new possible applications but also demonstrate the importance of spin textures within the FM [126, 127]. One of the most fundamental interactions which govern such spin formation is the exchange coupling between similar or dissimilar atoms. In addition to self-formation, it is possible to engineer controlled spin structures by choosing the materials and physical parameters. For example in

magnetically hard/soft bilayers, the exchange interaction triggers spring-like (incomplete, i.e., non 180°) domain walls in the soft layer [16, 128-130].

In the case of exchange bias, an analogue to hard/soft FM bilayers, the FM spin configuration perpendicular to the interface can be affected by the exchange coupling. However, since the exchange interaction is short ranged, only the spins close to the interface are taken into account. Therefore, the effect of the spin configuration along the whole thickness of the FM layer has been ignored. All theoretical models to date propose the dependence of H_{EB} with the magnetization (M_{FM}) and the thickness of the FM layer (t_{FM}) as

$$H_{EB} = \frac{\sigma}{M_{FM} t_{FM}} . \tag{4.1}$$

Here, σ refers to the interfacial exchange energy density and includes the exchange parameter (J_{ex}) and the spins of the interfacial atoms (S_{FM} and S_{AF}) [4, 14, 15]. From this equation, the exchange bias field is mainly defined by the three constituents, i) the spin structure of the AFM layer, ii) the spin configuration at the FM/AFM interface, and iii) the thickness and magnetization of the FM layer. The first two contributions, the AFM bulk and the FM/AFM interface, set σ on equation (4.1). Thus, the magnitude of H_{EB} can be predicted for any given M_{FM} and t_{FM}. Experimental results have confirmed this thickness dependence in different magnetic systems [131-133]. However, in these references there is no consideration given to the FM spin configuration which can vary along the FM film thickness, particularly in soft FM materials.

In this chapter we show that the spin configuration along the FM layer thickness plays a crucial role to determine the magnitude of the exchange bias field. It has been assumed till now that the exchange interfacial energy density σ is the only parameter which sets H_{EB} for a given material and thickness. Here we prove the active role of the FM spin configuration on the effect. The inverse dependence of H_{EB} with t_{FM} is no longer valid under certain magnetization reversal mechanisms. Moreover, spin configuration of the FM layer does not only break the inverse dependence with the FM thickness, but also give rise to an anomalous temperature dependence of H_{EB}. The evolution of the FM spin configuration can yield an increase of H_{EB} as temperature raises, contrary to conventional exchange bias systems where higher temperatures decrease the exchange coupling and therefore decrease H_{EB}. These facts add an extra degree of freedom in the design of exchange bias -based devices and insights on the nature of the exchange bias phenomenon.

4.2. Sample fabrication

In order to investigate the effect of magnetic structure in FM, the thickness of the FM can be varied while keeping the other parameters are the same. FeF_2 (70 nm) / Py (t_{FM}) / Al (4 nm) films were deposited by electron beam evaporation with 1 Å/s deposition rate, at a base pressure of $2x10^{-7}$ Torr. Six FM thicknesses (t_{FM} = 15, 30, 50, 70, 100 and 140 nm) were prepared in one deposition using a stepper motor-controlled

shutter, in order to avoid run-to-run differences. The MgF_2 (110) single crystal substrates were heated to 500 ºC for 1 hour before the deposition. Then the temperature was reduced to 300 ºC which is also the deposition temperature for FeF_2. Under these conditions, FeF_2 was grown epitaxially. The textured Permalloy (Py), the FM layer, was deposited at 150 ºC. To prevent the oxidization, 4 nm of Al capping layer was deposited after reducing the temperature below 50 ºC.

4.3. Magnetic characterization

All samples were measured using a SQUID magnetometer. Above the Néel temperature of FeF_2 (T_N = 79 K), Py shows a well-defined magnetic easy axis parallel to the AFM easy axis of FeF_2, which is along [001] direction. The following experimental protocol was used for all samples to obtain truly comparable measurements. Samples were saturated at 150 K with 1000 Oe external field applied along the easy axis. 1000 Oe was chosen to be enough to saturate various thicknesses of Py. Then the magnetic field was reduced to the cooling field H_{FC} = 50 Oe and kept during cooling to 10 K, the lowest measurement temperature. After measuring a magnetic hysteresis loop at 10 K, the sample temperature was raised up to 70 K at H = 0 and a second loop was measured at this temperature. 10 K and 70 K were chosen in order to compare either a strong or a weak exchange coupling established, respectively.

Figure 37 shows hysteresis loops at 10 K and 70 K after 50 Oe field cooling for three Py thicknesses; 15, 70, and 140 nm. The magnetic field was always swept from

positive to negative saturation. The magnetization values were normalized to the saturation after a diamagnetic correction by subtracting a linear slope. For all thicknesses, the magnetization reversal mechanism is reversible with a slow approach to the negative saturation at 10 K, whereas it is irreversible at 70 K featuring square loops with a sharp magnetization reversal. Similar magnetic behavior was observed for any t_{FM} . These remarkable changes in reversibility with temperature indicate the formation of different spin configurations in the FM layer, which is induced by the temperature dependent AFM-FM exchange interaction.

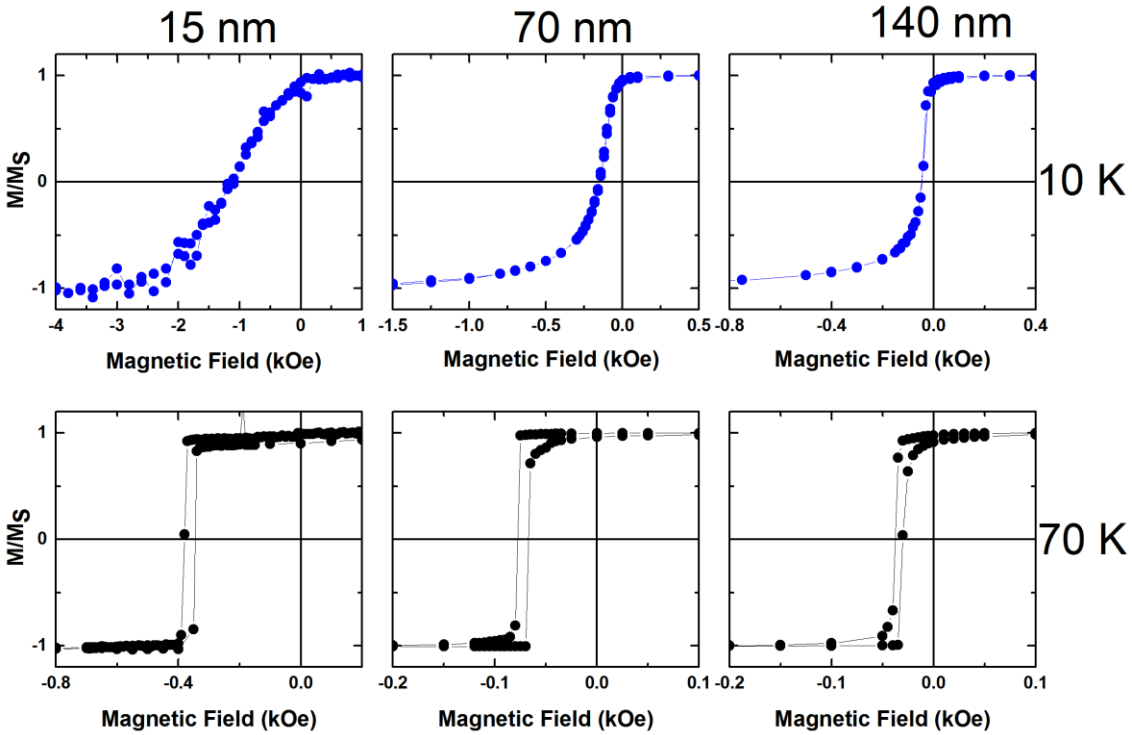

Figure 37. Hysteresis loops for FeF_2 (70 nm) / Py (15, 70, and 140 nm) films at T = 10 K (top) and T = 70 K (bottom). Symbols are the experimental data and the lines between symbols are guide to the eye.

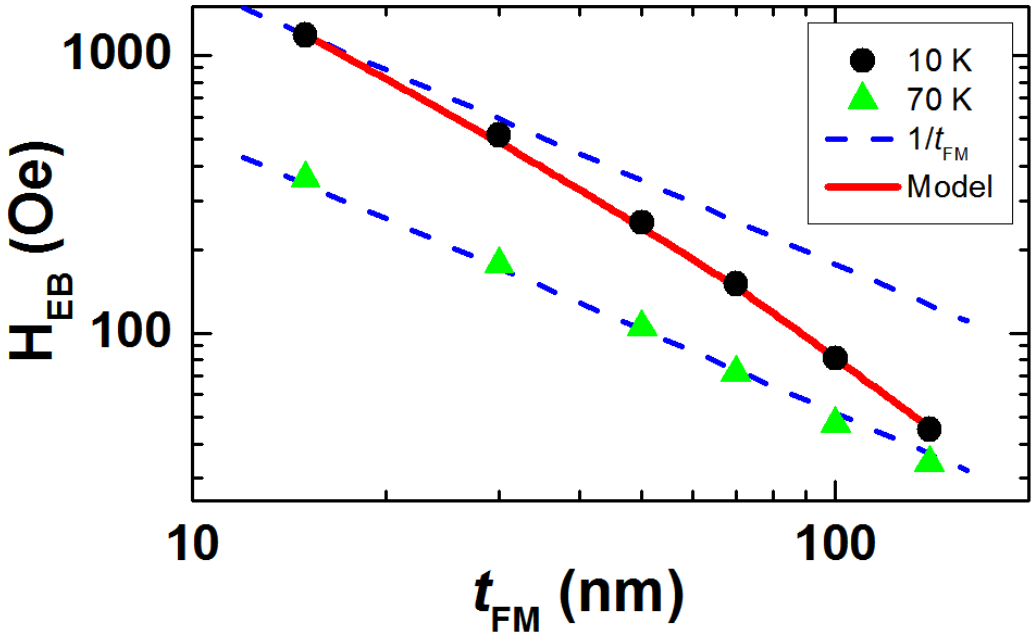

Figure 38. The obtained exchange bias fields as a function of the thickness of FM layers at 10 K and 70 K (black circles and green triangles, respectively). Dashed blue lines represent the expected behavior from equation (4.1). The solid red line is calculated from the model.

Similar hysteresis loops after following exactly the same experimental protocol were measured for all six FM thicknesses and the exchange bias fields were obtained. Figure 38 shows exchange bias fields as a function of the thickness of FM layer in a logarithmic scale for both 10 K and 70 K. In this logarithmic scale the dependence of exchange bias field on FM thickness $H_{EB}(t_{FM})$ given by formula (4.1) appears as a straight line with a negative slope -1. Dashed blue lines plot this $1/t_{FM}$ dependence for two different σ values (σ values are changed in order to induce the temperature effect since the temperature does not appear in the equation). At 70 K, the obtained

$H_{EB}(t_{FM})$ values follow the blue dashed line, i.e., the well-known $1/t_{FM}$ dependence (equation(4.1)). However, it significantly deviates from this law at 10 K for the same samples. The experimentally obtained H_{EB} values gradually diverge from this line as t_{FM} increases, giving a much lower H_{EB} than predicted by equation (4.1).

The dashed blue line for 10 K can also cross a different data point. However the whole data points never fits on a single linear line. The line is drawn in such a way that the lowest Py thickness fits on it. Therefore, increasing the thickness of FM layer yields much lower exchange bias field than the expected from formula (4.1). This is a reasonable approach since the deviation is more likely in thicker samples and it is supported in our model. The deviation found in the data and model is an evident proof that the exchange bias field is determined by not only the spin configuration at the FM/AFM interface or the FM layer thickness, but also the spin configuration along the FM thickness.

4.4. Temperature dependence

The influence of FM spin structure does not only appear on the thickness dependence of H_{EB}, but also gives rise to an anomalous temperature dependence. Figure 39 shows hysteresis loops at different temperatures for the $t_{FM} = 140$ nm sample. The sample was cooled to 10 K in 50 Oe cooling field and the first loop was recorded at this temperature. The other loops were consecutively measured every 5 or 10 K towards the higher temperatures. The plots are divided into two temperature ranges, 10 to 50 K

(top) and 55 to 75 K (bottom), in order to highlight the change in the reversal mechanism and the evolution of H_{EB}.

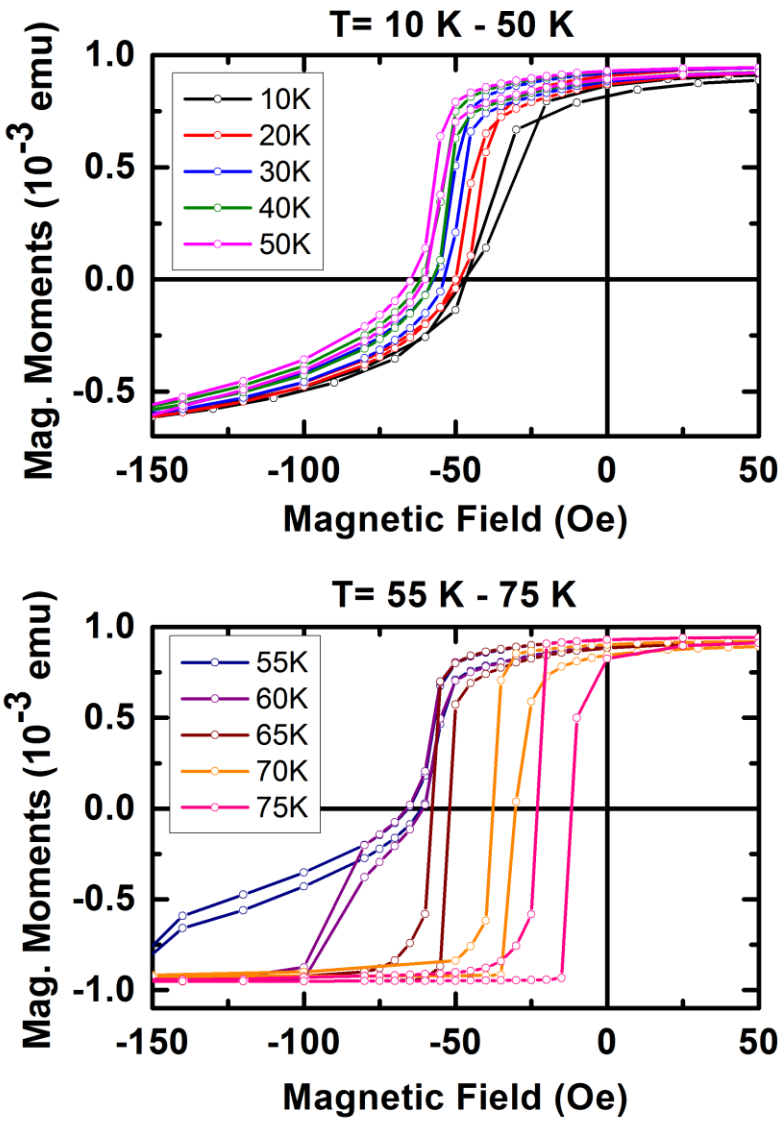

Figure 39. Hysteresis loops for t_{Py} = 140 nm sample after 50 Oe field cooling. The temperature ranges from 10 K to 50 K (top), 55 K to 75 K (bottom).

Between 10 and 50 K, the shape of the hysteresis loops does not change and the magnetization reversal mechanism is mainly reversible with a slow approach to the negative saturation. Above 55 K, the irreversibility which is associated with loop opening and sharp switching appears. Besides this change in the reversal mechanism with temperature, the most surprising result is that the loop shift is not decreasing as the temperature increases. This anomalous temperature dependence is opposite to expected behavior since the exchange coupling weakens at higher temperatures.

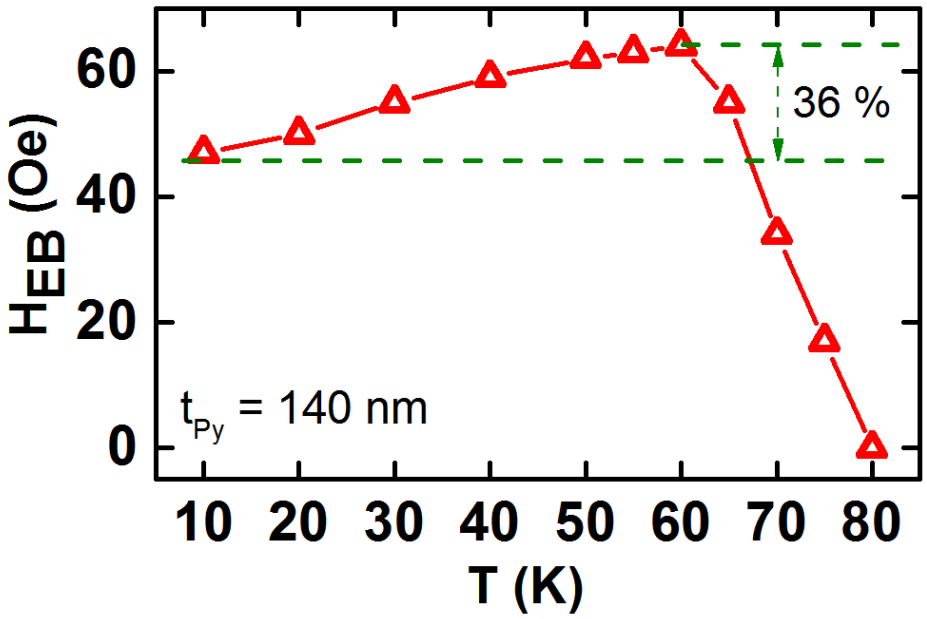

Figure 40. Temperature dependence of the exchange bias field for FeF_2 (70 nm) / Py (140 nm).

In order to study this unexpected behavior in more detail, the absolute values of exchange bias field ($|H_{EB}|$) for $t_{FM} = 140$ nm were extracted from Figure 39 and plotted in Figure 40. The $|H_{EB}|$ gradually increases by 36 % up to 60 K and then decreases.

However, the exchange coupling at the interface and therefore H_{EB} is expected to decrease with increasing temperature as has been observed in many exchange bias systems even in bilayers with the same antiferromagnet, FeF_2 [11, 43, 134]. Therefore, this anomalous behavior indicates the importance of the thermal evolution of the FM spin structure.

4.5. Discussion

In order to explain these findings, we used the incomplete domain wall model which is based on incoherent rotations of FM spins (see Chapter 1.3 for more details). The hysteresis loops were simulated for all thicknesses at 10 K where the magnetization rotation mechanism is reversible (Figure 41). The parameters used for this simulation were: $A_{AF} = 3.1 \times 10^{-8}$ erg/cm and $K_{AF} = 1.35 \times 10^{8}$ erg/cm^3 [18, 91], $J_{AF-FM} = 2$ erg/cm^2 and $J_{FM} = 18$ erg/cm^2 as obtained from a fit of all $M(H)$ curves. $K_{FM} = 4 \times 10^{3}$ erg/cm^3 was obtained from the saturation field along the hard axis of the FM layer, and m_i was calculated from the Permalloy magnetization $M_{NiFe} = 800$ emu/cm^3 as $m_i = M_{NiFe} \Delta t_{FM}$. The thickness of each FM sublayer Δt_{FM} was taken as 1 nm. All the parameters were kept constant for all the FM thicknesses simulated. Only the number of sublayers N was varied to attain $t_{FM} = N \Delta t_{FM}$.

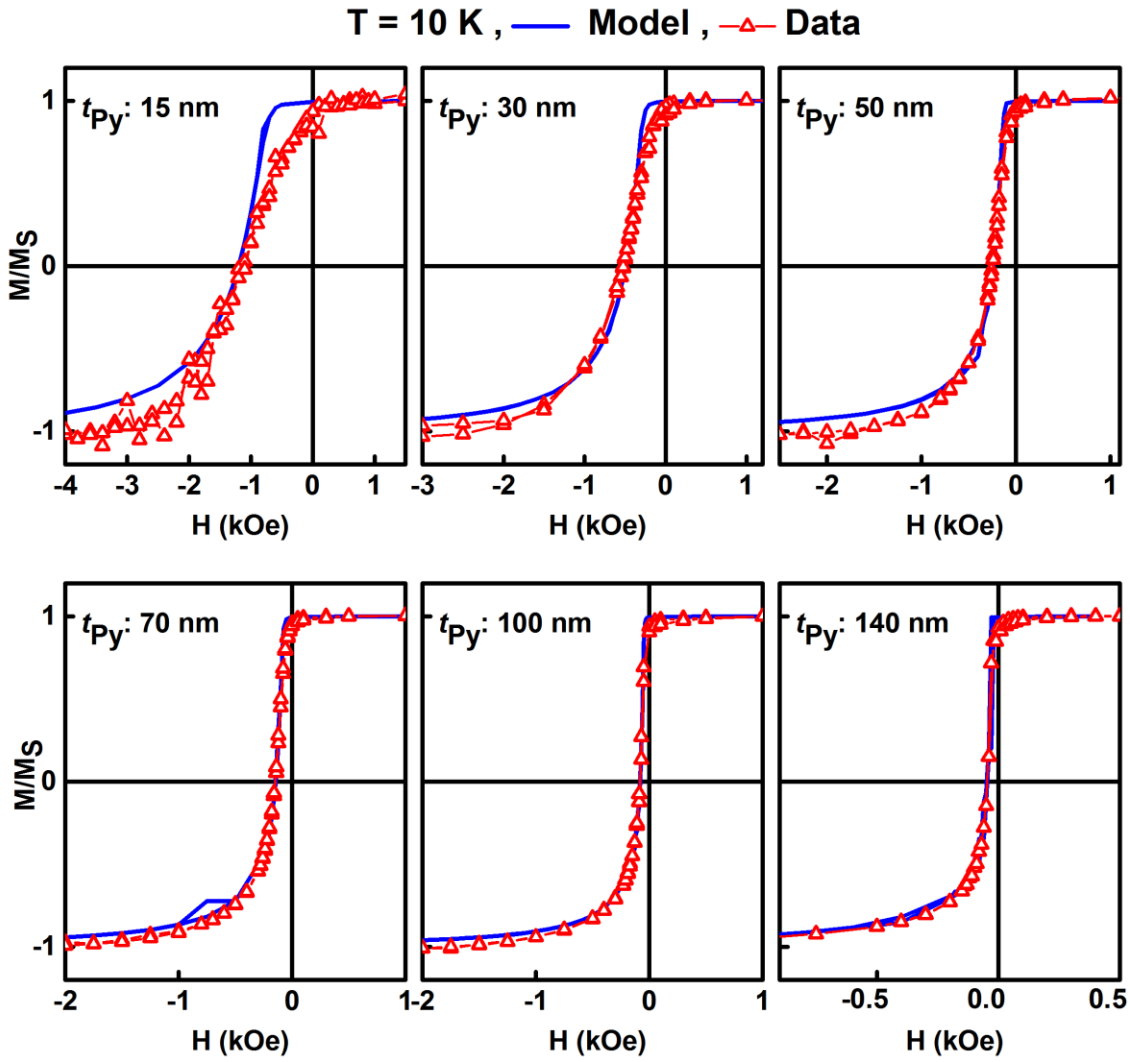

Figure 41. Comparison of hysteresis loops for all Py thicknesses at 10 K after 50 Oe field cooling. Solid blue lines are calculated from the model using the parameters given in the text. Open red triangles are experimental data.

Simulated $M(H)$ curves are shown in Figure 41 together with experimental data at 10 K. The simulation follows very well the shape of the hysteresis loops; the fast decay of the magnetization approaching the exchange bias field and the slow saturation at negative fields. The model predicts a reversible magnetization reversal mechanism

even for the thickest sample, $t_{Py} = 140$ nm, which was confirmed by SQUID measurement. The exchange bias values are in a good agreement for all thicknesses. The simulated hysteresis loop for $t_{Py} = 15$ nm is slightly different in positive branch and follows much sharper switching than the data. This could be explained considering the crystallographic properties of this particular sample, which maybe different than the others.

In Figure 38, the theoretical dependence of $H_{EB}(t_{FM})$ (solid red line) extracted from the simulated $M(H)$ curves is compared with experimental values at 10 K (solid black dots). The agreement is excellent, quantitatively obtained the deviation of the exchange bias field from the inverse proportionality (dashed blue line). Therefore, we can conclude that the in-depth spin configuration induced by exchange interaction on the FM is responsible for the deviation in the magnitude of the exchange bias field.

Although incomplete domain walls were studied in FeF_2/Fe thin films [61], no deviation from $1/t_{FM}$ was observed. In fact, the exchange bias field was predicted to follow the inverse proportionality rule in equation (4.1). In order to observe such a deviation, the FM material must be magnetically soft. It is worth to mention that we have also investigated Ni/FeF_2 bilayer. In this case, the deviation for thick Ni is much smaller than for Py. Moreover, the magnetization reversal mechanism for Ni samples is irreversible above ~30 nm thickness even at low temperatures (~10 K). This indicates the observed deviation is related to the magneto crystalline anisotropy strength of the

material. As a result, the effect of the spin structure along the FM thickness on exchange bias systems is much more important for the soft magnetic materials.

The reversal mechanism is different at higher temperatures. The square shape of the hysteresis loops at 70 K suggests a nucleation of opposite FM domains with domain walls perpendicular to the FM/AFM interface. Reversing the applied magnetic field causes a domain wall motion, which is seen as irreversibility, rather than a rotation. This domain structure formation in the FM for all thicknesses yields a $1/t_{FM}$ dependence as shown in Figure 38 at 70 K, and as it was proved in many other systems [135].

The thermal evolution of the FM spin structure could explain the anomalous temperature dependence of H_{EB} in Figure 40. When the exchange bias field is strong enough, i.e. at low temperatures, the magnetization reversal occurs by incoherent rotation of the planar FM sublayers, creating a spring-like domain wall parallel to the FM/AFM interface. This FM spin configuration yields a much lower magnitude of H_{EB} than predicted by equation (4.1), as seen more noticeable in thicker FM samples. However, the magnetization reversal at higher temperature is dominated by nucleation of inverse domains and domain wall motion. This mechanism follows equation (4.1), and leads to a higher magnitude of H_{EB} with respect to the parallel domain wall mechanism. Consequently, H_{EB} increases with temperature as the FM spin configuration evolves between these two mechanisms. It is worth to mention that the exchange interaction decreases as temperature increases. Thus, a reduced value of H_{EB}

is expected as temperature rises. However, the thermal evolution of the FM spin structure can overturn this trend and may cause a higher exchange bias field.

4.6. Conclusion

In summary, the dependence of exchange bias on the FM thickness was investigated. Two important conclusions are revealed by the experimental results: i) deviation from the inverse proportionality of $H_{EB}(t_{FM})$ and ii) the enhancement of H_{EB} with increasing temperature. The incomplete domain wall model explains these experimental findings and points out the importance of the FM spin structure in the exchange bias phenomenon. Therefore, we can conclude that any theory on exchange bias must take into account the spin structure along the FM, besides the interface and AFM bulk. The active role of FM spin structure perpendicular to the interface could be used in the design of exchange coupling-based devices or hard/soft heterostructures for ultra-high density storage media.

4.7. Acknowledgements

Chapter 4, in part, is currently submitted to Physical Review Letters for publication of the material. Co-authors include R. Morales, J.E. Villegas, D. Navas, N. Soriano, B. Mora, C. Redondo, X. Batlle, and Ivan K. Schuller. Ali C. Basaran worked

on the sample design, performed the fabrication, measurement, and analysis for this work, and will be the second author on the paper.

I would like to thank Rafael Morales for the idea, simulations, and useful discussions.

5. Other studies

During my PhD research, I have been strongly encouraged to study on many different subjects in parallel. Involving in several collaborations and projects yields much more than the ones summarized in previous chapters. This chapter consists of brief descriptions of these other projects.

5.1. Search for new superconductors

One of the most fundamental discoveries in condensed matter physics from the last century is the appearance of superconducting state of matter [136]. Superconducting materials exhibit zero electrical resistance and expel the magnetic field (Meissner effect), when cooled down below a critical temperature (T_C). The physical origin of the transition from the normal to the superconducting state is only partially understood. Conventional superconductivity, which applies mainly to low temperature superconductors, can be described microscopically by BCS theory [137]. However, the mechanisms behind high temperature superconductivity [138] and the new emerging Fe-based superconductors [139] are still under debate.

Synthesizing novel superconductors has been an ongoing challenge in the field since their discovery. A comprehensive theory that describes how to synthesize new superconductors is still missing, in spite of the enormous theoretical effort [140-142]

that has gone into understanding their behavior. Nevertheless, some interesting correlations between normal and superconducting state properties do exist [143]. Furthermore, superconducting materials, in general, are very complex and exist only in a small region of a multielement metallurgical phase diagram. Therefore superconductors are hard to find as they may be embedded in non-superconducting materials or they just may be overlooked. The latter was demonstrated by the discovery of superconductivity in MgB_2 in 2001 [144], almost fifty years after the material was synthesized.

In order to increase the chances of finding new superconducting materials, a combinatorial search can be used [33]. This method is based on the synthesis of inhomogeneous samples consisting of several phases with different stoichiometries. The use of a technique that can detect superconductivity selectively and with very high sensitivity would enable probing of all present phases in a sample at the same time. We have significantly advanced the methods for detecting superconductivity by developing a highly sensitive and selective microwave technique.

5.2. Magnetic field modulated microwave spectroscopy

Microwave absorption of a material drastically changes when the material cross a superconducting transition. However, a change in the microwave absorption associated with other type of transitions could also be possible. Since the search for "new superconducting materials" involves a very broad range of temperature scans, the

ability of distinguishing the superconducting from non-superconducting transitions is crucial. This especially comes into prominence when an “unknown” material is investigated. In our studies, we used Magnetic Field Modulated Microwave Spectroscopy (MFMMS) as a powerful technique in the search for new superconductors. MFMMS measures reflected microwave power as a function of temperature. The modulation induced by the external ac magnetic field enables the use of phase locked detection with the consequent sensitivity enhancement. We highlight the main advantages of MFMMS in terms of its sensitivity and selectivity when combining with low field scans.

MFMMS uses a customized X-band Electron Paramagnetic Resonance (EPR) apparatus. It includes a microwave circuit, a phase sensitive detector, an electromagnet, a cavity resonator, and a flow cryostat. The cryostat allows sweeping the sample temperature between 3.8 K and 300 K. The dual-mode cavity can be used to produce two resonances at 9.4 and 9.6 GHz that correspond to modes where the microwave magnetic field is perpendicular (TE_{012} mode) or parallel (TE_{102} mode) to modulation field, respectively. An automatic frequency controller continuously adjusts the microwave frequency to the resonance frequency of the cavity. The sample is placed at the center of the cavity where electric field component of the microwaves is minimum and magnetic field component is maximum. More details about the technique and its applications to superconducting and non-superconducting materials can be found in our review article [Accepted, Reports on Progress in Physics (2014), in press].

We have analyzed more than two thousands samples to date, including several different types of superconducting and non-superconducting phases. Besides extensively reported in the review article, we have two more publications. We identified a known superconducting phase in a new compound [33]. We also found a new magnetic phase in Pr-Si-C system [34].

5.3. Search for superconductivity in exotic materials

Since material synthesis is the bottleneck in the search for new superconductors we have extended our searches beyond artificially prepared materials to naturally stabilized ones. Extraterrestrial materials are particular interesting. The analysis of extra-terrestrial materials allows measurement of materials that cannot be synthesized in the laboratory. It is now well recognized that in many meteoritic classes there are pre-solar grains of oxides (Al_2O_3, $MgAl_2O_4$, $CaAl_{12}O_{19}$, TiO_2 , $Mg(Cr,Al)_2O_4$ as well as SiC, diamonds, graphite, Si_3N_4, and deuterium enriched organics [20-22]. These molecules have been formed under some of the most intense physico-chemical environments in the Universe, including supernovae and stellar outflows. These meteorites are some of the oldest, most pristine objects in the solar system and have been created under a wide range of pressure, temperature, and chemistry, ranging from highly reduced (e.g. iron meteorites) to highly oxidized meteorites containing organic material (carbonaceous chondrites). It is during such severe processes when the formation of exotic chemical species may be created and may constitute the components

of micrometeorites. Note that the conditions under which these form in many cases are not attainable under ordinary laboratory conditions and therefore they provide a unique source of exotic materials.

We have found no evidence for superconductivity in the 65 micrometeorite investigated to date. In most of them, MFMMS measurements indicate the presence of magnetite. The search for new superconducting phases in exotic materials is still an ongoing project [in press].

5.4. Superconducting vortex pinning in conformal crystals

At the intersection of magnetism and superconductivity, we have investigated the superconducting vortex pinning in conformal crystal geometry [35]. Vortex dynamics in superconducting thin films with artificial pinning centers have been of great interest. A central problem in these studies is how to improve the critical current density of a superconducting device by choosing a suitable artificial pinning center distribution.

In our studies, we compared the magnetoresistance of a conformal crystal and a randomly diluted artificial pinning center pattern with that of a triangular reference lattice. We have found that in both cases the magnetoresistance below the first matching field of the triangular reference lattice is significantly reduced. For the conformal crystal, the magnetoresistance is below the noise floor indicating highly effective vortex pinning over a wide magnetic field range. Further, we have discovered that for

asymmetric patterns the magnetoresistance curves are mostly symmetric. This implies that the enhanced vortex pinning is due to the commensurability with a stripe in the non-uniform artificial pinning center pattern and not due to a rearrangement and compression of the whole vortex lattice

5.5. Competing correlation length scales in exchange coupled nanostructures

Geometric confinement of magnetic structures down to critical length scales such as the FM exchange length or the domain wall width results in intriguing new phenomena not observed in the corresponding bulk material. In this regard, a proximity effect such as the exchange bias phenomenon is of particular interest.

In this study, we demonstrated that dimensional constraints of the FM correlation length can drastically affect the AFM domain structure. We used photoemission electron microscopy (PEEM) combined with X-ray magnetic circular dichroism (XMCD) techniques for direct observations of the spin configuration at both sides of the FM/AFM interface. The measurements revealed that the final spin structure is determined by the competing balance between the two dissimilar magnetic length scales. Direct imaging the spin configurations at both sides of the interface offers a unique advantage of probing the role of domain size and the competing interfacial exchange-coupling and lateral contributions.

It is widely accepted that the FM layer does not actively contribute to the domain formation in the antiferromagnet. However, we demonstrate that if the FM layer

is sufficiently thin (below about 10 nm) the competing interactions with the proximal AFM system lead to tunable configurations of coexisting exchange bias domains with opposite orientations. This is due to the different length scales of the two dissimilar magnetic materials. The FM order was further geometrically constrained by antidot patterning. This leads additional positive exchange bias domain formations below a critical antidot interspace (in the order of a few FeF_2 crystal domains).

These remarkable findings revealed that the AFM domain formation can be affected by the FM layer. This brings another aspect to the understanding of the origin of exchange bias. A manuscript was written and it is still circulating among co-authors at this time.

5.6. Phase coexistence in V_2O_3/Ni bilayers

It is possible to tune novel functionalities in hybrid materials by the transfer of the properties of one material into another or by new phases that may appear at the interfaces between dissimilar materials [145]. For example, unexpected magnetic properties are known to be induced in magnetic thin films when in proximity with complex oxides undergoing phase transitions [146]. This is more extreme when different lengths scales are competing in each material [147].

In this manner we have studied the magnetization dynamics in Ni/V_2O_3 bilayers by employing the ferromagnetic resonance technique. We have found a drastic modification of the magnetization dynamics of Ni films caused by the first order

structural phase transition of V_2O_3. Ferromagnetic resonance measurements across the structural phase transition show diverse features that cannot be interpreted solely by magneto-elastic effects. We have found two well-defined resonance modes for Ni and an increase in the line width of each mode across the structural phase transition. The temperature dependence of the intensity of the peaks suggests that the two resonances arise from the coexistence of the two V_2O_3 crystallographic phase domains in contact with the magnetic Ni domains. Our results highlight the strong coupling of the lattice dynamics of a complex oxide to the magnetization dynamics of a ferromagnet in proximity. The existence of similar effects can be extended in other hybrid materials with structural phase transitions. At this stage, we are still writing a manuscript regarding these remarkable findings.

5.7. Investigation of exchange bias in complex oxide heterostructures

Many studies imply that very regular and smooth interfaces generally do not exhibit exchange bias [148]. This is a very important observation since the tendency has been to try to enhance the exchange bias by improving interface quality. However, the key may be precisely in the opposite direction although the type of defects needed to increase the exchange bias is not known.

Recently, we have studied the influence of defects on enhanced coercivity and possible exchange bias in the (La,Sr)$CaMnO_3$ (LSMO) films. We used 100 nm thick single crystal LSMO films which was grown on SrTiO3 substrates and introduced

defects using alumina masks and O- ion bombardment. The alumina mask was prepared by anodization technique and transferred on surface of the samples. The masks contain 60 nm diameter holes with 110 nm spacing through which O- ions can pass and create cascades of defects in laterally confined regions of the LSMO film. We compared the magnetic properties of the samples before and after the bombardment. We have found that the irradiation reduces the sample magnetization and enhances coercivity. The coercivity enhancement is dramatically higher at low temperatures. These observations are consistent with the possibility that ion irradiation increases AFM interactions in the portion of the LSMO film and exchange coupling between FM and partially AFM regions. Alternatively, ion irradiation may affect magnetic anisotropy.

Although the existing results are consistent within a set of samples, we are preparing more samples to confirm the previous results and obtain more data points for better understanding. This is an ongoing project at this time.

5.8. Acknowledgements

This chapter contains work performed in several different projects. Some of them have been previously published in:

J. de la Venta, Ali C. Basaran, T. Grant, A. J. S. Machado, M. R. Suchomel, R. T. Weber, Z. Fisk, and Ivan K. Schuller, “Methodology and search for superconductivity in the La-Si-C system”, Superconductor Science and Technology 24, 075017 (2011). Ali C. Basaran worked on the sample design, fabrication, measurement,

contributed to the rietveld refinement, and analysis for this work. I would like to thank Ted Grant for arc melting samples.

J. de la Venta, Ali C. Basaran, T. Grant, J.M. Gallardo-Amores, J.G. Ramirez, M.A. Alario-Franco, Z. Fisk, and Ivan K. Schuller, "Magnetism and the absence of superconductivity in the praseodymium–silicon system doped with carbon and boron", Journal of Magnetism and Magnetic Materials 340,27-31, (2013). Ali C. Basaran worked on the sample design, measurement, and data analysis for this work.

S. Guenon, Y.J. Rosen, Ali C. Basaran, and Ivan K. Schuller, "Highly effective superconducting vortex pinning in conformal crystals", Applied Physics Letters 102, 25, (2013). Ali C. Basaran contributed to the sample fabrication, lithography, measurement, and analysis for this work.

J. Ramirez, Ali C. Basaran, J. de la Venta, J. Pereiro, and Ivan K. Schuller, "Magnetic Field Modulated Microwave Spectroscopy (MFMMS) across phase transitions and the search for new superconductors", Reports on Progress in Physics accepted (2014). The dissertation author was the primary investigator and the co-first-author of this paper. Ali C. Basaran worked on the equipment design and installation, performed sample design and fabrication, measurement, and analysis for this work.

Chapter 5, in part, is currently submitted to Scientific Reports for publication of the material. Co-authors include S. Guenon, J.G. Ramirez, M. Thiemens, S. Taylor, and Ivan K. Schuller. Ali C. Basaran contributed to the measurement and analysis for this work and will be a co-author of this material.

Chapter 5, in part, is currently being prepared for publication of the material. Co-authors include G. Ramirez, J. de la Venta, S. Wang, T. Saerbeck, X. Batlle, and Ivan K. Schuller. Ali C. Basaran contributed to the FMR measurement and analysis for this work and will be a co-author of this material.

Chapter 5, in part, is currently submitted to Nano Letters for publication of the material. Co-authors include A.F. Rodriguez, M. Kovylina, R. Morales, J. Llobet, X. Borrise, M.A. Marcus, A. Scholl, Ivan K. Schuller, X. Batlle, and A. Labarta. Ali C. Basaran performed the sample fabrication, magnetization measurements, and contributed to the date analysis for this work and will be a co-author of this material.

6. Summary

Due to the short range of the exchange interaction, the exchange bias phenomenon has been mostly considered as an interfacial effect. The importance and contribution of the magnetic structure in regions away from the interface remain ambiguous. In this dissertation, we studied the individual contributions of each region on exchange bias. We considered the exchange bias effect in magnetic thin films as mainly defined by the three components of the spin structure; i) at the FM/AFM interface, ii) in the AFM layer, and iii) in the FM layer. We studied these three ingredients individually using different experimental approaches and found that the exchange bias is significantly affected by the *bulk* of AFM and FM layers.

In order to understand the general properties of our model exchange bias system, Ni/FeF_2, we performed magnetoresistance measurements by using a cross shaped ferromagnetic nano-junction (chapter 2). The advantage of having a cross shaped junction is that longitudinal and transverse components of the magnetization could be simultaneously measured via magnetoresistance response. Therefore, a combination of these measurements allowed us to study all main features of the magnetization reversal mechanism from a single measurement setup. In addition to the general features of the exchange bias system, we unambiguously showed that PHE measurements can be used to distinguish the rotation direction of the magnetization. We found the presence of a distribution of unidirectional anisotropy axes around the crystallographic easy axis.

These unidirectional anisotropy axes determine the direction of the magnetization rotation. Furthermore, the rotational dependence of the magnetization was used to investigate the spin configuration of crosses by rotating the sample in the CW and CCW directions. We observed an angular hysteretic behavior when the applied field in the range of the exchange bias field. We simulated all of the experimental features using a model based on incomplete domain walls that are formed due to exchange bias.

In chapter 3, we presented an experimental approach which allowed us to separate and investigate the individual contributions of the AFM bulk and interface on exchange bias. We used He-ion bombardment to create defects and therefore control both magnitude and direction of the exchange bias field. We employed two different approaches: i) the defects were selectively created either in the bulk of the AFM layer or at the FM/AFM interface by varying the capping layer thickness, and ii) the number of defects at a certain depth was controlled by varying the ion dose. We have obtained the penetration depth profiles of bombardment ions and the number of vacancies (defects) from SRIM (Stopping and Range of Ions in Matter) simulations. We performed extensive structural and magnetic characterizations before and after the bombardment to investigate the effect of the selectively created defects at different locations on the exchange bias. These results unambiguously revealed that the AFM bulk is an important ingredient in establishing and controlling the exchange bias. Therefore, the AFM bulk has to be included in any theoretical considerations. Moreover, the ion dose dependency revealed two important conclusions: i) the exchange bias can be significantly affected only by creating defects in the bulk of the

AFM layer – without altering the interface, and ii) the exchange bias field and the coercive field are decoupled and can behave independently.

As a third ingredient, we studied the effect of the FM layer on exchange bias in chapter 4. We investigated the influence of the FM thickness and the temperature on spin configuration within the ferromagnet. We prepared several Permalloy / FeF_2 films with varying the thickness of the FM layer in-situ and investigated with magnetization measurements. All these measurements revealed the active role of the spin structure within the ferromagnet. In contrast to the widely accepted inverse proportionality rule with the thickness of the ferromagnet, we found a deviation from $1/t_{FM}$ dependence due to the spin structure in the ferromagnet. The model based on incomplete domain walls parallel to the FM/AFM interface quantitatively accounts for the experimental results and, in particular, for the deviation from the inverse proportionality law.

As well as the above mentioned three constituents of the exchange bias phenomenon we have studied many other projects in parallel. We included a summary of these other studies in chapter 5. We have explored new superconducting materials using a microwave absorption technique called Magnetic Field Modulated Microwave Spectroscopy (MFMMS). We showed that MFMMS is a very sensitive and selective technique and can be used in the search for new superconducting materials. We identified a known superconducting phase in a new La-C compound. We also found a new magnetic phase in Pr-Si-C system. We have also investigated the superconducting vortex pinning in conformal crystal geometry using magnetic nanodots.

There are ongoing projects by the time of writing this dissertation. We have applied the MFMMS technique in the search for superconductivity in meteorites and micro-meteorites. We are still collecting data from different meteorites and writing a manuscript regarding possible superconducting phases in exotic materials. We have also investigated electrical and magnetic properties of La-Sr-Mn-O thin films, in which possible intrinsic exchange bias induced by the oxygen irradiation through a porous alumina mask. In a separate experiment, we have employed photoemission electron microscopy combined with X-ray magnetic circular dichroism techniques for direct observations of the spin configuration at both sides of the Ni/FeF_2 interface. We found that the final spin structure is determined by the competing balance between the two dissimilar magnetic length scales.

To summarize, we built this dissertation around the three pillars of the exchange bias: the interface, the antiferromagnet, and the ferromagnet. We have performed clear cut experiments to address directly many crucial issues in the exchange bias phenomenon: the dependence of exchange bias on interfacial and bulk AFM and FM spins. The study shows that the exchange bias is significantly affected by the *bulk* of AFM and FM layers. Since the exchange bias has a key role for many nanomagnetism and spintronics related applications, this study will have a high impact in the community and extend some long-standing controversies in magnetism.

Appendix

Table 1. Sample preparation steps for cross junction: lift-off

1.	Substrate	MgF_2, 5 mm by 10 mm
2.	Cleaning	10 min. Acetone, 10 min. Methanol, 10 min. DI water (x2) – in ultrasonic bath
3.	Deposition	Electron-beam evaporator, 100 nm FeF_2
4.	Spin coating	S1818, 5000 RPM, 1 min.
5.	Baking	Hot plate, 115 °C, 1 min.
6.	Photolithography (cross)	UV exposure, 3.5 min.
7.	Developing	AZ developer 1:1 DI water, 40 s rinse with DI water 20 s, dry with N_2
8.	Visual check	Optical microscope
9.	Ion milling	4 mTorr Ar, 50 W, 3 min.
10.	Deposition	Sputter, 10 nm Ni, 4 mTorr Ar, 100 W, ~ 2 Å/s
11.	Lift-off	Acetone, 2 – 4 hours
12.	Cleaning	2 min. Isopropanol, 2 min. DI water (+ low power ultrasonic bath if needed)
13.	Visual check	Optical microscope and SEM
14.	Spin coating	S1818, 5000 RPM, 1 min.
15.	Baking	Hot plate, 115 °C, 1 min.
16.	Photolithography (contacts)	UV exposure, 3.5 min.
17.	Developing	AZ developer 1:1 DI water, 40 s 20 s rinse with DI water, dry with N_2
18.	Visual check	Optical microscope
19.	Ion milling	4 mTorr Ar, 50 W, 3 min.
20.	Deposition	Sputter, Ti (10 nm) / Au (90 nm), 4 mTorr Ar, 100 W
21.	Lift-off	Acetone, 2 – 4 hours
22.	Cleaning	2 min. Isopropanol, 2 min. DI water(+ low power ultrasonic bath if needed)
23.	Visual check	Optical microscope

Table 2. Sample preparation steps for cross junction: etching

1.	Substrate	MgF_2, 5 mm by 10 mm
2.	Cleaning	10 min. Acetone, 10 min. Methanol, 10 min. DI water (x2) – in ultrasonic bath
3.	Deposition	Electron-beam evaporator, 100 nm FeF_2 + 10 nm Ni
4.	Spin coating	NR9-1500PY, 4000 RPM, 40 s
5.	Pre-baking	Hot plate, 150 °C, 1 min.
6.	Photolithography (cross)	UV exposure, 3.5 min.
7.	Post-baking	Hot plate, 100 °C, 1 min.
8.	Developing	RD-6 developer, 40 s rinse with DI water 20 s (x2), dry with N_2
9.	Visual check	Optical microscope
10.	Reactive Ion Etching	25 mTorr, 40 sccm Ar, 200 W, 540 V, ~ 4 min.
11.	Visual check	Optical microscope
12.	Mask (resist) removal	Acetone, 2 – 4 hours
13.	Cleaning	2 min. Isopropanol, 2 min. DI water(+ low power ultrasonic bath if needed)
14	Visual check	Optical microscope + SEM
15.	Spin coating	S1818, 5000 RPM, 1 min.
16.	Baking	Hot plate, 115 °C, 1 min.
17	Photolithography (contacts)	UV exposure, 3.5 min.
18.	Developing	AZ developer 1:1 DI water, 40 s 20 s rinse with DI water, dry with N_2
19.	Visual check	Optical microscope
20.	Ion milling	4 mTorr Ar, 50 W, 3 min.
21.	Deposition	Sputter, Ti (10 nm) / Au (90 nm), 4 mTorr Ar, 100 W
22.	Lift-off	Acetone, 2 – 4 hours
23.	Cleaning	2 min. Isopropanol, 2 min. DI water(+ low power ultrasonic bath if needed)
24.	Visual check	Optical microscope

References

[1] S.D. Bader, Colloquium: Opportunities in nanomagnetism, Reviews of Modern Physics, 78 (2006) 1-15.

[2] J. Nogués, I.K. Schuller, Exchange bias, Journal of Magnetism and Magnetic Materials, 192 (1999) 203-232.

[3] W.H. Meiklejohn, C.P. Bean, New Magnetic Anisotropy, Physical Review, 102 (1956) 1413-1414.

[4] A.E. Berkowitz, K. Takano, Exchange anisotropy — a review, Journal of Magnetism and Magnetic Materials, 200 (1999) 552-570.

[5] C. Tsang, Magnetics of small magnetoresistive sensors (invited), Journal of Applied Physics, 55 (1984) 2226-2231.

[6] S.S.P. Parkin, K.P. Roche, M.G. Samant, P.M. Rice, R.B. Beyers, R.E. Scheuerlein, E.J. O'Sullivan, S.L. Brown, J. Bucchigano, D.W. Abraham, Y. Lu, M. Rooks, P.L. Trouilloud, R.A. Wanner, W.J. Gallagher, Exchange-biased magnetic tunnel junctions and application to nonvolatile magnetic random access memory (invited), Journal of Applied Physics, 85 (1999) 5828-5833.

[7] S. Parkin, J. Xin, C. Kaiser, A. Panchula, K. Roche, M. Samant, Magnetically engineered spintronic sensors and memory, Proceedings of the IEEE, 91 (2003) 661-680.

[8] K. O'Grady, L.E. Fernandez-Outon, G. Vallejo-Fernandez, A new paradigm for exchange bias in polycrystalline thin films, Journal of Magnetism and Magnetic Materials, 322 (2010) 883-899.

[9] P.K. Manna, S.M. Yusuf, Two interface effects: Exchange bias and magnetic proximity, Physics Reports, 535 (2014) 61-99.

[10] W.H. Meiklejohn, Exchange Anisotropy—A Review, Journal of Applied Physics, 33 (1962) 1328-1335.

[11] R. Morales, Z.-P. Li, J. Olamit, K. Liu, J.M. Alameda, I.K. Schuller, Role of the Antiferromagnetic Bulk Spin Structure on Exchange Bias, Physical Review Letters, 102 (2009) 097201.

[12] P. Miltényi, M. Gierlings, J. Keller, B. Beschoten, G. Güntherodt, U. Nowak, K.D. Usadel, Diluted Antiferromagnets in Exchange Bias: Proof of the Domain State Model, Physical Review Letters, 84 (2000) 4224-4227.

[13] M.Y. Khan, C.-B. Wu, W. Kuch, Pinned magnetic moments in exchange bias: Role of the antiferromagnetic bulk spin structure, Physical Review B, 89 (2014) 094427.

[14] R.L. Stamps, Mechanisms for exchange bias, Journal of Physics D: Applied Physics, 33 (2000) R247.

[15] M. Kiwi, Exchange bias theory, Journal of Magnetism and Magnetic Materials, 234 (2001) 584-595.

[16] E.E. Fullerton, J.S. Jiang, M. Grimsditch, C.H. Sowers, S.D. Bader, Exchange-spring behavior in epitaxial hard/soft magnetic bilayers, Physical Review B, 58 (1998) 12193-12200.

[17] W. Kuch, L.I. Chelaru, F. Offi, J. Wang, M. Kotsugi, J. Kirschner, Tuning the magnetic coupling across ultrathin antiferromagnetic films by controlling atomic-scale roughness, Nat Mater, 5 (2006) 128-133.

[18] J. Nogués, D. Lederman, T.J. Moran, I.K. Schuller, K.V. Rao, Large exchange bias and its connection to interface structure in FeF_2–Fe bilayers, Applied Physics Letters, 68 (1996) 3186-3188.

[19] T. Saerbeck, H. Zhu, D. Lott, H. Lee, P.R. LeClair, G.J. Mankey, A.P.J. Stampfl, F. Klose, Tailoring exchange bias through chemical order in epitaxial $FePt_3$ films, Journal of Applied Physics, 114 (2013) 013901-013905.

[20] K. Nishioka, C. Hou, H. Fujiwara, R.D. Metzger, Grain size effect on ferro-antiferromagnetic coupling of NiFe/FeMn systems, Journal of Applied Physics, 80 (1996) 4528-4533.

[21] M. Pakala, Y. Huai, G. Anderson, L. Miloslavsky, Effect of underlayer roughness, grain size, and crystal texture on exchange coupled IrMn/CoFe thin films, Journal of Applied Physics, 87 (2000) 6653-6655.

[22] J. Nogués, T.J. Moran, D. Lederman, I.K. Schuller, K.V. Rao, Role of interfacial structure on exchange-biased FeF_2-Fe, Physical Review B, 59 (1999) 6984-6993.

[23] R. Jungblut, R. Coehoorn, M.T. Johnson, J. aan de Stegge, A. Reinders, Orientational dependence of the exchange biasing in molecular-beam-epitaxy-grown $Ni_{80}Fe_{20}/Fe_{50}Mn_{50}$ bilayers (invited), Journal of Applied Physics, 75 (1994) 6659-6664.

[24] Y.K. Kim, S.-R. Lee, S.A. Song, G.-S. Park, H.S. Yang, K.-I. Min, Magnetoresistance and interlayer diffusion in PtMn spin valves upon postdeposition annealing, Journal of Applied Physics, 89 (2001) 6907-6909.

[25] A. Mougin, T. Mewes, M. Jung, D. Engel, A. Ehresmann, H. Schmoranzer, J. Fassbender, B. Hillebrands, Local manipulation and reversal of the exchange bias field by ion irradiation in FeNi/FeMn double layers, Physical Review B, 63 (2001) 060409.

[26] J.-V. Kim, R.L. Stamps, Defect-modified exchange bias, Applied Physics Letters, 79 (2001) 2785-2787.

[27] J. Nogués, D. Lederman, T.J. Moran, I.K. Schuller, Positive Exchange Bias in FeF_2-Fe Bilayers, Physical Review Letters, 76 (1996) 4624-4627.

[28] Z.-P. Li, J. Eisenmenger, C.W. Miller, I.K. Schuller, Anomalous Spontaneous Reversal in Magnetic Heterostructures, Physical Review Letters, 96 (2006) 137201.

[29] C.L. Dennis, R.P. Borges, L.D. Buda, U. Ebels, J.F. Gregg, M. Hehn, E. Jouguelet, K. Ounadjela, I. Petej, I.L. Prejbeanu, M.J. Thornton, The defining length scales of mesomagnetism: a review, Journal of Physics: Condensed Matter, 14 (2002) R1175.

[30] J.I. Martín, J. Nogués, K. Liu, J.L. Vicent, I.K. Schuller, Ordered magnetic nanostructures: fabrication and properties, Journal of Magnetism and Magnetic Materials, 256 (2003) 449-501.

[31] J. Nogués, J. Sort, V. Langlais, V. Skumryev, S. Suriñach, J.S. Muñoz, M.D. Baró, Exchange bias in nanostructures, Physics Reports, 422 (2005) 65-117.

[32] J.F. Ziegler, J.P. Biersack, U. Littmark, The Stopping and Range of Ions in Solids, Pergamon Press, New York, 1985.

[33] J.d.l. Venta, A.C. Basaran, T. Grant, A.J.S. Machado, M.R. Suchomel, R.T. Weber, Z. Fisk, I.K. Schuller, Methodology and search for superconductivity in the La–Si–C system, Superconductor Science and Technology, 24 (2011) 075017.

[34] J. de la Venta, A.C. Basaran, T. Grant, J.M. Gallardo-Amores, J.G. Ramirez, M.A. Alario-Franco, Z. Fisk, I.K. Schuller, Magnetism and the absence of superconductivity in the praseodymium–silicon system doped with carbon and boron, Journal of Magnetism and Magnetic Materials, 340 (2013) 27-31.

[35] S. Guénon, Y.J. Rosen, A.C. Basaran, I.K. Schuller, Highly effective superconducting vortex pinning in conformal crystals, Applied Physics Letters, 102 (2013).

[36] H. Wang, T. Zhu, K. Zhao, W.N. Wang, C.S. Wang, Y.J. Wang, W.S. Zhan, Surface spin glass and exchange bias in Fe_3O_4 nanoparticles compacted under high pressure, Physical Review B, 70 (2004) 092409.

[37] J. Kouvel, A Ferromagnetic-Antiferromagnetic Model Foe Copper-Manganese and Related Alloys, J. Phys. Chem. Solids, 24 (1963) 795-822.

[38] R.D. Hempstead, S. Krongelb, D.A. Thompson, Unidirectional anisotropy in nickel-iron films by exchange coupling with antiferromagnetic films, Magnetics, IEEE Transactions on, 14 (1978) 521-523.

[39] F. Radu, H. Zabel, Exchange Bias Effect of Ferro-/Antiferromagnetic Heterostructures, in: H. Zabel, S. Bader (Eds.) Magnetic Heterostructures, Springer Berlin Heidelberg, 2008, pp. 97-184.

[40] Z.-h. Yang, X.-y. Wang, L. Liu, X.-p. Su, Structural, magnetic and electronic properties of FeF_2 by first-principle calculation, Transactions of Nonferrous Metals Society of China, 22 (2012) 386-390.

[41] M.T. Hutchings, B.D. Rainford, H.J. Guggenheim, Spin waves in antiferromagnetic FeF 2, Journal of Physics C: Solid State Physics, 3 (1970) 307.

[42] J. Strempfer, U. Rütt, W. Jauch, Absolute Spin Magnetic Moment of FeF_2 from High Energy Photon Diffraction, Physical Review Letters, 86 (2001) 3152-3155.

[43] I.V. Roshchin, O. Petracic, R. Morales, Z.-P. Li, X. Batlle, I.K. Schuller, Lateral length scales in exchange bias, Europhysics Letters, 71 (2005) 297.

[44] M.R. Fitzsimmons, P. Yashar, C. Leighton, I.K. Schuller, J. Nogués, C.F. Majkrzak, J.A. Dura, Asymmetric Magnetization Reversal in Exchange-Biased Hysteresis Loops, Physical Review Letters, 84 (2000) 3986-3989.

[45] Z.-P. Li, O. Petracic, R. Morales, J. Olamit, X. Batlle, K. Liu, I.K. Schuller, Asymmetric Reversal in Inhomogeneous Magnetic Heterostructures, Physical Review Letters, 96 (2006) 217205.

[46] S. Roy, M.R. Fitzsimmons, S. Park, M. Dorn, O. Petracic, I.V. Roshchin, Z.-P. Li, X. Batlle, R. Morales, A. Misra, X. Zhang, K. Chesnel, J.B. Kortright, S.K. Sinha, I.K. Schuller, Depth Profile of Uncompensated Spins in an Exchange Bias System, Physical Review Letters, 95 (2005) 047201.

[47] M.R. Fitzsimmons, B.J. Kirby, S. Roy, Z.-P. Li, I.V. Roshchin, S.K. Sinha, I.K. Schuller, Pinned magnetization in the antiferromagnet and ferromagnet of an exchange bias system, Physical Review B, 75 (2007) 214412.

[48] D. Mauri, H.C. Siegmann, P.S. Bagus, E. Kay, Simple model for thin ferromagnetic films exchange coupled to an antiferromagnetic substrate, Journal of Applied Physics, 62 (1987) 3047-3049.

[49] M. Kiwi, J. Mejía-López, R.D. Portugal, R. Ramírez, Exchange bias model for Fe/FeF 2 : Role of domains in the ferromagnet, Europhysics Letters, 48 (1999) 573.

[50] C. Leighton, M. Song, J. Nogués, M.C. Cyrille, I.K. Schuller, Using magnetoresistance to probe reversal asymmetry in exchange biased bilayers, Journal of Applied Physics, 88 (2000) 344-347.

[51] T. Gredig, I.N. Krivorotov, E.D. Dahlberg, Magnetization reversal in exchange biased Co/CoO probed with anisotropic magnetoresistance, Journal of Applied Physics, 91 (2002) 7760-7762.

[52] C. Binek, A. Hochstrat, X. Chen, P. Borisov, W. Kleemann, B. Doudin, Electrically controlled exchange bias for spintronic applications, Journal of Applied Physics, 97 (2005).

[53] W. Thomson, The Bakerian Lecture.—On the Electro-dynamic Qualities of Metals, Philosophical Transactions of the Royal Society of London, 146 (1856) 649-751.

[54] T.R. McGuire, R.I. Potter, Anisotropic magnetoresistance in ferromagnetic 3d alloys, Magnetics, IEEE Transactions on, 11 (1975) 1018-1038.

[55] E.D. Dahlberg, K. Riggs, G.A. Prinz, Magnetotransport: An ideal probe of anisotropy energies in epitaxial films (invited), Journal of Applied Physics, 63 (1988) 4270-4275.

[56] T. Miyazaki, Magnetoresistance of Alloy Films and Multilayers, Magnetics in Japan, IEEE Translation Journal on, 8 (1993) 351-360.

[57] M. Geissler, Y. Xia, Patterning: Principles and Some New Developments, Advanced Materials, 16 (2004) 1249-1269.

[58] Y. Chen, A. Pépin, Nanofabrication: Conventional and nonconventional methods, ELECTROPHORESIS, 22 (2001) 187-207.

[59] B.D. Gates, Q. Xu, M. Stewart, D. Ryan, C.G. Willson, G.M. Whitesides, New Approaches to Nanofabrication: Molding, Printing, and Other Techniques, Chemical Reviews, 105 (2005) 1171-1196.

[60] R. Morales, Z.-P. Li, O. Petracic, X. Batlle, I.K. Schuller, J. Olamit, K. Liu, Magnetization depth dependence in exchange biased thin films, Applied Physics Letters, 89 (2006) -.

[61] M. Kiwi, J. Mejia-Lopez, R.D. Portugal, R. Ramirez, Exchange-bias systems with compensated interfaces, Applied Physics Letters, 75 (1999) 3995-3997.

[62] S.S.P. Parkin, Giant Magnetoresistance in Magnetic Nanostructures, Annual Review of Materials Science, 25 (1995) 357-388.

[63] K. Liu, C.L. Chien, Magnetic and magneto-transport properties of novel nanostructured networks, Magnetics, IEEE Transactions on, 34 (1998) 1021-1023.

[64] F.B. Mancoff, S.E. Russek, Spin-current-induced magnetotransport in Co-Cu-Co nanostructures, Magnetics, IEEE Transactions on, 38 (2002) 2853-2855.

[65] K. Hong, N. Giordano, Approach to mesoscopic magnetic measurements, Physical Review B, 51 (1995) 9855-9862.

[66] E.E. Fullerton, D.M. Kelly, J. Guimpel, I.K. Schuller, Y. Bruynseraede, Roughness and giant magnetoresistance in Fe/Cr superlattices, Physical Review Letters, 68 (1992) 859-862.

[67] J.I. Martín, J. Nogués, I.K. Schuller, M.J. Van Bael, K. Temst, C. Van Haesendonck, V.V. Moshchalkov, Y. Bruynseraede, Magnetization reversal in long chains of submicrometric Co dots, Applied Physics Letters, 72 (1998) 255-257.

[68] U. Ruediger, J. Yu, S. Zhang, A.D. Kent, S.S.P. Parkin, Negative Domain Wall Contribution to the Resistivity of Microfabricated Fe Wires, Physical Review Letters, 80 (1998) 5639-5642.

[69] J.E. Wegrowe, D. Kelly, A. Franck, S.E. Gilbert, J.P. Ansermet, Magnetoresistance of Ferromagnetic Nanowires, Physical Review Letters, 82 (1999) 3681-3684.

[70] T. Taniyama, I. Nakatani, T. Namikawa, Y. Yamazaki, Resistivity due to Domain Walls in Co Zigzag Wires, Physical Review Letters, 82 (1999) 2780-2783.

[71] A. Fert, L. Piraux, Magnetic nanowires, Journal of Magnetism and Magnetic Materials, 200 (1999) 338-358.

[72] S. Mangin, D. Ravelosona, J.A. Katine, M.J. Carey, B.D. Terris, E.E. Fullerton, Current-induced magnetization reversal in nanopillars with perpendicular anisotropy, Nat Mater, 5 (2006) 210-215.

[73] M.I. Montero, R.K. Dumas, G. Liu, M. Viret, O.M. Stoll, W.A.A. Macedo, I.K. Schuller, Magnetoresistance of mechanically stable Co nanoconstrictions, Physical Review B, 70 (2004) 184418.

[74] D.C. Leitao, J. Ventura, J.M. Teixeira, C.T. Sousa, S. Pinto, J.B. Sousa, J.M. Michalik, J.M.D. Teresa, M. Vazquez, J.P. Araujo, Correlations among magnetic, electrical and magneto-transport properties of NiFe nanohole arrays, Journal of Physics: Condensed Matter, 25 (2013) 066007.

[75] L. Ejsing, M.F. Hansen, A.K. Menon, H.A. Ferreira, D.L. Graham, P.P. Freitas, Planar Hall effect sensor for magnetic micro- and nanobead detection, Applied Physics Letters, 84 (2004) 4729-4731.

[76] T.Q. Hung, B.P. Rao, C. Kim, Planar Hall effect in biosensor with a tilted angle of the cross-junction, Journal of Magnetism and Magnetic Materials, 321 (2009) 3839-3841.

[77] C.D. Damsgaard, S.C. Freitas, P.P. Freitas, M.F. Hansen, Exchange-biased planar Hall effect sensor optimized for biosensor applications, Journal of Applied Physics, 103 (2008) -.

[78] A. Schuhl, F.N. Van Dau, J.R. Childress, Low-field magnetic sensors based on the planar Hall effect, Applied Physics Letters, 66 (1995) 2751-2753.

[79] Z. Ge, W.L. Lim, S. Shen, Y.Y. Zhou, X. Liu, J.K. Furdyna, M. Dobrowolska, Magnetization reversal in (Ga,Mn)As/MnO exchange-biased structures: Investigation by planar Hall effect, Physical Review B, 75 (2007) 014407.

[80] Y.S. Huang, C.C. Wang, A.O. Adeyeye, Determination of vortex chirality using planar Hall effect, Journal of Applied Physics, 100 (2006) -.

[81] T. Kimura, F. Wakaya, J. Yanagisawa, Y. Yuba, K. Gamo, Magnetization process and resistance jumps in a submicron-scale cross-shaped Co wire, Journal of Magnetism and Magnetic Materials, 222 (2000) 79-85.

[82] T. Kimura, F. Wakaya, K. Gamo, Control of magnetization rotation using submicron-wide cross geometry, Journal of Magnetism and Magnetic Materials, 248 (2002) 286-291.

[83] Y.C. Chang, C.C. Chang, J.C. Wu, Z.H. Wei, M.F. Lai, C.R. Chang, Probing the Magnetization Reversal of Microstructured Permalloy Cross by Planar Hall Measurement and Magnetic Force Microscopy, Magnetics, IEEE Transactions on, 42 (2006) 2963-2965.

[84] Y.S. Huang, C.C. Wang, A.O. Adeyeye, D. Tripathy, Planar Hall effect in orthogonal submicrometer Co wires, Journal of Applied Physics, 99 (2006) -.

[85] G. Li, T. Yang, Q. Hu, H. Jiang, W. Lai, Ferromagnetic domain structure and hysteresis of exchange bias in NiFe/NiMn bilayers, Physical Review B, 65 (2002) 134421.

[86] A. Nemoto, Y. Otani, S.G. Kim, K. Fukamichi, O. Kitakami, Y. Shimada, Magnetoresistance and planar Hall effects in submicron exchange-coupled NiO/Fe[sub 19]Ni[sub 81] wires, Applied Physics Letters, 74 (1999) 4026-4028.

[87] A. Tillmanns, S. Oertker, B. Beschoten, G. Güntherodt, C. Leighton, I.K. Schuller, J. Nogués, Magneto-optical study of magnetization reversal asymmetry in exchange bias, Applied Physics Letters, 89 (2006) -.

[88] J. Camarero, J. Sort, A. Hoffmann, J.M. García-Martín, B. Dieny, R. Miranda, J. Nogués, Origin of the Asymmetric Magnetization Reversal Behavior in Exchange-Biased Systems: Competing Anisotropies, Physical Review Letters, 95 (2005) 057204.

[89] R. Morales, M. Kovylina, I.K. Schuller, A. Labarta, X. Batlle, Antiferromagnetic/ferromagnetic nanostructures for multidigit storage units, Applied Physics Letters, 104 (2014) -.

[90] T. Pokhil, R. Chantrell, C. Hou, E. Singleton, Rotational relaxation of pinning field in AFM/FM bilayer films, Journal of Magnetism and Magnetic Materials, 272–276, Supplement (2004) E849-E851.

[91] Z.-P. Li, C.W. Miller, I.V. Roshchin, I.K. Schuller, Origin of spontaneous magnetization reversal in exchange biased heterostructures, Physical Review B, 76 (2007) 014423.

[92] A.P. Malozemoff, Mechanisms of exchange anisotropy (invited), Journal of Applied Physics, 63 (1988) 3874-3879.

[93] U. Nowak, A. Misra, K.D. Usadel, Domain state model for exchange bias, Journal of Applied Physics, 89 (2001) 7269-7271.

[94] J.D. Dutson, C. Huerrich, G. Vallejo-Fernandez, L.E. Fernandez-Outon, G. Yi, S. Mao, R.W. Chantrell, K. O'Grady, Bulk and interfacial effects in exchange bias systems, Journal of Physics D: Applied Physics, 40 (2007) 1293.

[95] A.P. Malozemoff, Random-field model of exchange anisotropy at rough ferromagnetic-antiferromagnetic interfaces, Physical Review B, 35 (1987) 3679-3682.

[96] U. Nowak, K.D. Usadel, J. Keller, P. Miltényi, B. Beschoten, G. Güntherodt, Domain state model for exchange bias.I.Theory, Physical Review B, 66 (2002) 014430.

[97] J. Keller, P. Miltényi, B. Beschoten, G. Güntherodt, U. Nowak, K.D. Usadel, Domain state model for exchange bias.II.Experiments, Physical Review B, 66 (2002) 014431.

[98] J.-I. Hong, T. Leo, D.J. Smith, A.E. Berkowitz, Enhancing Exchange Bias with Diluted Antiferromagnets, Physical Review Letters, 96 (2006) 117204.

[99] D.N.H. Nam, W. Chen, K.G. West, D.M. Kirkwood, J. Lu, S.A. Wolf, Propagation of exchange bias in CoFe/FeMn/CoFe trilayers, Applied Physics Letters, 93 (2008) -.

[100] M. Ali, C.H. Marrows, B.J. Hickey, Controlled enhancement or suppression of exchange biasing using impurity layers, Physical Review B, 77 (2008) 134401.

[101] M.R. Fitzsimmons, D. Lederman, M. Cheon, H. Shi, J. Olamit, I.V. Roshchin, I.K. Schuller, Antiferromagnetic domain size and exchange bias, Physical Review B, 77 (2008) 224406.

[102] S. Brück, G. Schütz, E. Goering, X. Ji, K.M. Krishnan, Uncompensated Moments in the MnPd/Fe Exchange Bias System, Physical Review Letters, 101 (2008) 126402.

[103] M. Ali, C.H. Marrows, M. Al-Jawad, B.J. Hickey, A. Misra, U. Nowak, K.D. Usadel, Antiferromagnetic layer thickness dependence of the IrMn/Co exchange-bias system, Physical Review B, 68 (2003) 214420.

[104] C. Tsang, N. Heiman, K. Lee, Exchange induced unidirectional anisotropy at FeMn-Ni80Fe20 interfaces, Journal of Applied Physics, 52 (1981) 2471-2473.

[105] A. Ehresmann, D. Junk, D. Engel, A. Paetzold, K. Röll, On the origin of ion bombardment induced exchange bias modifications in polycrystalline layers, Journal of Physics D: Applied Physics, 38 (2005) 801.

[106] T. Mewes, R. Lopusnik, J. Fassbender, B. Hillebrands, M. Jung, D. Engel, A. Ehresmann, H. Schmoranzer, Suppression of exchange bias by ion irradiation, Applied Physics Letters, 76 (2000) 1057-1059.

[107] M. Urbaniak, P. Kuświk, Z. Kurant, M. Tekielak, D. Engel, D. Lengemann, B. Szymański, M. Schmidt, J. Aleksiejew, A. Maziewski, A. Ehresmann, F. Stobiecki, Domain-Wall Movement Control in Co/Au Multilayers by He^{+} -Ion-Bombardment-Induced Lateral Coercivity Gradients, Physical Review Letters, 105 (2010) 067202.

[108] D. Lengemann, D. Engel, A. Ehresmann, Plasma ion source for in situ ion bombardment in a soft x-ray magnetic scattering diffractometer, Review of Scientific Instruments, 83 (2012) -.

[109] J. Ziegler, J. Biersack, The Stopping and Range of Ions in Matter, in: D.A. Bromley (Ed.) Treatise on Heavy-Ion Science, Springer US, 1985, pp. 93-129.

[110] A. Nelson, Co-refinement of multiple-contrast neutron/X-ray reflectivity data using MOTOFIT, Journal of Applied Crystallography, 39 (2006) 273-276.

[111] M. Kovylina, R. Morales, A. Labarta, X. Batlle, Magnetization reversal in Ni/FeF_2 heterostructures with the coexistence of positive and negative exchange bias, Physical Review B, 86 (2012) 224414.

[112] A. Ehresmann, C. Schmidt, T. Weis, D. Engel, Thermal exchange bias field drift in field cooled Mn[sub 83]Ir[sub 17]/Co[sub 70]Fe[sub 30] thin films after 10 keV He ion bombardment, Journal of Applied Physics, 109 (2011) 023910-023917.

[113] A. Ehresmann, D. Engel, T. Weis, A. Schindler, D. Junk, J. Schmalhorst, V. Höink, M.D. Sacher, G. Reiss, Fundamentals for magnetic patterning by ion bombardment of exchange bias layer systems, physica status solidi (b), 243 (2006) 29-36.

[114] D. Engel, A. Kronenberger, M. Jung, H. Schmoranzer, A. Ehresmann, A. Paetzold, K. Röll, Exchange anisotropy modification in NiO/NiFe bilayers by ion bombardment, Journal of Magnetism and Magnetic Materials, 263 (2003) 275-281.

[115] H. Shi, Z. Liu, D. Lederman, Exchange bias of polycrystalline Co on single-crystalline $Fe_xZn_{1-x}F_2$ thin films, Physical Review B, 72 (2005) 224417.

[116] H. Shi, D. Lederman, E.E. Fullerton, Exchange bias in $Fe_xZn_{1-x}F_2$/Co bilayers, Journal of Applied Physics, 91 (2002) 7763-7765.

[117] H. Shi, D. Lederman, N.R. Dilley, R.C. Black, J. Diedrichs, K. Jensen, M.B. Simmonds, Temperature-induced sign change of the exchange bias in $Fe_{0.82}Zn_{0.18}F_2$/Co bilayers, Journal of Applied Physics, 93 (2003) 8600-8602.

[118] D. Kaya, P.N. Lapa, P. Jayathilaka, H. Kirby, C.W. Miller, I.V. Roshchin, Controlling exchange bias in FeMn with Cu, Journal of Applied Physics, 113 (2013) -.

[119] K.D. Usadel, R.L. Stamps, Exchange bias: Dependence on the properties of the ferromagnetic interface layer, Physical Review B, 82 (2010) 094432.

[120] J. Juraszek, J. Fassbender, S. Poppe, T. Mewes, B. Hillebrands, D. Engel, A. Kronenberger, A. Ehresmann, H. Schmoranzer, Tuning exchange bias and coercive fields in ferromagnet/antiferromagnet bilayers with ion irradiation, Journal of Applied Physics, 91 (2002) 6896-6898.

[121] M.D. Stiles, R.D. McMichael, Coercivity in exchange-bias bilayers, Physical Review B, 63 (2001) 064405.

[122] Y.J. Tang, B. Roos, T. Mewes, S.O. Demokritov, B. Hillebrands, Y.J. Wang, Enhanced coercivity of exchange-bias Fe/MnPd bilayers, Applied Physics Letters, 75 (1999) 707-709.

[123] C. Leighton, J. Nogués, B.J. Jönsson-Åkerman, I.K. Schuller, Coercivity Enhancement in Exchange Biased Systems Driven by Interfacial Magnetic Frustration, Physical Review Letters, 84 (2000) 3466-3469.

[124] T.J. Moran, J.M. Gallego, I.K. Schuller, Increased exchange anisotropy due to disorder at permalloy/CoO interfaces, Journal of Applied Physics, 78 (1995) 1887-1891.

[125] L.E. Fernandez-Outon, K. O'Grady, Angular dependence of coercivity and exchange bias in IrMn/CoFe bilayers, Journal of Magnetism and Magnetic Materials, 290–291, Part 1 (2005) 536-539.

[126] X.Z. Yu, Y. Onose, N. Kanazawa, J.H. Park, J.H. Han, Y. Matsui, N. Nagaosa, Y. Tokura, Real-space observation of a two-dimensional skyrmion crystal, Nature, 465 (2010) 901-904.

[127] S. Mühlbauer, B. Binz, F. Jonietz, C. Pfleiderer, A. Rosch, A. Neubauer, R. Georgii, P. Böni, Skyrmion Lattice in a Chiral Magnet, Science, 323 (2009) 915-919.

[128] P. Steadman, M. Ali, A.T. Hindmarch, C.H. Marrows, B.J. Hickey, S. Langridge, R.M. Dalgliesh, S. Foster, Exchange Bias in Spin-Engineered Double Superlattices, Physical Review Letters, 89 (2002) 077201.

[129] Y. Henry, S. Mangin, T. Hauet, F. Montaigne, Positive exchange-bias induced by interface domain wall quenching in GdFe/TbFe films, Physical Review B, 73 (2006) 134420.

[130] G.h. Guo, G.f. Zhang, X.g. Wang, Crossover from reversible to irreversible magnetic exchange-spring processes in antiferromagnetically exchange-coupled soft/hard bilayer structures, Journal of Applied Physics, 108 (2010) -.

[131] S.M. Zhou, K. Liu, C.L. Chien, Dependence of exchange coupling in permalloy/$Cr_{82}Al_{18}$ bilayers on the constituent layer thickness, Journal of Applied Physics, 87 (2000) 6659-6661.

[132] M. Gruyters, D. Riegel, Strong exchange bias by a single layer of independent antiferromagnetic grains: The CoO/Co model system, Physical Review B, 63 (2000) 052401.

[133] C. Leighton, M.R. Fitzsimmons, A. Hoffmann, J. Dura, C.F. Majkrzak, M.S. Lund, I.K. Schuller, Thickness-dependent coercive mechanisms in exchange-biased bilayers, Physical Review B, 65 (2002) 064403.

[134] M. Grimsditch, A. Hoffmann, P. Vavassori, H. Shi, D. Lederman, Exchange-Induced Anisotropies at Ferromagnetic-Antiferromagnetic Interfaces above and below the Néel Temperature, Physical Review Letters, 90 (2003) 257201.

[135] V.I. Nikitenko, V.S. Gornakov, A.J. Shapiro, R.D. Shull, K. Liu, S.M. Zhou, C.L. Chien, Asymmetry in Elementary Events of Magnetization Reversal in a Ferromagnetic/Antiferromagnetic Bilayer, Physical Review Letters, 84 (2000) 765-768.

[136] J.R. Schrieffer, M. Tinkham, Superconductivity, Reviews of Modern Physics, 71 (1999) S313-S317.

[137] J. Bardeen, L.N. Cooper, J.R. Schrieffer, Theory of Superconductivity, Physical Review, 108 (1957) 1175-1204.

[138] J.G. Bednorz, K.A. Müller, Possible highT c superconductivity in the Ba−La−Cu−O system, Z. Physik B - Condensed Matter, 64 (1986) 189-193.

[139] G.R. Stewart, Superconductivity in iron compounds, Reviews of Modern Physics, 83 (2011) 1589-1652.

[140] A.A. Abrikosov, Problem of super-high-Tc superconductivity, Physica C: Superconductivity, 468 (2008) 97-99.

[141] W.E. Pickett, The next breakthrough in phonon-mediated superconductivity, Physica C: Superconductivity, 468 (2008) 126-135.

[142] M. Tachiki, Overscreening mechanism for room temperature superconductivity, Physica C: Superconductivity, 468 (2008) 111-114.

[143] J.E. Hirsch, Correlations between normal-state properties and superconductivity, Physical Review B, 55 (1997) 9007-9024.

[144] J. Nagamatsu, N. Nakagawa, T. Muranaka, Y. Zenitani, J. Akimitsu, Superconductivity at 39[thinsp]K in magnesium diboride, Nature, 410 (2001) 63-64.

[145] H.Y. Hwang, Y. Iwasa, M. Kawasaki, B. Keimer, N. Nagaosa, Y. Tokura, Emergent phenomena at oxide interfaces, Nat Mater, 11 (2012) 103-113.

[146] J. de la Venta, S. Wang, J.G. Ramirez, I.K. Schuller, Control of magnetism across metal to insulator transitions, Applied Physics Letters, 102 (2013) 122404-122405.

[147] J. de la Venta, S. Wang, T. Saerbeck, J.G. Ramírez, I. Valmianski, I.K. Schuller, Coercivity enhancement in V2O3/Ni bilayers driven by nanoscale phase coexistence, Applied Physics Letters, 104 (2014) -.

[148] M.R. Fitzsimmons, I.K. Schuller, Neutron scattering—The key characterization tool for nanostructured magnetic materials, Journal of Magnetism and Magnetic Materials, 350 (2014) 199-208.